Characterization and Modeling of Nanocomposite Thermoelectric Materials System Bismuth Antimony Telluride ($(Bi_ySb_{1-y})_2Te_3$) as a Function of Temperature and Magnetic Field

by

Ming Y. Tang

B.S. in Electrical Engineering and Computer Sciences
& Materials Science and Engineering
University of California, Berkeley (2001)
S.M. in Electrical Engineering and Computer Science
Massachusetts Institute of Technology (2004)

Submitted to the Department of Electrical Engineering and Computer Science
in partial fulfillment of the requirements for the degree of
Doctor of Philosophy in Electrical Engineering and Computer Science
at the
MASSACHUSETTS INSTITUTE OF TECHNOLOGY
September 2011

Author .....
Department of Electrical Engineering and Computer Science
September 2, 2011

Certified by .....
Mildred S. Dresselhaus
Institute Professor of Electrical Engineering and Physics
Thesis Supervisor

Accepted by .....
Leslie A. Kolodziejski
Chair, Department Committee on Graduate Students

Characterization and Modeling of Nanocomposite Thermoelectric Materials System Bismuth Antimony Telluride ($(Bi_ySb_{1-y})_2Te_3$) as a Function of Temperature and Magnetic Field

by

Ming Y. Tang

Submitted to the Department of Electrical Engineering and Computer Science
on September 6, 2011, in partial fulfillment of the
requirements for the degree of
Doctor of Philosophy in Electrical Engineering and Computer Science

Abstract

This thesis looks at $(Bi_ySb_{1-y})_2Te_3$ nanocomposites as an example of the currently available nano systems. In this thesis, $(Bi_ySb_{1-y})_2Te_3$ nanocomposites are characterized from ~325K down to ~3K. Advantages of this low temperature regime include the minimization of lattice vibrations and the decreasing of κ_e with decreasing temperature. As a result, nano effects on κ_L could be better observed and characterized in this low temperature regime.

We are also interested in studying the effect of an applied magnetic field on the conduction carriers in this low temperature regime. We like to find out whether an applied magnetic field could impede the carriers' heat conducting ability more than their current conducting ability. Therefore, a magnetic field effect study is also carried out to see whether any improvement in ZT could be achieved by the applying of a magnetic field.

The measurement system used in this thesis is QD PPMS. Only the ACT and TTO options of the QD PPMS apparatus are used for measurements in this thesis. Under the ACT option, Hall and 4-pt ρ measurements on the same sample are performed. On the other hand, κ_{th}, S, and 2-pt ρ measurements are performed simultaneously on the same sample under the TTO option. Both the ACT and TTO options use an AC current instead of a DC current during ρ measurement to eliminate any unwanted Seebeck voltage.

Since the ability to perform correct measurements on thermoelectric samples is not a trivial task, benchmarking with known results is a must. In this thesis, I calibrate our QD PPMS against both the manufacturer's results and the published data, and demonstrate that our measurement system gives accurate results. I also benchmark our κ_{th} results under a magnetic field using a pyrex sample. Our results confirm that the QD PPMS apparatus does not introduce artifacts under an applied

magnetic field. Thus, any changes observed under the QD PPMS apparatus measurements in an applied magnetic field would be expected to be solely due to the sample. Lastly, no measurable difference is found between our 2-pt ρ (TTO) and 4-pt ρ (ACT) measurements.

A total of eight $(Bi_ySb_{1-y})_2Te_3$ samples are measured in this thesis. The sample set includes: (a) one bulk ingot sample manufactured by Marlow (Ingot), (b) four nanocomposite samples (XY21, XY146, XY144, and GJ99) made by collaborators from Boston College (BC) where the letters simply indicate the sample maker's initials, and (c) three nanocomposite samples (0%, 40%, and 100%) made by collaborators from Nanyang Technological University (NTU) in Singapore, where the % denotes the weight % of the nanoinclusions prepared via melt spinning [1] in the sample. All the nanocomposite samples in this thesis are made solely for research uses and are purposely fabricated under conditions different than those used for the best samples previously reported [2, 1]. Although BC and NTU use different starting materials, different fabrication machines, and different fabrication parameters, the resulting densities of the nanocomposites from the ball-milled nanopowders alone (XY21, XY146, XY144, GJ99, and 0%) are almost identical. Moreover, the addition of nanoinclusions prepared via melt spinning decreases the sample mass density somewhat.

From the XRD measurement results, we notice that (a) both the NTU and BC samples have the same XRD peak locations, (b) the NTU samples have a lower intensity for peaks (1 0 10) and (1 1 0), and (c) the NTU samples have a higher intensity for peaks (0 0 ς) where ς is an integer. Comparing the XRD patterns with the reference database, the difference in peak intensities is a good indication that the NTU samples are not completely randomized and have internal preferred orientations. From the SEM images, we notice that the NTU samples and the BC samples are markedly different. For example, the BC samples are shown to have grains in the μm range with a small grain size distribution. On the other hand, the grain sizes of the NTU samples decreases with the addition of nanoinclusions prepared via melt spinning. Moreover, the NTU samples have a wider grain size distribution that ranges from nm to μm. This observed difference is believed to arise from the difference in the fabrication techniques used by the BC and NTU teams.

Temperature-dependent κ_{th}, S, and ρ measurements, along with the carrier concentration measurements, are performed on all samples. All samples are found to be p-type materials. Transport measurements are performed both // and $\perp$ to the press direction for the nanocomposite samples, and only // to the growth direction for the Ingot sample. Anisotropic behavior is observed in κ_{th} and ρ for all the nanocomposite samples investigated, with the anisotropy being always higher in ρ than in κ_{th}. On the other hand, S is found to be isotropic. Thus, care needs be taken during the fabrication process to ensure that no unwanted anisotropic behavior is introduced. Common ρ and S features among all samples include: (a) a dramatic decrease in the peak value of κ_{th} for the nanocomposite samples when compared with the Ingot //'s value, (b) constant slope $\partial S/\partial T$ for $T < 20$K, (c) constant slope $\partial S/\partial ln(T)$ of $\sim$ 130-140μV/ln(K) for 200K $< T <$ 300K, (d) close-to-zero slope in ρ for $T < 20$K, and (e) $\rho \propto T^{1.5\pm0.1}$ for 200K $< T <$ 300K.

From the measured κ_{th}, S, and ρ data, the mobility μ_p, hole mean free path ℓ_e, and phonon mean free path ℓ_{ph} are computed. It is found that nanocomposite approach decreases μ_p, ℓ_e, and ℓ_{ph}. Moreover, the μ_p, ℓ_e, and ℓ_{ph} values are always lower in the // direction for the nanocomposite samples than in the $\perp$ direction. Furthermore, ℓ_e in general is in the nm range while ℓ_{ph} ranges from μm to nm as the temperature increases. Therefore, if one wants to decrease the κ_{th}, a possible solution is to decrease ℓ further. However, in order not to affect the ρ too much, the lower limit for ℓ should be in the nm range. As a result, decreasing ℓ would have the biggest effect on κ_{th} in the low temperature regime.

Using the κ_{th} and σ data, κ_L is extracted through the intercept method (see Section 3.5.3). This method only makes sense if all the samples have similar ℓ. Since pressure is coming from top and bottom during the fabrication process for the nanocomposite samples, my samples are expected not to behave as the same materials system along the // direction. However, for the $\perp$ direction, they can be considered as a same materials system since no pressure is applied. The 40% and 100% samples are believed to deviate from the results for the 0% sample because of the presence of nanoinclusions in them. $\kappa_{L,\perp}$ is found to be 0.76W/m-K for the 40% sample at 297K. When I compare this value with previously determined values for Bi_2Te_3 (1.4W/m-K [3]) and $(Bi_{0.3}Sb_{0.7})_2Te_3$ (0.9W/m-K [4]) alloy at 300K, these results confirm that the nanocomposite approach does indeed lower the lattice thermal conductivity.

The semi-classical model is then used to interpret the various transport coefficients ($\sigma = 1/\rho$, S, and κ_e) and is based on the Boltzmann Transport Equation (BTE) under the relaxation time approximation (RTA). Acoustic phonon scattering, ionized impurity atom scattering, neutral impurity atom scattering, alloy scattering for a 3-atom $I_pII_{1-p}III$ system, point defect scattering, grain boundary scattering, and polar optical phonon scattering are considered for the electrons. On the other hand, boundary scattering, point defect / alloy scattering, and Umklapp scattering are considered for the phonons. We find that for holes, point defect scattering dominates at low T, while acoustic phonon scattering dominates around 300K. As for phonons, boundary and point defect scattering mechanisms dominate at low T, while point defect and Umklapp scattering mechanisms dominate at high T ($\approx$300K). We also find that the nano approach increases the crossover temperature T_{cross}. For the electron model, we observe that the deformation potential (D_A) seems to be both process dependent and materials dependent. We see that D_A changes from the BC samples to the NTU samples (process dependent). Moreover, D_A changes in the NTU samples when going from 0% to 100% (materials dependent). From the electron model, the ionized impurity atom concentration N_i and the neutral impurity atom concentration N_0 reflect the somewhat anisotropic behavior of all the samples investigated. Lastly, ℓ seems to play little role in the determination of ρ.

For the phonon model, we observe that ℓ plays a rather important role in the determination of κ_L, especially at low temperatures. The value of ℓ seems to be consistently lower for the BC samples than for the NTU sample (0%) for the nanocomposite samples made solely from ball-milled nanoparticles. We also see that the Umklapp scattering contribution (B') has a materials dependent factor, where B' decreases from $\approx$ 10x10^{18}s/K for the nanoparticle nanocomposite samples to $\approx$ 4x10^{18}s/K for

the nanocomposite sample made using 100% nanoinclusions prepared via melt spinning. Furthermore, we see that the point defect contribution (A') reaches the highest value when both the nanoparticles and nanoinclusions prepared via melt spinning are present in the nanocomposite samples (e.g. the 40% sample), similar to the alloying effect on the thermal conductivity. In general, it is desirable to increase the values of A' and B', resulting in a decrease in the κ_L values. However, care needs to be taken to ensure that the phonon parameters are independent of the electron parameters so that no adverse effect on ZT would result.

The determination of $\mathcal{L}$ is also carried out based on my electron model findings. We observe that $\mathcal{L}$ is isotropic. Moreover, $\mathcal{L}$ for each sample investigated reaches the same value of $2.44\text{x}10^{-8}\text{W-Ohm/K}^2$ as $T \rightarrow 0\text{K}$ (completely degenerate limit of $\frac{\pi^2}{3}\left(\frac{k_B}{e}\right)^2$). Furthermore, the higher the hole concentration the sample has, the higher its $\mathcal{L}$ value is at a given temperature. Lastly, I find that a lower ℓ leads to higher ZT values at 297K for the BC nanocomposite samples measured in the $\perp$ direction. On the other hand, a lower ℓ leads to lower ZT values at 297K for the NTU nanocomposite samples measured in both the // and $\perp$ directions.

From the magnetic field studies on the Ingot and on the 40% samples, few important facts are demonstrated. First, an applied magnetic field can be used to effectively increase the ZT of $(Bi_ySb_{1-y})_2Te_3$, especially at temperatures below 200K. Use of a magnetic field might theoretically extend the effective temperature ranges over which $(Bi_ySb_{1-y})_2Te_3$ materials can be used for refrigeration. Second, the data under various applied B fields allow me to confidently calculate the $\mathcal{L}$ value below the temperature ranges where a plateau has occurred. Third, the data under various applied B fields serve as an important guideline for both validating any electron model and extrapolating values for $\mathcal{L}$ above the plateau occurrence temperatures. As a result, this allows me to get some insights into the temperature dependence of $\mathcal{L}$ (see Figure 4-14). Fourth, from the magnetic field dependent transport studies on our samples, we observe that the applied B field pushes away the holes more effectively in the Ingot // than the holes in the nanocomposite samples. We also find that the $\kappa_{th,\text{plateau}}$ values obtained under the magnetic field study serve as a more realistic and practical limit for κ_L. Lastly, from the magnetic field-dependent studies, we find that having point defects as the dominant scattering mechanism for the carriers results in an increase in ZT under an applied magnetic field. It would be extremely useful if one can make a sample such that the point defect dominant regime is extended to higher temperatures, resulting in a shift of the increase in the ZT ratio regime to a temperature range closer to room temperature (300K). However, care needs to be taken to ensure that such modifications would result in an increase in the ZT values under an applied magnetic field.

Thesis Supervisor: Mildred S. Dresselhaus
Title: Institute Professor of Electrical Engineering and Physics

Acknowledgments

This thesis work is no one man's work. I like to take this opportunity to thank those who contributed to my success.

I cannot ever thank Professors Millie Dresselhaus and Cyril Opeil enough for this research opportunity. Thank you Millie for your patience, guidance, and support throughout all these years. Fr. Cy, thank you for teaching me everything I need to know about low temperature measurements for the last three years. I especially thank you for the valuable machine times and your patience. I also like to thank Mrs. Laura Doughty and Mr. Edward Jacobson for their constant encouragement. As for Dr. Gene Dresselhaus, thank you for your never-ending sense of humor. I also like to thank my committee members Professors Peter Hagelstein and Gang Chen. Thank you Peter for all of your insightful thoughts and suggestions. I especially like to thank you for taking your valuable time to give me early feedback on my thesis. As for Gang, I want to thank you for your valuable suggestions and constructive criticisms throughout these years.

My thesis work would not be the same if it were not for the following individuals. I first like to thank Professors Zhifeng Ren and Huey Hoon Hng for providing me samples for measurements, and Dr. Xiao Yan and Ms. Shufen Fan for making the samples. I especially like to thank Dr. Xiao Yan for all the help on the SEM and XRD measurements. I also like to thank Mr. Bo Yu for the help on making the contact surfaces for my samples. My knowledge on the QD PPMS apparatus would not be the same without the tremendous help from Dr. Neil Dilley of Quantum Design. I like to thank Dr. Neil Dilley for all the valuable time he spent discussing QD PPMS apparatus with me. I also like to thank Mr. Mario Hofmann for his thoughtful and constructive criticisms on my presentations whenever I need it. Lastly, I like to thank Messrs. Kevin Lukas, Mani Pokharel, Marco Almeida, and Andrew Treat for making the Opeil group another home for me. They create both a pleasant and yet productive working environment. I especially like to thank Mr. Kevin Lukas for his humor and his flexibility on the machine usage time. Lastly, I have to thank Total

for its generous support for my ICT 2010 trip. Without this Total grant, ICT 2010 would not be possible and I probably could still be in the dark and never see the light at the end of the PhD tunnel.

Besides research, I also have the great opportunity to be a TA during my graduate career. I like to thank Professors Tayo Akinwande, Charles Sodini, and Jing Kong for giving me this invaluable experience. I especially like to thank Tayo and Jing for their continuing support and mentoring throughout my graduate career.

My experience would not be the same without my friends. I especially like to thank Dr. Xin Huang and Dr. Sam Au for all the fun and casual conversations, Dr. Ernie Yeh and Mrs. Connie Yeh for all the advices and encouragements, Dr. Natalija Jovanovic, Dr. Mitch Peabody, Mr. Shawn Kuo, Mr. Steve Kohen, Ms. Vivian Lei, Dr. Tyrone Hill, Dr. Chris Rycroft, and Ms. Melinda Wong for all the great hangout moments. I especially like to thank Dr. Federico Villalpando for being a great officemate and a graet friend for letting me crash with him during the last mile of my thesis writing.

Finally, I want to thank my family. I know they are always there for me even though they might not quite understand the PhD path that I am walking. I especially like to thank my older brother Eric and my mom for always being there for me. Last but not least is my love Ms. Elizabeth Liu. This thesis would not have happened if it were not for her. No matter what happens, Liz would always be there for me, cheering for me, and supporting me. She is always there even during my late night / early morning run to BC for experimental work. No words in this universe can describe how much you have done for me. Thank you Liz.

List of Acronyms and Symbols

a	- part of τ_e that is both E- and T-independent
A'	- coefficient of the phonon point defect / alloy scattering relaxation time
ACT	- Alternate Current Transport, the measurement option of QD PPMS that carries out Hall and 4-pt ρ measurements on the same sample
Au	- Gold
b	- subband index
B field	- magnetic field
$B//Q$	- measurements with the applied B field being parallel to the transport direction
$B \perp Q$	- measurements with the applied B field being perpendicular to the transport direction
B'	- coefficient of the phonon Umklapp scattering relaxation time
BC	- Boston College
Bi	- Bismuth
BTE	- Boltzmann Transport Equation
C	- coefficient of the exponent in the phonon Umklapp scattering relaxation time
^{o}C	- degree Celsius
C_A	- fraction of atom I in a 3-atom system $I_pII_{1-p}III$ ($C_A = p$)
C_v	- heat capacity per unit volume
cm	- centimeter
Cu	- Copper
D_A	- acoustic phonon deformation potential
$\overrightarrow{dk}$	- differential element in ζ dimensional k space
E	- carrier energy
$E(k)$	- carrier dispersion relation

e - electron charge (e = 1.602x10^{-19}C)

e^* - Callen effective charge

E_0 - carrier band edge energy

E_f - Fermi energy

exp - exponential function

eV - Electronvolt

$\mathbf{F}$ - force

f - distribution function

f^0 - equilibrium distribution function

$f_e(E)$ - Fermi-Dirac distribution function

$F_{imp}(E)$ - a dimensionless factor in τ_{ii}

$F_j(\eta^*)$ - Fermi-Dirac integral of order j

f_{phonon} - phonon distribution function

g - gram

h - Planck's constant (h = 6.626x10^{-34}J-s)

$\hbar$ - Planck's constant divided by 2π

I - current

i - index for τ and τ_e

$I_pII_{1-p}III$ - 3-atom system (Using $(Bi_{0.2}Sb_{0.8})_2Te_3$ as an example, I=Bi, II=Sb, III=Te, and p=0.2)

$I_qII_rIII_s$ - 3-atom system (Using $(Bi_{0.2}Sb_{0.8})_2Te_3$ as an example, I=Bi, II=Sb, III=Te, q=0.08, r=0.32, and s=0.60)

$\mathbf{k}$ - reciprocal space coordinates

K - degree Kelvin

k_B - Boltzmann constant (k_B = 1.38x10^{-23}J/K)

kV - kilovolt

$\mathcal{L}$ - Lorenz Number

$\mathscr{L}$ - integral function for the calculation of ρ, S, and κ_e

ℓ - average diameter of the grain boundaries assuming all grains have spherical shape

ℓ_e - carrier mean free path

ℓ_{ph} - phonon mean free path

LFA - Laser Flash Apparatus

ln - natural logarithm

M - effective ion mass in a 3-atom system $I_qII_rIII_s$

m - meter

M_I - mass of atom I in a 3-atom system $I_qII_rIII_s$

M_{II} - mass of atom II in a 3-atom system $I_qII_rIII_s$

M_{III} - mass of atom III in a 3-atom system $I_qII_rIII_s$

$M_{reduced}$ - reduced ion mass

m^* - density of states effective mass per carrier pocket ($m^{*3/2} = \sqrt{m_t m_t m_\ell}$)

m_0 - electron rest mass ($m_0 = 9.11\text{x}10^{-31}$kg)

m^*_{cond} - conduction effective mass for the carriers

m_ℓ - longitudinal effective mass components of an ellipsoidal model for the carrier pocket

m_t - transverse effective mass components of an ellipsoidal model for the carrier pocket

mA - milliamp

mm - millimeter

mol - mole

n - carrier concentration

N - number of atoms in an unit cell

N_0 - neutral impurity atom concentration

N_A - number of lattice points I in a 3-atom system $I_pII_{1-p}III$ unit cell

N_g - point defect concentration

N_i - ionized impurity atom concentration

Ni - Nickel

NIST - National Institute of Standards and Technology

NTU - Nanyang Technological University in Singapore

Ohm	- ohm
$P(t, t')$	- fraction of the carriers that actually survive from time t' to time t without suffering any further collisions
PD	- point defect
pocket	- number of equivalent carrier pockets
PPMS	- Physical Property Measurement System
Pt	- Platinum
Q	- heat
QD	- Quantum Design
$\overleftrightarrow{R}$	- rotational matrix
$\mathbf{r}$	- real space coordinates
R^2	- goodness of fit of linear regression with a value between 0 (no linear relationship) and 1 (all points lie exactly on a straight line)
r_0	- ionized impurity atom screening radius
R_H	- Hall coefficient
RTA	- Relaxation Time Approximation
S	- Seebeck coefficient
s	- second
Sb	- Antimony
SEM	- Scanning Electron Microscopy
Sn	- Tin
T	- Tesla
T	- temperature
t	- time
T_{cross}	- crossover temperature between the point defect scattering mechanism and the acoustic phonon scattering mechanism for the carriers
T_{flat}	- maximum T at which the ρ ratio (9T) is constant
T_{min}	- T at which the κ_{th} ratio (9T) reaches its minimum
T_{peak}	- T at which the S ratio (9T) reaches its maximum

Te - Tellurium

TTO - Thermal Transport System, the measurement option of QD PPMS that carries out κ_{th}, S, and 2-pt ρ measurements on the same sample

U_0 - volume integral of the point defect potential

$\mathbf{v}$ - velocity

v_e - carrier velocity

v_s - sound velocity

W - watt

x - dimensionless phonon energy ($x = \hbar\omega/(k_B T)$)

$\hat{x}$ - binary axis in the rhombohedral unit cell system

XRD - X-ray Powder Diffraction

y - fraction of Bi in $(Bi_ySb_{1-y})_2Te_3$

$\hat{y}$ - bisectrix axis in the rhombohedral unit cell system, which is also in the hexagonal plane and normal to $\hat{x}$

z - dimensionless longitudinal optical phonon energy ($z = \hbar\omega_\ell/(k_B T)$)

$\hat{z}$ - trigonal axis in the rhombohedral unit cell system, which is normal to both $\hat{x}$ and $\hat{y}$

ZT - dimensionless thermoelectric figure of merit ($ZT = S^2 T/(\rho\kappa_{th})$)

// - transport measurements measured parallel to the growth axis (for Ingot) or press direction (for nanocomposites)

$\perp$ - transport measurements measured perpendicular to the growth axis (for Ingot) or press direction (for nanocomposites)

α - reciprocal mass

α' - $\mathscr{L}$ index ($\alpha' = 0, 1, 2$)

β - exponent of T in τ_e

δ^3 - unit cell volume

ϵ - dimensionless carrier energy ($\epsilon = E/(k_B T)$)

ε - permittivity

ζ - dimension of the system under consideration

η^* - dimensionless Fermi energy ($\eta^* = E_f/(k_B T)$)

θ_D - Debye temperature

κ_e - electrical thermal conductivity

κ_L - lattice thermal conductivity

$\kappa_{L,\perp}$ - κ_L in the $\perp$ direction

$\kappa_{L,//}$ - κ_L in the // direction

κ_{th} - thermal conductivity ($\kappa_{th} = \kappa_e + \kappa_L$)

λ - exponent of E in τ_e

μ_p - hole mobility

μm - micrometer

μV - microvolt

ξ - a dimensionless factor in $F_{imp}(E)$

ρ - electrical resistivity

ϱ - mass density

σ - electrical conductivity

ς - an integer

τ - phonon relaxation time

τ_0 - part of τ_{PO} that is carrier energy-independent

τ_a - alloy scattering relaxation time for carriers

τ_{aph} - acoustic phonon scattering relaxation time for carriers

τ_b - boundary scattering relaxation time for phonons

$\tau_{b,e}$ - boundary scattering relaxation time for carriers

τ_e - electron relaxation time

τ_{ii} - ionized impurity atom scattering relaxation time for carriers

τ_{ni} - neutral impurity atom scattering relaxation time for carriers

τ_{PD} - point defect / alloy scattering relaxation time for phonons

$\tau_{PD,e}$ - point defect scattering relaxation time for carriers

τ_{PO} - polar optical phonon scattering relaxation time for carriers

τ_U - Umklapp scattering relaxation time for phonons

ω - phonon angular frequency

ω_ℓ - longitudinal optical phonon angular frequency

ΔE - effective bandgap offset between alloys I_0II_1III and I_1II_0III in a 3-atom system $I_pII_{1-p}III$

Γ - center of the Brillouin zone

Γ(number) - Gamma function ($\Gamma(p+1) = p\Gamma(p)$)

Γ' - scattering parameter in phonon point defect / alloy scattering relaxation time

THIS PAGE INTENTIONALLY LEFT BLANK

Contents

THIS PAGE INTENTIONALLY LEFT BLANK

List of Figures

THIS PAGE INTENTIONALLY LEFT BLANK

List of Tables

THIS PAGE INTENTIONALLY LEFT BLANK

Chapter 1

Introduction

This thesis starts off with some background information on the topic of thermoelectrics. It is then followed by the motivation for this thesis work and the outline of this thesis write-up.

1.1 Background

The thermoelectric effect is the conversion between thermal energy and electrical energy based on measuring a voltage difference produced by a temperature difference of a material, or vice versa. The two major thermoelectric applications are (a) refrigeration and (b) electricity generation through heat. Advantages of thermoelectric refrigeration include the absence of moving parts and noise. As for thermoelectric power generation, it provides a pathway to recover waste heat to increase the overall system efficiency. More importantly, thermoelectric power generation plays a vital role in supplying electricity aboard a deep space mission spacecraft or on a submarine.

Thermoelectrics can be dated all the way back to the 19th century. In 1821, Thomas Seebeck discovered that an electromotive force could be produced by heating a junction between two different metals. Following Seebeck's discovery, in 1834, Jean Peltier discovered that passing an electric current through the junction between two dissimilar conductors could result in a cooling effect. More importantly, in 1855, William Thomson (later Lord Kelvin) not only predicted a third thermoelectric effect,

but he also derived the relationship between the different thermoelectric effects using thermodynamic arguments. Resulting from these discoveries, the idea of thermoelectric materials was born. However, it was not until the invention of the transistor in 1949 that researchers started seriously looking into thermoelectric applications [9].

Since the birth of the transistor, interest in the field of thermoelectric materials has skyrocketed. The field of thermoelectrics was especially active during the 1957-1965 period. Much improvement in thermoelectric materials was made during this period, especially after the proposal in 1956 by Abram Ioffe and his co-workers that doped semiconducting materials were the best candidates for thermoelectric materials and that alloying could reduce the lattice thermal conductivity in a major way without much deterioration to the other thermoelectric parameters [9]. Unfortunately, following this very active period, little improvement in thermoelectric performance was achieved for many years, and the search for good thermoelectric materials consequently became rather inactive for the next thirty year period.

In the 1990s, using low dimensional physics concepts, Hicks and Dresselhaus predicted that a dramatic enhancement in thermoelectric performance was possible through the use of quantum wells and quantum wires [10, 11]. In the same time frame, nano-fabrication technology rapidly improved during the last two decades. With the advance in technology along with new low dimensional concepts, improvements in thermoelectric efficiency ($ZT = S^2T/(\rho\kappa_{th})$) have been demonstrated (where ρ is the electrical resistivity, S is the Seebeck coefficient, $\kappa_{th} = \kappa_e + \kappa_L$ is the thermal conductivity, κ_e is the electrical thermal conductivity, κ_L is the lattice thermal conductivity, and T is the temperature). For example, room temperature ($T = 25^oC$) values of the dimensionless thermoelectric figure of merit $ZT \sim 2.4$ have been achieved for a p-type Bi_2Te_3/Sb_2Te_3 superlattice device [12]. These promising trends have once again ignited the interest of the research community in the area of thermoelectrics.

1.2 Motivation

Since the proposal by Hicks and Dresselhaus [10, 11], many nano systems have been fabricated and high ZT values have been reported. Moreover, the new systems are fabricated using cheaper and less time intensive procedures. Although researchers now understand that the decrease in κ_L has been the key to the dramatic ZT improvement, the community still lacks a quantitative understanding of the nano effect. Therefore, we are motivated in gaining a better quantitative understanding of the nano effect.

This thesis looks at $(Bi_ySb_{1-y})_2Te_3$ nanocomposites as an example of the currently available nano systems. In this thesis, $(Bi_ySb_{1-y})_2Te_3$ nanocomposites are characterized from ~325K down to ~3K. Advantages of this low temperature regime include the minimization of lattice vibrations and the decreasing of κ_e with decreasing temperature. As a result, nano effects on κ_L could be better observed and characterized in this low temperature regime.

We are also interested in studying the effect of an applied magnetic field on the conduction carriers in this low temperature regime. We like to find out whether an applied magnetic field could impede the carriers' heat conducting ability more than their current conducting ability. Therefore, a magnetic field effect study is also carried out to see whether any improvement in ZT could be achieved. A detailed analysis is performed on the experimental results to gain further quantitative understanding. Conclusions are made and generalized to other nano systems.

1.3 Thesis Outline

In Chapter 2, a brief summary of the measurement system is given. Benchmark results on known samples, as well as my sample preparation techniques, are also presented. Chapter 3 presents the measurement results for all my samples. Simple trends and implications of the results without the need of any models are discussed. Chapter 4 interprets the measurement results further using my electron and phonon models that are based on semi-classical transport model. The model findings are then

discussed. Chapter 5 presents the measurements results under an applied magnetic field along with their interpretations. Finally, Chapter 6 closes with conclusions and future research directions.

Chapter 2

Measurement System and Sample Preparation Techniques

This chapter first gives a brief description of our measurement system. It follows with a comparison of my benchmark results (a) with the results provided by the apparatus' manufacture and (b) with published data. This chapter then concludes with my sample preparation techniques.

2.1 Quantum Design Physical Property Measurement System (QD PPMS)

Our main measurement system used for sample characterization is a Quantum Design (QD) Physical Property Measurement System (PPMS) (see Figure 2-1). An ULVAC Technologies Incorporated ZEM3 system [13] is also used on a few samples to demonstrate the validity of our QD PPMS apparatus measurement results. Since a detailed discussion of the QD PPMS apparatus has been given elsewhere [14, 15], only a brief description of the QD PPMS apparatus is given in this thesis. For the QD PPMS apparatus in Professor Opeil's laboratory at Boston College (BC), it has a temperature range of 2K to 400K and a magnetic field range of 0T to ±9T. In this thesis, only the Alternate Current Transport (ACT) and the Thermal Transport

System (TTO) options of the QD PPMS apparatus are used for our measurements.

Figure 2-1: Photo of a Quantum Design (QD) Physical Property Measurement System (PPMS) apparatus. For the QD PPMS apparatus in Professor Opeil's laboratory at Boston College (BC), it has a temperature range of 2K to 400K and a magnetic field range of 0T to ±9T. It has the capability to simultaneously measure the κ_{th}, S, and ρ, as well as the R_H.

Under the ACT option, Hall and 4-pt ρ measurements on the same sample are performed. On the other hand, κ_{th}, S, and 2-pt ρ measurements are performed simultaneously on the same sample under the TTO option. Both the ACT and TTO options use an AC current instead of a DC current during measurement to eliminate any unwanted Seebeck voltage. All data collected under the TTO option in this thesis use the continuous mode instead of the steady state mode, and details of the continuous mode technique have been discussed elsewhere [16, 17]. Although a magnetic field of up to ±9T can theoretically be applied in both the ACT and the TTO options, 2-pt ρ measurement results collected under the TTO option become unreliable with field magnitudes $>$ 1T. As a result, magnetoresistance measurements are only performed under the ACT option. For all the Hall measurements performed in this thesis, they are either (a) collected with at least six magnetic field values (three positive and three negative) under one current value for each temperature or (b) collected under two magnetic field values (one positive and one negative) under three different current values for each temperature. For the latter case, the magnetic field misalignment is checked at 300K with eighteen field values (nine positive and nine negative) prior to measurements at temperatures other than 300K.

2.2 QD PPMS Apparatus Benchmarking

The ability to perform correct measurements on thermoelectric samples is not a trivial task. Therefore, benchmarking with known results is a must. We first benchmark our system using a Nickel (Ni) alloys sample provided by QD (see Figure 2-2). Figure 2-3 shows that our temperature-dependent κ_{th}, S, ρ, and ZT results are in excellent agreement with the QD results. The results in Figure 2-3 clearly demonstrate the ability of our experimental set up to give reliable experimental results. However, typical thermoelectric samples have much lower κ_{th} and higher S than the Ni alloy. Therefore, Figure 2-3 demonstrates our system's ability to correctly measure ρ of typical thermoelectric samples.

Figure 2-2: Photo of a Ni alloy sample provided by QD. A US penny is placed next to it for size comparison.

To demonstrate our ability to correctly measure low κ_{th} values, we next benchmark our system using pyrex samples. Figure 2-4 shows that our κ_{th} results for pyrex are in excellent agreement with the QD results (and the constant ratio between the results simply reflects the error in measuring the dimensions of the sample). Moreover, we prepare the sample's contacts using two difference epoxies (Epo-Tek H20E and Tra-Con 816H01), and both give identical results within experimental error. Therefore, Figures 2-3 and 2-4 demonstrate that our system is working within the manufacturer's standards. Please note that due to the cracking of Epo-Tek H20E epoxy, measurement data using Epo-Tek H20E epoxy as the contact material is only available for $T >$ 175K.

Typically, our results described above are sufficient for benchmarking purposes since the QD PPMS apparatus has benchmarked its measurement capabilities against the National Institute of Standards and Technology (NIST) pyrex and stainless steel

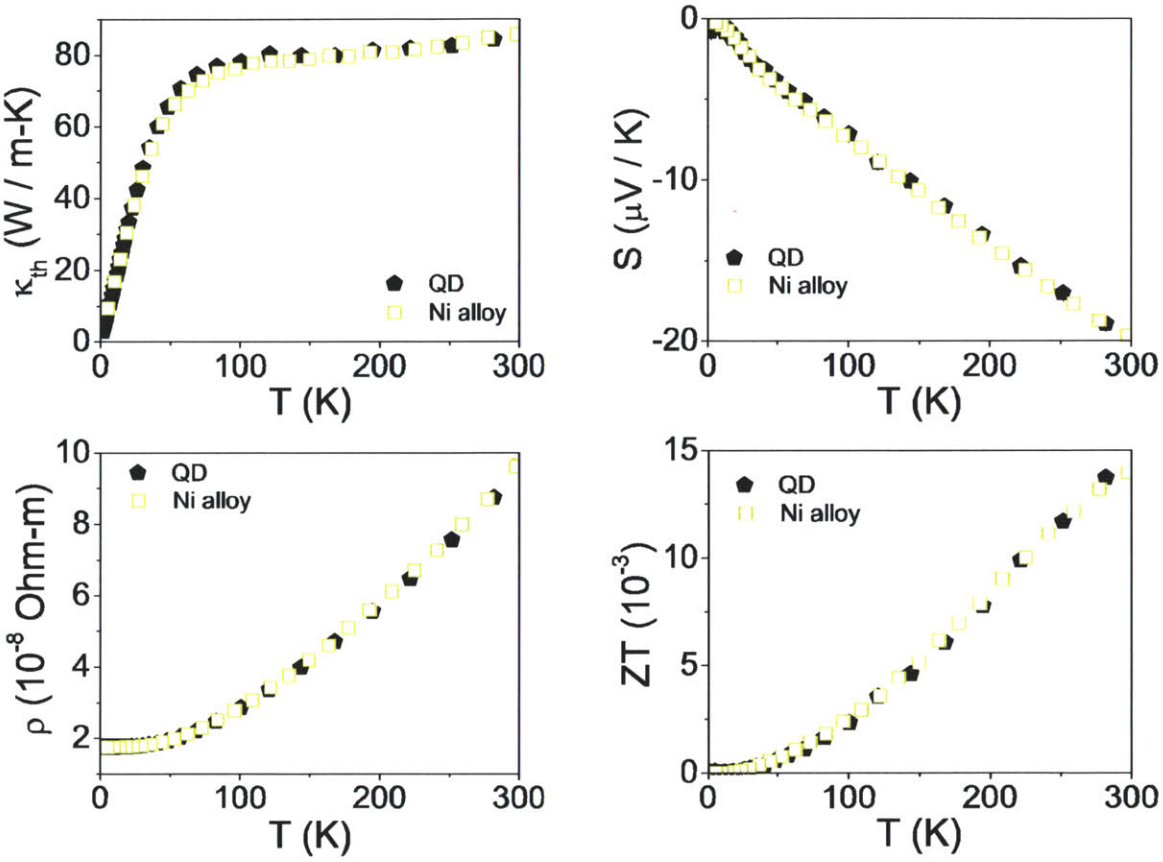

Figure 2-3: Plots of κ_{th}, S, ρ, and ZT of sample Ni alloy as a function of temperature. Also shown are the results from the manufacturer QD. Our results are in excellent agreement with the QD data. These plots demonstrate that our QD PPMS apparatus is calibrated properly relative to the manufacturer's standards.

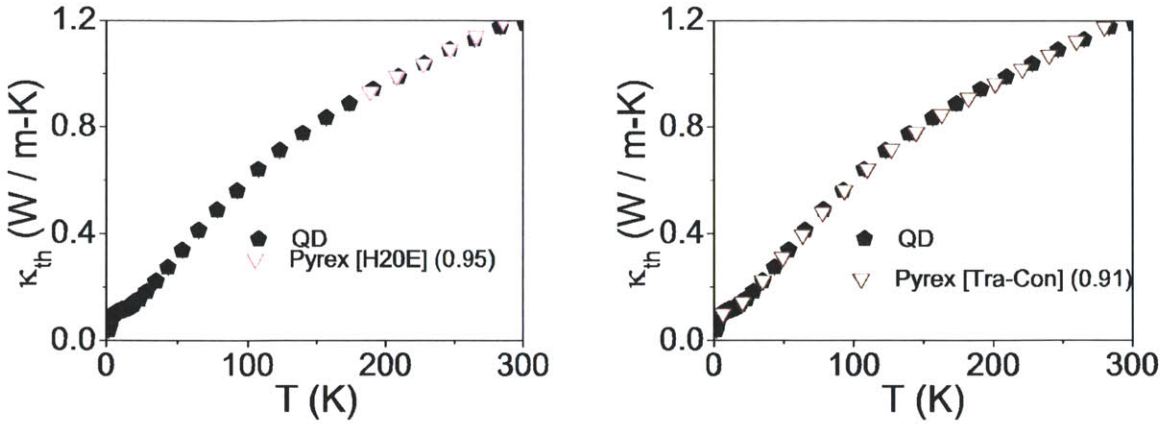

Figure 2-4: Plots of κ_{th} of sample Pyrex as a function of temperature, with the contacts prepared using both Epo-Tek H20E (left) and Tra-Con 816H01 (right) epoxies. Also shown are the results from the manufacturer QD. Our results are in excellent agreement with the QD data. These plots demonstrate that our QD PPMS apparatus is calibrated properly relative to the manufacturer's specifications. Please note that due to the cracking of Epo-Tek H20E epoxy, measurement data using Epo-Tek H20E epoxy as the contact material is only available for $T > 175$K.

samples previously [16]. Nevertheless, we decided to benchmark our system further by using known results from different measurement systems to eliminate any doubts of any measurements presented in this thesis. We first benchmark our Hall coefficient (R_H) measurements using two Copper (Cu) alloys samples, where one is provided by QD and the other one is cut from a Cu foil (see Figure 2-5). Comparison between our results with known literature data for typical Cu samples [5] confirms that our results are in excellent agreement with literature values. We then benchmark our measurements using Constantan from Alfa Aesar with published Constantan results from NIST [18]. The S results are shown in Figure 2-6 and clearly demonstrate that our system is working well within the experimental error of the common results. Lastly, we benchmark our measurements using a $(Bi_{0.2}Sb_{0.8})_2Te_3$ Ingot from the Marlow company against published data [2] (see Figure 2-7). Although overlapping data is only available in the 300K to 350K range, the values and slope around 300K for κ_{th}, S, ρ, and ZT clearly demonstrate that our measurement system gives accurate results. More importantly, the published κ_{th}, S, ρ. and ZT values for the Marlow

Ingot are measured using the Netzsch Laser Flash Apparatus (LFA) 457 MicroFlash (κ_{th}) and ULVAC Technologies Incorporated ZEM3 (S and ρ) systems instead of the QD PPMS apparatus system, giving additional evidence for the reliability of our measurements.

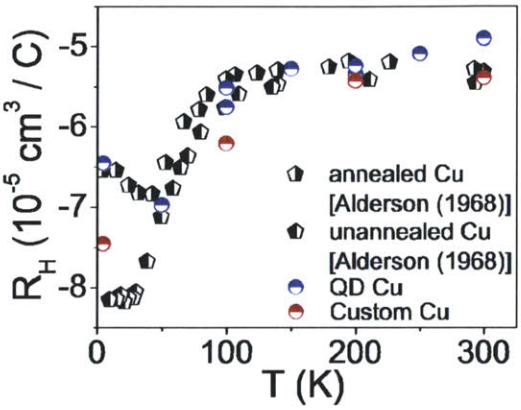

Figure 2-5: Plot of R_H of samples QD Cu and Custom Cu as a function of temperature. Also shown are the published R_H values of annealed Cu and unannealed Cu [5]. Our results are in excellent agreement with the published data. This plot demonstrates that our QD PPMS apparatus is calibrated properly.

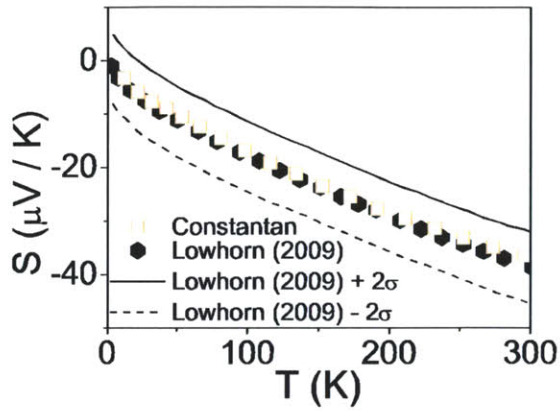

Figure 2-6: Plot of S of sample Constantan as a function of temperature. Also shown are the published S values of Constantan [5]. Our results are in excellent agreement with the published data. This plot demonstrates that our QD PPMS apparatus is calibrated properly.

Since we are extremely interested in the κ_{th} study under a magnetic field as mentioned in Section 1.2, we conclude this section with benchmarking our κ_{th} results under a magnetic field. To accomplish this task, a sample with κ_{th} independent of magnetic field is required. Pyrex is an excellent sample choice for this specific task since it is an insulator with next-to-no conducting carriers available in the temperature range below 300K. Thus, no difference between its κ_{th} values under zero applied magnetic field and under an applied magnetic field is expected. As Figure 2-8 shows, our results are in line with our expectations. Moreover, it confirms that the QD PPMS apparatus does not introduce artifacts under an applied magnetic field. As a result, any changes observed under the QD PPMS apparatus measurements in an applied magnetic field would be expected to be solely due to the sample.

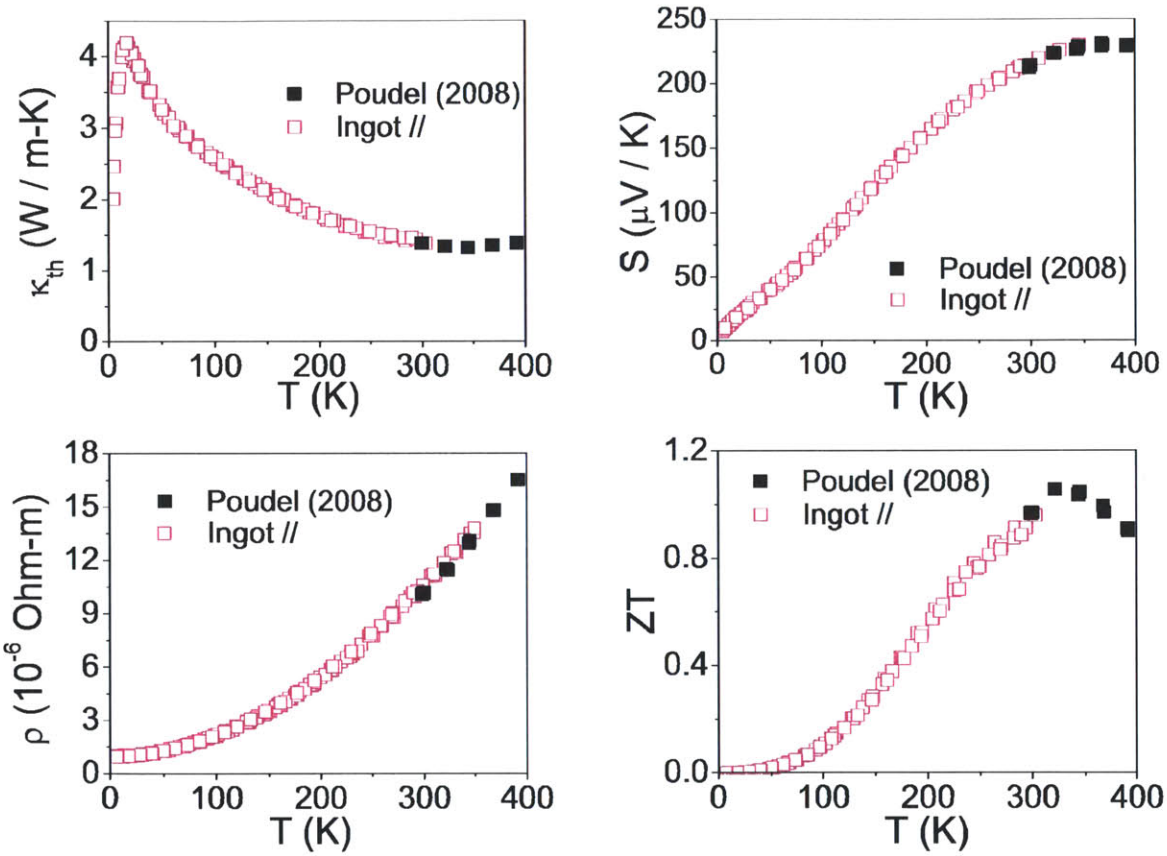

Figure 2-7: Plots of κ_{th}, S, ρ, and ZT of sample Ingot // as a function of temperature. Also shown are the published values of Ingot // [2]. Our results, both in magnitude and in slope, are in excellent agreement with the published data. This plot demonstrates that our QD PPMS apparatus is calibrated properly.

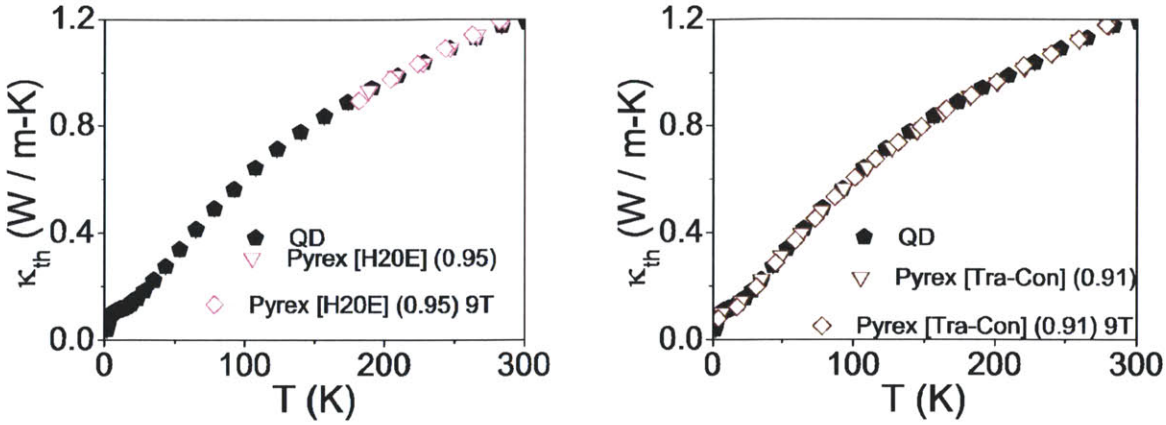

Figure 2-8: Plots of κ_{th} of sample Pyrex as a function of temperature under no applied magnetic field and under an applied magnetic field strength of 9T, with the contacts prepared using both epoxies Epo-Tek H20E (left) and Tra-Con 816H01 (right). Also shown are the zero applied magnetic field results from QD. These plots demonstrate that our QD PPMS apparatus does not introduce artifacts under an applied magnetic field.

2.3 Sample Preparation Techniques

Typical $(Bi_ySb_{1-y})_2Te_3$ received samples from our collaborators are in a cylindrical disk shape with a diameter of 0.5in and a thickness of at least 2mm. Density measurements using the Archimedes Principle and X-ray Powder Diffraction (XRD) measurements using a Bruker D8 instrument with a 2D detector are performed prior to any sample preparation procedures.

For the κ_{th}, S, and 2-pt ρ measurements under the TTO option, typical sample dimensions are a rectangular bar of $\sim$ 2mm by 2mm by 2mm. For contact purposes, two opposite surfaces of the sample are either plated with Ni or sputtered with Gold (Au) by Messrs Bo Yu and Kevin Lukas of Boston College. To ensure the accuracy of our low temperature data, our samples are soldered to the QD PPMS contact leads with a low melting temperature eutectic Bismuth Tin solder ($Bi_{58}Sn_{42}$) with the aide of Johnson Stainless Steel Flux. Lastly, the samples are sonicated in distilled water for five minutes prior to measurements. Figure 2-9 shows the contact surfaces of a typical Ni-plated and Au-sputtered TTO sample.

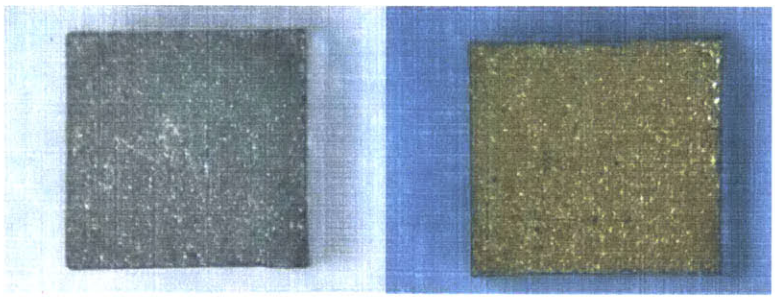

Figure 2-9: Top-view photos of a typical Ni-plated sample (left) and a typical Au-sputtered sample (right) prepared for measurements under the TTO option.

As for the Hall and 4-pt ρ measurements under the ACT option, typical sample dimensions are a rectangular bar of $\sim$ 1mm by 2mm by 10mm. To make electrical connection to the sample, contacts are prepared by using either: (a) 2 mil (= 0.002in) Platinum (Pt) wires that are spark-welded to the 10mm by 2mm surfaces or (b) 6 mil (= 0.006in) Cu wires that are soldered to one of the already Au sputtered 10mm by 2mm surface (see Figure 2-10). Finally, the sample is wired to the sample holder accordingly.

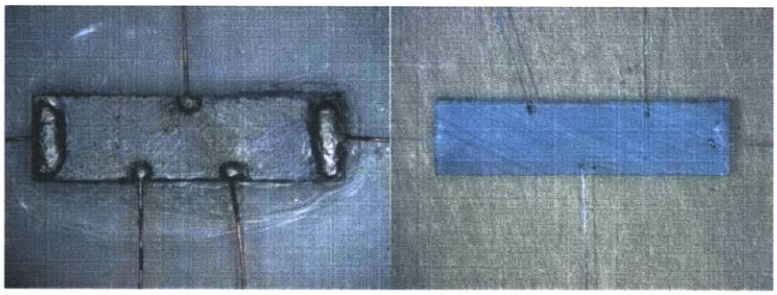

Figure 2-10: Top-view photos of a typical sample prepared for measurements under the ACT option. The left side shows a typical sample with Cu wires soldered to its Au-sputtered surface, and the right side shows a typical sample with Pt wires spark-welded to its polished surfaces.

THIS PAGE INTENTIONALLY LEFT BLANK

Chapter 3

$(Bi_ySb_{1-y})_2Te_3$ Measurement Results

This chapter first gives a brief introduction to the $(Bi_ySb_{1-y})_2Te_3$ materials system. It then follows with the measurement results of our $(Bi_ySb_{1-y})_2Te_3$ bulk and nanocomposite samples. The chapter concludes with a discussion of a simple analysis of the results and leads to a more in-depth discussion of the results in the next chapter.

3.1 $(Bi_ySb_{1-y})_2Te_3$ Introduction

Since detailed reviews of $(Bi_ySb_{1-y})_2Te_3$ have been published previously [3, 19, 4, 20], only a brief summary of the properties of this materials system is presented here. $(Bi_ySb_{1-y})_2Te_3$ is an alloys of Bi_2Te_3 and Sb_2Te_3, which can be prepared over the entire $0 \leq y \leq 1$ composition range. Both Bi_2Te_3 and Sb_2Te_3 have a rhombohedral lattice structure that belongs to the space group $R\bar{3}m$ and contains five atoms along the trigonal axis in the sequence of Te1-Bi-Te2-Bi-Te1 (or Te1-Sb-Te2-Sb-Te1) (see Figure 3-1) [6, 21, 22]. As a result, $(Bi_ySb_{1-y})_2Te_3$ also possesses the rhombohedral lattice structure, except that the Bi and Sb isoelectronic atoms are randomly distributed. Bi_2Te_3, Sb_2Te_3, and $(Bi_ySb_{1-y})_2Te_3$ are always found to be p-type materials in their stoichiometrical balanced form. Other than Sb_2Te_3, these materials can become n-type by doping with excess Te [23, 24] or Iodine [25]. Unlike other well-known ma-

terials systems, such as Silicon, carriers in these V-VI systems are generated through anti-site substitutions [26]. Depending on the alloying in $(Bi_ySb_{1-y})_2Te_3$, its indirect energy gap ranges from 140meV for Bi_2Te_3 to 290meV for Sb_2Te_3 [7, 27, 28, 29]. $(Bi_ySb_{1-y})_2Te_3$ has six equivalent electron pockets [30, 31, 32] and six equivalent hole pockets [32, 33, 34]. Unfortunately, satisfactory agreeable results on the locations of the band extrema are yet to be achieved, except that they lie in the $\hat{y}$-$\hat{z}$ plane. For instance, one group reported that the conduction band minima and the valence band maxima of Bi_2Te_3 lie along the Λ' [100] and $\triangle$ [110] directions in the Brillouin zone, with the conduction band minima located at a distance of 0.1 $|\Gamma A|$ from point A and the valence band maximum located at a distance of (0.3-0.5) $|\Gamma X|$ from point Γ [7]. On the other hand, another group reported (in rhombohedral unit cell coordinates) that the valence band maxima and conduction minima of Bi_2Te_3 are located at (0.650, 0.584, 0.584) and at (0.652,0.585,0.585), respectively [33, 34]. This group also reported that the valence band maxima and conduction minima of Sb_2Te_3 are located at (0.695,0.613,0.613) and at (0.690,0.605,0.605), respectively. Thus, further study on the electronic structure of alloy $(Bi_ySb_{1-y})_2Te_3$ is needed.

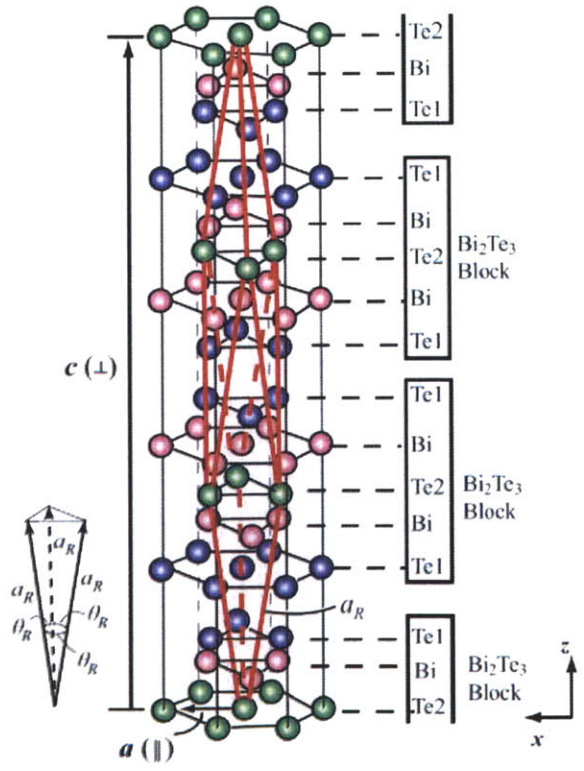

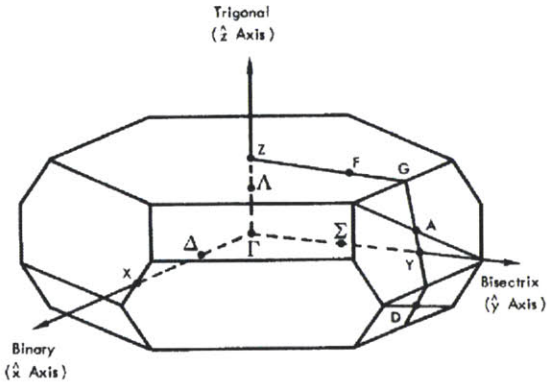

Figure 3-1: Bi_2Te_3's crystal structure in the hexagonal lattice (color black) and in the rhombohedral lattice (color red) [6]. Also shown is its first Brillouin zone for the rhombohedral cell and the high symmetry points are indicated where Γ denotes the center of the first Brillouin zone [7, 8].

Since the 1960s, Bi_2Te_3 and $(Bi_ySb_{1-y})_2Te_3$ have become well-known for their good thermoelectric performance from 200K to 300K [4]. Therefore, refrigeration is the primary application for these materials in this temperature range.

3.2 Description of Samples

A total of eight $(Bi_ySb_{1-y})_2Te_3$ samples are measured in this thesis. The sample set includes: (a) one bulk ingot sample manufactured by Marlow (Ingot), (b) four nanocomposite samples (XY21, XY146, XY144, and GJ99) made by collaborators from Boston College (BC) where the letters simply indicate the sample maker's initials, and (c) three nanocomposite samples (0%, 40%, and 100%) made by collaborators from Nanyang Technological University (NTU) in Singapore, where the % denotes the weight % of the nanoinclusions prepared via melt spinning [1] in the sample. All the nanocomposite samples in this thesis are made solely for research uses and are purposely fabricated under conditions different than the best samples previously reported [2, 1]. All received nanocomposite samples are in a cylindrical disk shape with a diameter of 0.5in and a thickness of at least 2mm, while the Ingot is in a cylindrical disk shape with a diameter of 1in and a length of at least 12mm. Relating the sample's shape to its fabrication conditions, the cylindrical disk axis of any nanocomposite sample is always parallel to its press direction, whereas the Ingot's cylindrical disk axis is parallel to its growth direction.

3.3 Sample Nomenclature

It is well-known that the $(Bi_ySb_{1-y})_2Te_3$ sample is highly anisotropic and has the best thermoelectric properties along the growth direction (the cylindrical disk axis) [35]. Therefore all transport measurements on the Ingot sample are only performed parallel to the growth direction (denoted by //).

As for the nanocomposite samples, an isotropic behavior is expected from the random orientation of all the nanoparticles in the nanocomposite sample. Nevertheless,

a small anisotropic behavior is expected to be observed since pressure is applied only along the cylindrical disk axis during fabrication. Moreover, due to the layer nature of the melt spinning procedure, samples with nanoinclusions prepared via melt spinning are believed to possess a small anisotropy in them. Therefore, the anisotropy of the nanocomposite samples is checked. For bookkeeping, // and $\perp$ denote transport measurements measured parallel and perpendicular to the cylindrical disk axis (the press direction), respectively.

As mentioned in Chapter 2, κ_{th}, S, and 2-pt ρ measurements are carried out under the TTO option, whereas Hall and 4-pt ρ measurements are carried out under the ACT option. Due to the sample size requirement for the ACT option, Hall and 4-pt ρ measurements cannot be performed in both the // and $\perp$ directions for all samples. For selected samples, various strengths of magnetic field up to 9T are also applied along with the current (I) and heat (Q) transport measurements. $B//Q$ is used to denote measurements with the applied magnetic field being parallel to the transport direction, whereas $B \perp Q$ denotes measurements with the applied magnetic field being perpendicular to the transport direction. Figure 3-2 schematically shows examples of measurement conditions for TTO and ACT samples under the $B \perp Q$ scenario.

Since there are eight samples investigated in this thesis, along with the various experimental conditions that are available, a comprehensive and consistent sample labeling system is necessary. Table 3.3 summarizes the color and symbol of the sample nomenclature for all temperature-dependent plots used in this thesis. Let us use an example to better clarify the notations. For sample 40% //, a pink $\diamond$ is used to represent the B=9T TTO measurements (κ_{th}, S, and 2-pt ρ) under the $B \perp Q$ condition.

3.4 Non-Transport Measurement Results

All samples studied in this thesis have the composition $(Bi_{0.2}Sb_{0.8})_2Te_3$. The theoretical density of a material at this composition at 300K is 6.776g/cm^3. Table 3.2 lists the

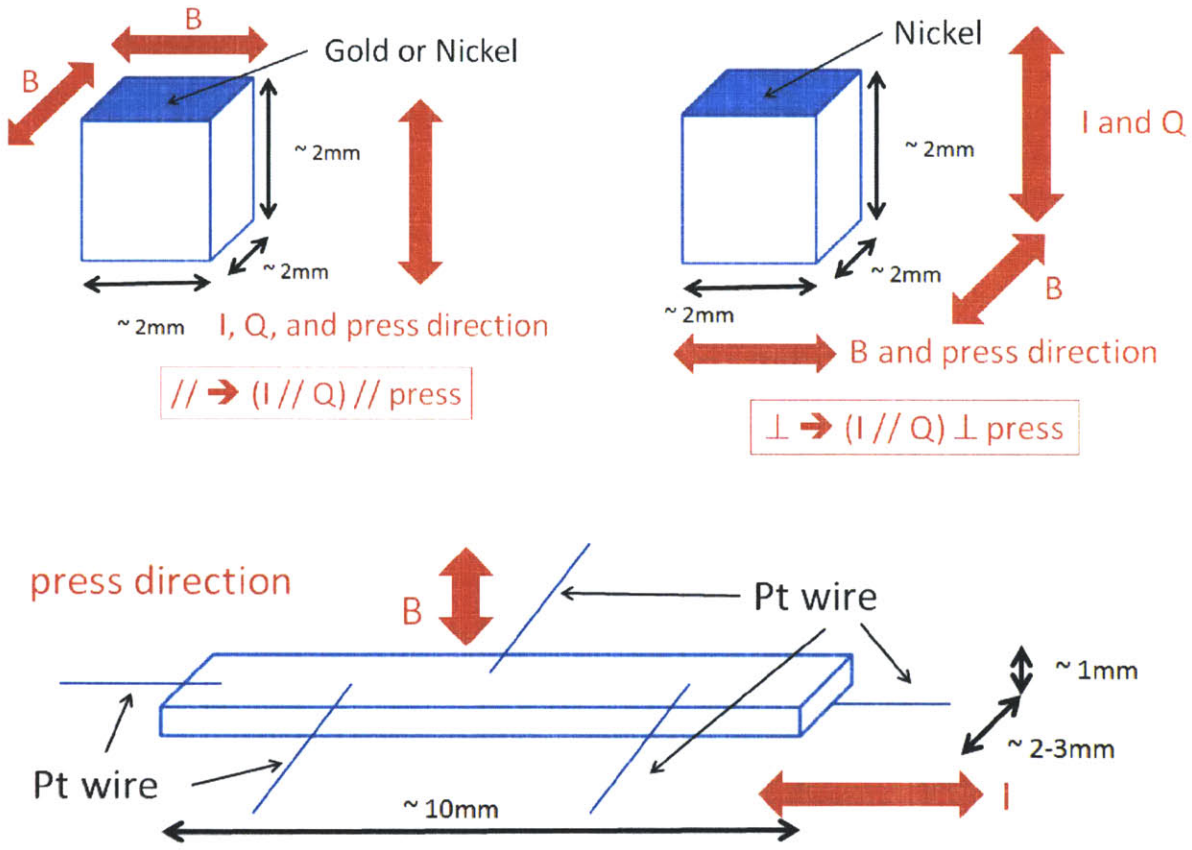

Figure 3-2: Examples of measurement conditions for TTO (top) and ACT (bottom) samples under the $B \perp Q$ scenario.

Table 3.1: Sample nomenclature for all temperature-dependent plots in this thesis. // and ⊥ denote transport data measured parallel and perpendicular to the cylindrical disk axis, respectively. B // Q and B ⊥ Q denote measurements with the applied magnetic field being parallel and perpendicular to the transport direction, respectively. Please see Section 2.1 for the definitions of TTO, ACT, and ZEM3.

Sample	*Color*
Reference	**Black**
QD Ni alloy	**Yellow**
Pyrex [Tra-Con]	**Wine**
Pyrex [H20E]	**Light Magenta**
QD Cu	**Light Blue**
Custom Cu	**Dark Red**
Constantan	**Light Orange**
Ingot	**Magenta**
XY21	**Red**
XY146	**Olive**
XY144	**Blue**
GJ99	**Dark Yellow**
0%	**Purple**
40%	**Pink**
100%	**Gray**
κ_L extraction	**Violet**
κ_L extraction without 40% and 100%	**Green**
κ_L extraction (BC samples)	**Light Cyan**

Reference Data	
Ingot [Poudel (2008)]	■
Quantum Design	⬟
Annealed Cu [Alderson (1968)]	◮
Unannealed Cu [Alderson (1968)]	◭
Constantan [Lowhorn (2009)]	⬢

κ_L *Extraction Temperature (K)*	⊥	//
297K	▼	▼
201K	◆	◆
101K	◀	◀
50K	▶	▶
26K	◐	◒
all T	▼	

Measurement Conditions			*TTO*	*ACT*	*ZEM3*
//	B // Q	0T	□		⬒
		1T	○		
		3T	⬡		
		6T	+		
		9T	△		
	B ⊥ Q	0T	▽	◫	
		1T	×	⊕	
		2T	⊠	⊠	
		3T	✳	⧋	
		4T	⊗	⊗	
		5T	⧻	⧻	
		6T	⊟	⧩	
		7T	⧻	⧻	
		8T	⊠	⊠	
		9T	◇	◈	
		all B		◓	
⊥	B // Q	0T	☆		◨
		1T	⊖		
		3T	⧋		
		6T	⧩		
		9T	⬠		
	B ⊥ Q	0T	◁	◭	
		1T	◈	◮	
		2T	⧻	⧻	
		3T	☆	⊕	
		4T	⧻	⧻	
		5T	⧻	⧻	
		6T	⊖	☆	
		7T	⊠	⊠	
		8T	✳	✳	
		9T	▷	◭	
		all B		◑	

300K mass density of all samples studied in this thesis found using Archimedes Principle. Two interesting observations are noted: (a) although BC and NTU use different starting materials, different fabrication machines, and different fabrication parameters, the resulting densities of the nanocomposites from the ball-milled nanopowders alone (XY21, XY146, XY144, GJ99, and 0%) are almost identical. (b) The addition of nanoinclusions prepared via melt spinning decreases the sample mass density somewhat.

Table 3.2: Sample's density at 300K. Mass density measurements are performed using the Archimedes Principle.

Sample	*Density (g/cm^3)*	*% of theoretical density*
Theoretical $(Bi_{0.2}Sb_{0.8})_2Te_3$	6.776	100
Ingot	6.358	93.83
XY21	6.724	99.23
XY146	6.718	99.14
XY144	6.732	99.35
GJ99	6.565	96.88
0%	6.718	99.14
40%	6.602	97.44
100%	6.444	95.10

Figure 3-3 shows the results of the XRD measurements taken on all my samples at 300K. All XRD measurements are performed with the Cu alpha X-rays (40kV and 30mA) hitting the plane perpendicular to the cylindrical disk axis of the sample. A few distinguishing differences exist between the BC and NTU samples. They are: (a) both NTU and BC samples have the same peak locations, (b) NTU samples have a lower intensity for peaks (1 0 10) and (1 1 0), and (c) NTU samples have a higher intensity for peaks (0 0 ς) where ς is an integer. Comparing the XRD patterns with the reference database, the difference in peak intensities is a good indication that the NTU samples are not completely randomized and have internal prefer orientations.

The surface structure of each sample at 300K is also examined using scanning electron microscopy (SEM) with a JEOL 6340F instrument (see Figure 3-4). The plane of examination is either parallel to the press direction for nanocomposite sam-

ples or parallel to the growth direction for the ingot sample. The SEM images show that the NTU samples and the BC samples are markedly different. For example, the BC samples are shown to have grains in the μm range with a small distribution (Figures 3-4(b)-(d)). On the other hand, the grain size of NTU samples decreases with the addition of nanoinclusions prepared via melt spinning. Moreover, the SEM images show that the NTU samples have a wider grain size distribution that ranges from nm to μm. This observed difference is believed to arise from the difference in the fabrication techniques incorporated by the BC and NTU teams.

3.5 Transport Measurement Results

This section shows the results of the temperature-dependent κ_{th}, S, and ρ measurements under no applied magnetic field (see Figures 3-5 to 3-7 and A-1 to A-4), along with the carrier concentration measurement results (see Figure 3-9). Since there are a total of seven nanocomposite samples and each sample is measured in both the // and $\perp$ directions, there are a total of fourteen results for each thermoelectric property. Thus, it would be extremely confusing to put all the results in one plot, except in rare specific cases. To display the data in an elegant fashion, each nanocomposite sample's results are displayed together only with the Ingot // results unless otherwise noted. Moreover, repeated measurement results under the same conditions are represented only using one symbol for simplicity purposes. Furthermore, the error bar for each data point is not shown unless it is larger than the size of the symbol. Additionally, a data display control is used. This control tool selects up to only one out of every fifty data points being displayed, depending on the number of measurements performed on the sample and the density of the collected data. This approach allows the symbols to be displayed clearly in the data plots. For example, the ρ results for Ingot // are composed of results from six measurements on three different Ingot // samples. The measurements include: (a) three repeated measurements on one TTO Ingot // sample with data collected for approximately every 2.5K, (b) one measurement on another TTO Ingot // sample with data collected for approximately every 2.5K, and

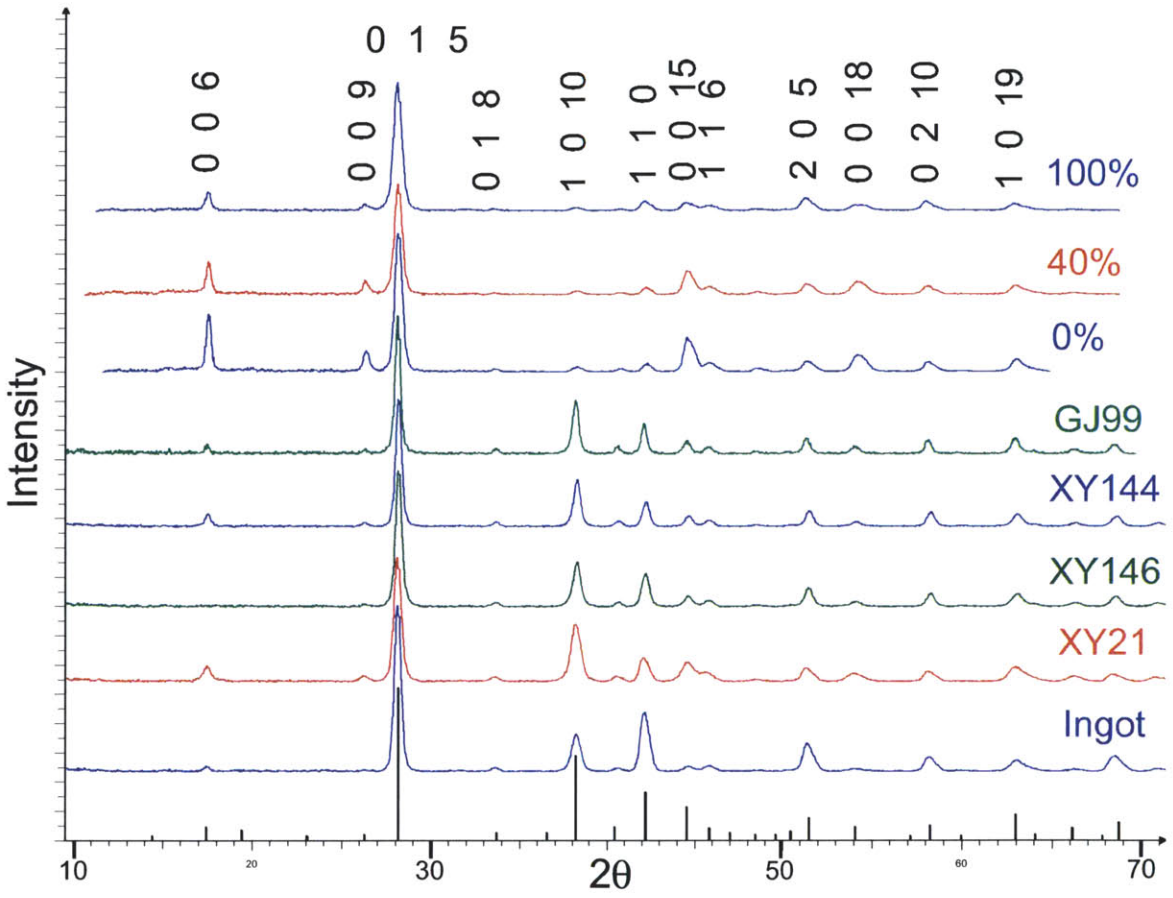

Figure 3-3: XRD results of all samples taken at 300K. All XRD measurements are performed with the Cu alpha X-rays (40kV and 30mA) hitting the plane perpendicular to the cylindrical disk axis of the sample. A few distinguishing differences exist between the BC and NTU samples. They are: (a) both NTU and BC samples have the same peak locations, (b) NTU samples have a lower intensity for peaks (1 0 10) and (1 1 0), and (c) NTU samples have a higher intensity for peaks (0 0 ς) where ς is an integer.

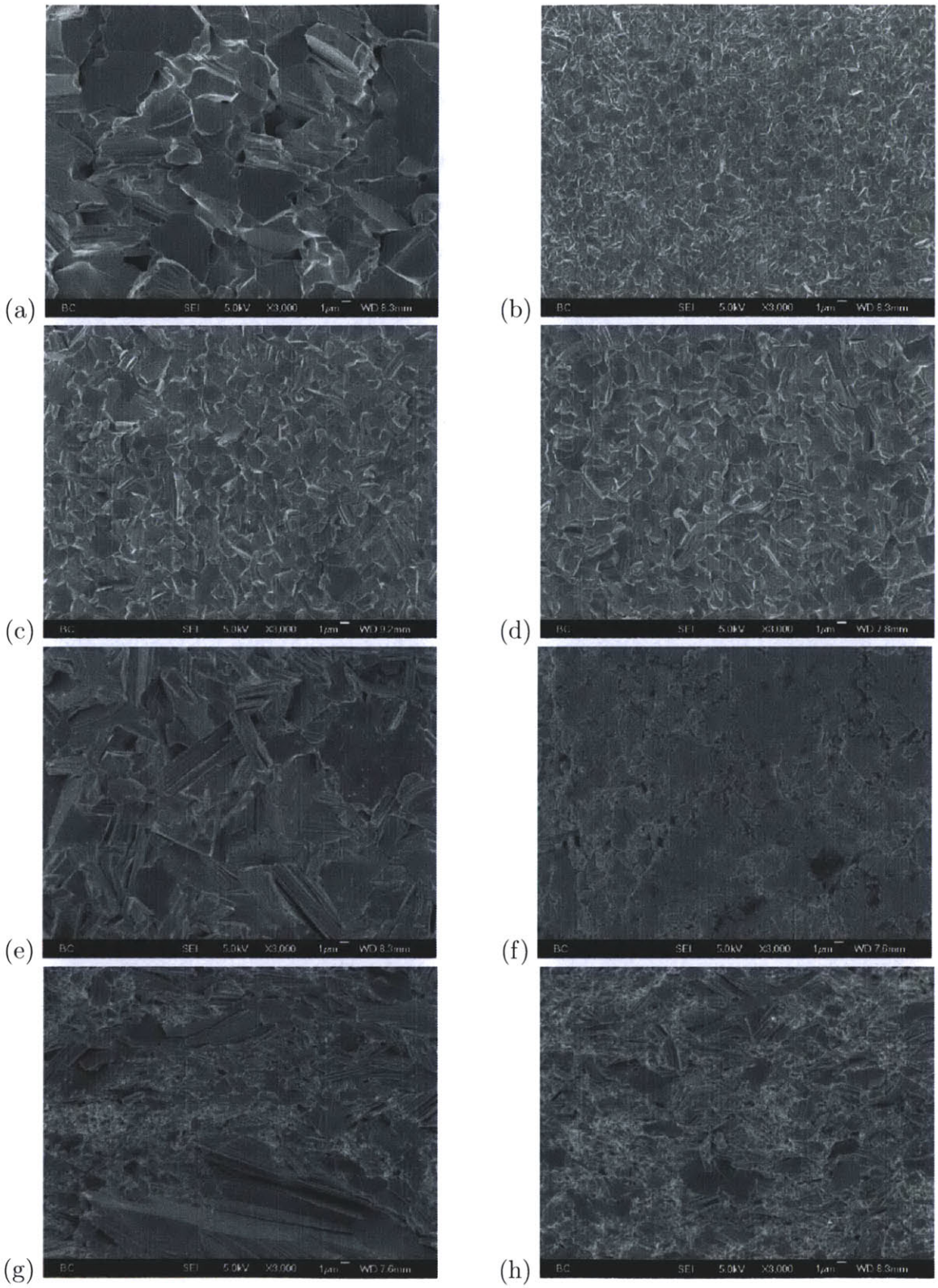

Figure 3-4: SEM images of samples (a) Ingot, (b) XY21, (c) XY146, (d) XY144, (e) GJ99, (f) 0%, (g) 40%, and (h) 100%. All SEM images are taken at x3000 magnification. Clear differences in structure is observed among the different samples.

(c) two repeated measurements on one ACT Ingot // sample with data collected for each 1K. To display the data clearly, a data display control of one out of every ten to thirty points being displayed is used for the Ingot //'s ρ results. Lastly, to help ease the reader's experience, only a few representative results are presented in the chapter with the rest of the results put in the Appendices for further reference.

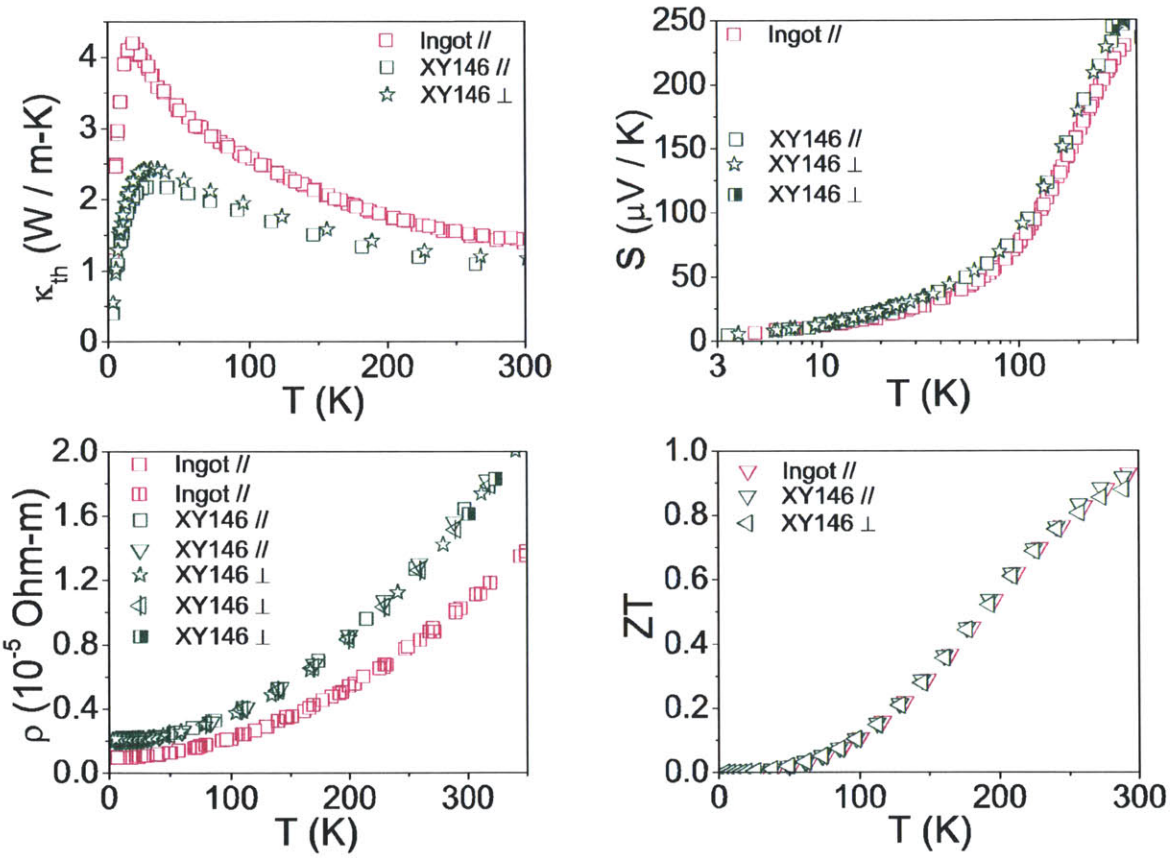

Figure 3-5: Plots of κ_{th}, S, ρ, and ZT of samples XY146 and Ingot // as a function of temperature. Anisotropic behavior is observed in κ_{th} and ρ, but not in S. No significant difference is observed between results from (a) QD PPMS vs. ZEM3, and (b) 2-pt ρ (TTO) vs. 4-pt ρ (ACT) (see Table 3.3 for the representation of each symbol and color). A data display control is used for sample XY146 to show only one out of every two to thirty points, while a data display control is used for sample Ingot // to show only one out of every five to thirty points.

Carrier concentration data in Figure 3-9 are collected under conditions described in Section 2.1. Together with Figure 3-8, these data clearly show that all samples are

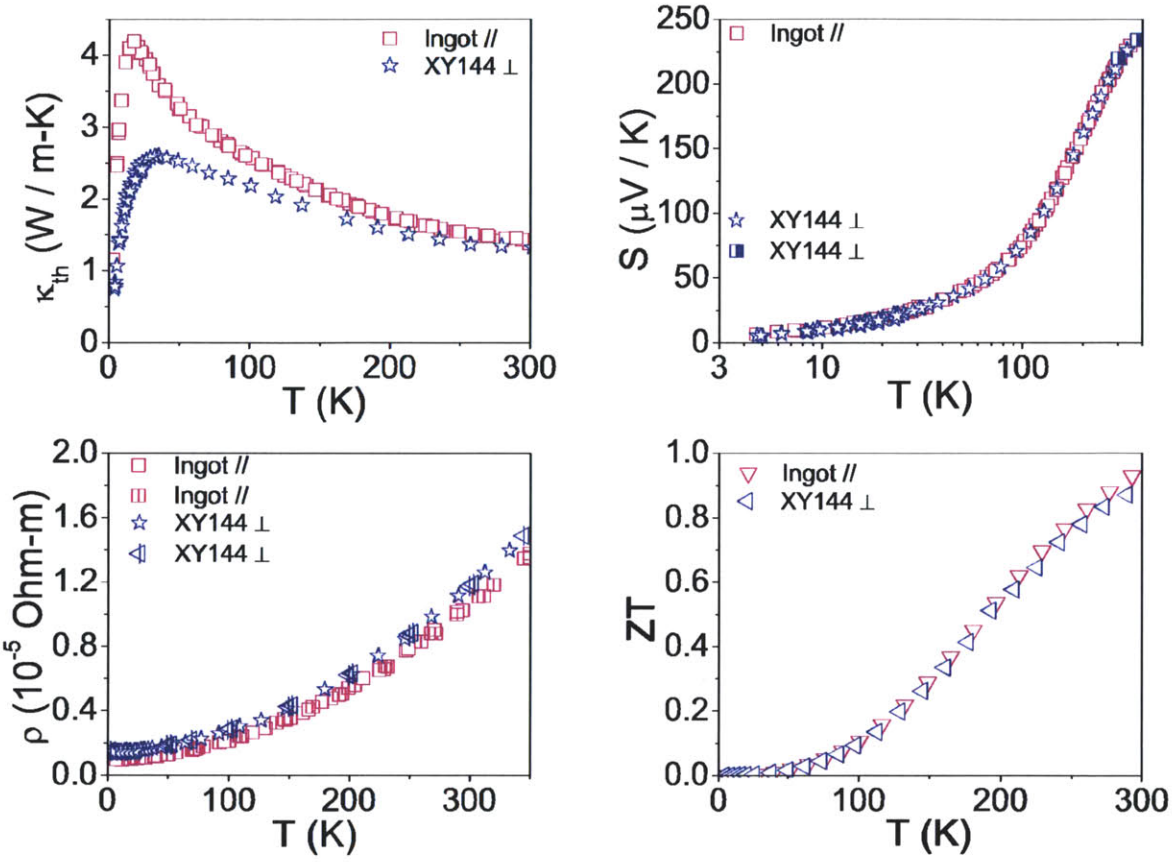

Figure 3-6: Plots of κ_{th}, S, ρ, and ZT of samples XY144 $\perp$ and Ingot // as a function of temperature. No significant difference is observed between results from (a) QD PPMS vs. ZEM3, and (b) 2-pt ρ (TTO) vs. 4-pt ρ (ACT) (see Table 3.3 for the representation of each symbol and color). A data display control is used for sample XY144 to show only one out of every two to fifty points, while a data display control is used for sample Ingot // to show only one out of every five to thirty points.

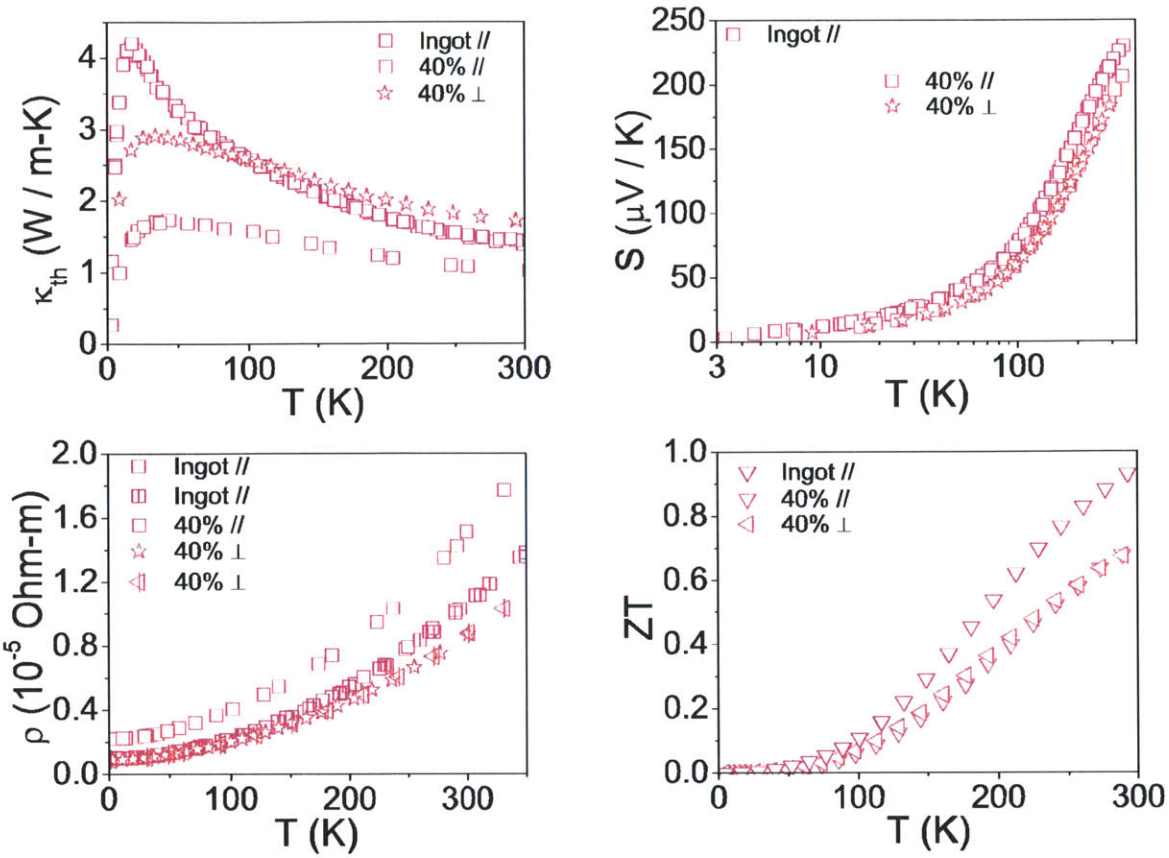

Figure 3-7: Plots of κ_{th}, S, ρ, and ZT of samples 40% and Ingot // as a function of temperature. Anisotropic behavior is observed in κ_{th} and ρ, but not in S. No significant difference is observed between results from 2-pt ρ (TTO) vs. 4-pt ρ (ACT) (see Table 3.3 for the representation of each symbol and color). A data display control is used for sample 40% to show only one out of every three to thirty points, while a data display control is used for sample Ingot // to show only one out of every five to thirty points.

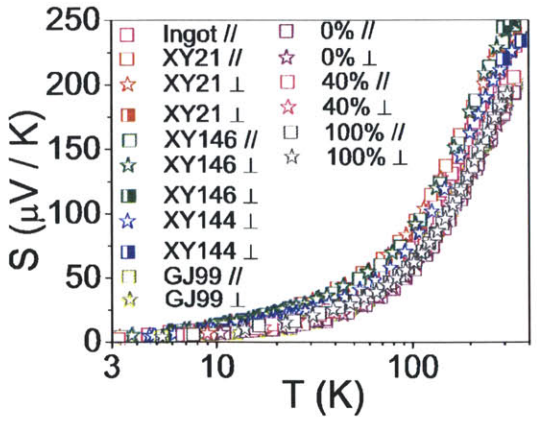

Figure 3-8: Plot of S of all seven nanocomposite samples and Ingot // as a function of temperature. Two similar trends are observed among all samples: (a) a constant slope $\partial S/\partial T$ at low temperature ($T < 20$K) and (b) a constant slope $\partial S/\partial ln(T)$ of $\sim$ 130-140μV/ln(K) from 200K to 300K.

p-type and follow a similar trend. We also notice that a higher carrier concentration leads to a lower Seebeck value, as expected. The observed hole concentration difference among all samples is believed to arise from the difference in grain size and point defect concentration among all nanocomposite samples investigated. This observed difference is in line with the observed difference in the S values among all samples. More on the relationship between S and carrier concentration will be discussed in Chapter 4. Due to an unexpected sample cracking during measurement, the data for sample XY146 $\perp$ are extrapolated from 100K down to 5K. The small difference between XY21 // and XY21 $\perp$ is believed to arise from the unavoidable imperfect rectangular shape of our samples (see Figure 3-10).

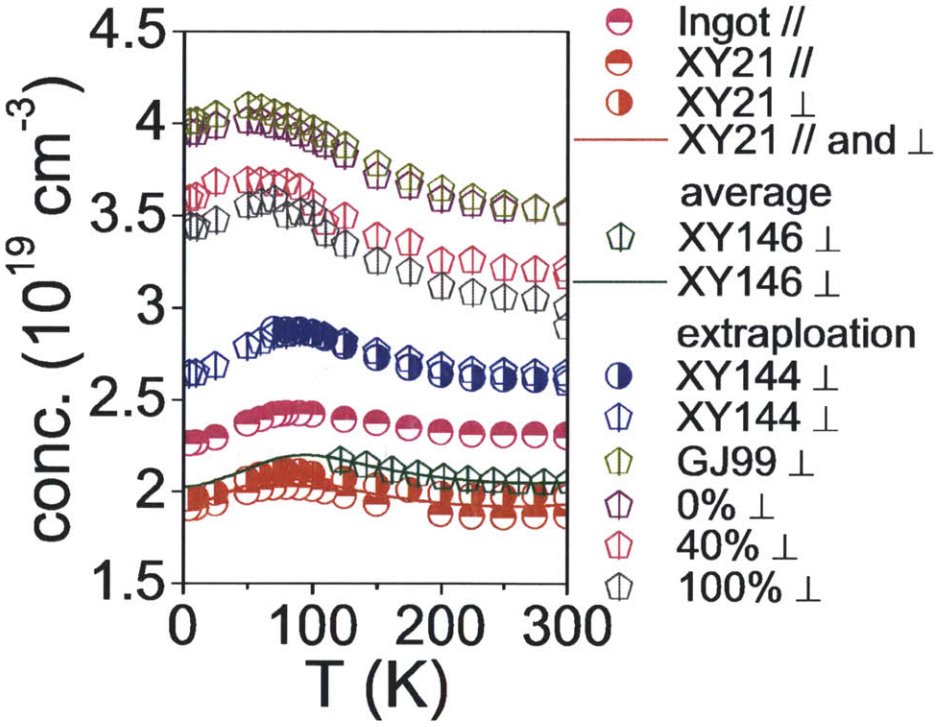

Figure 3-9: Plot of carrier concentration of all samples as a function of temperature below 300K. The data are collected under conditions described in Section 2.1. This plot shows that all measured samples follow a similar trend.

Figures 3-5 to 3-7 together with Figures A-1 to A-4 clearly suggest that there is no measurable difference found between our 2-pt ρ (TTO) and 4-pt ρ (ACT) measurements. In fact, any constant ratio difference between our measurements arises mainly

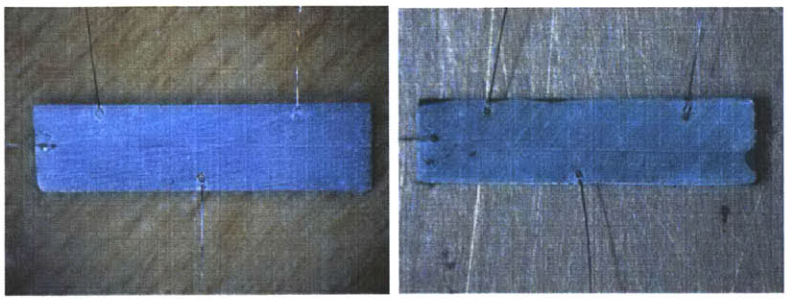

Figure 3-10: XY21 // (left) and XY21 $\perp$ (right) samples prepared for the Hall measurements. As can be seen from the photos, the samples are not in a perfect rectangular bar shape as desired. It is believed that this imperfect shape contributes to the slight difference in the Hall results from samples XY21 // and XY21 $\perp$.

from the uncertainty in measuring the dimensions of the samples. As mentioned in Section 2.3, the contact surfaces of the TTO samples in this thesis are prepared with either Ni or Au. The XY146 // samples are prepared using both methods to test whether any difference in the ρ results exists between the two surface materials used for the electrical contacts. Figure 3-11 redisplays the ρ results of Figure 3-5 with the symbols purposely filled with the contact material's color. As Figure 3-11 suggests, there is no observable difference in the ρ results between the cases when Au or Ni are used as the contact surface material.

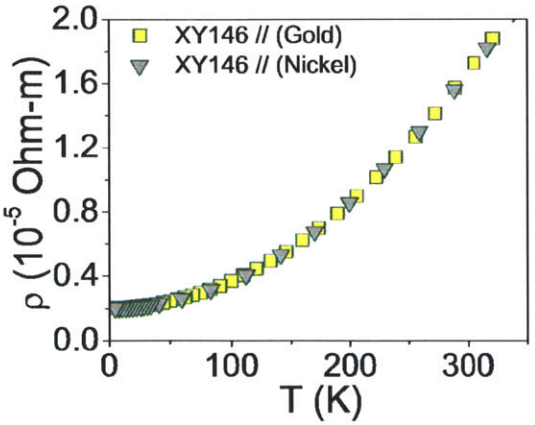

Figure 3-11: Comparison of the temperature dependence of ρ for sample XY146 // prepared using Ni and Au as the contact surface material. The symbols are purposely filled with the contact material's color. The results clearly suggest that there is no observable difference in the ρ results between using Au and Ni as the contact surface material.

A closer look at Figures 3-5 to 3-7 together with Figures A-1 to A-4 reveals numerous similarities between all nanocomposite samples. These similarities include:

- anisotropic behavior in κ_{th} and ρ
- isotropic behavior in S
- existence of a peak at low temperature in κ_{th}
- dramatic decrease in the peak value of κ_{th} for the nanocomposite samples when compared with the Ingot //'s value
- constant slope $\partial S/\partial T$ for $T < 20$K
- constant slope $\partial S/\partial ln(T)$ of $\sim$ 130-140μV/ln(K) for 200K $< T <$ 300K
- close-to-zero slope in ρ for $T < 20$K
- $\rho \propto T^{1.5\pm0.1}$ for 200K $< T <$ 300K

In fact, if all the S data are plotted together (see Figure 3-8), the results clearly show that S follows the same physics for all samples. This will be explained further in Chapter 4. For now, we extract the similarities among all samples investigated and list these results in Tables 3.3 and 3.4. Please note that the slightly bigger difference in the S vs. $ln(T)$ slope between the // and $\perp$ results coming from the NTU samples is mainly due to the number of data points used for the slope calculation. For the NTU samples, an average of ten data points are available for the slope calculation, whereas at least twenty data points are available for the slope calculation of the BC samples.

Anisotropic behavior is observed in κ_{th} and ρ for all the nanocomposite samples investigated, with the anisotropy being always higher in ρ than in κ_{th}. To get a quantitative sense of the anisotropy, data at 297K are extracted for comparison and the anisotropy % in this thesis is defined as

$$ani\ \% = (100\%)\frac{|value_{\perp} - value_{//}|}{value_{\perp}}. \tag{3.1}$$

Table 3.5 gives a good reminder that the fabrication process plays a vital role in the

Table 3.3: ρ features for all samples investigated in the temperature ranges $T < 20$K and 200K $< T <$ 300K. These trends are extracted from the data presented in Figures 3-5 to 3-7 and A-1 to A-4. Two similar trends are observed: (a) for $T < 20$K, the nanocomposite samples have ρ values measured in the $\perp$ direction that are always lower than the values in the // direction, except for sample XY146, and (b) for 200K $< T <$ 300K, $\rho \propto T^{1.5\pm0.1}$ for all samples investigated.

Property	*Temperature range*	*Sample*	*Feature*
ρ	$T < 20$K	Ingot //	$\approx 1.02\mu$Ohm-m
		XY21 //	$\approx 3.50\mu$Ohm-m
		XY21 $\perp$	$\approx 2.81\mu$Ohm-m
		XY146 //	$\approx 2.09\mu$Ohm-m
		XY146 $\perp$	$\approx 2.09\mu$Ohm-m
		XY144 $\perp$	$\approx 1.46\mu$Ohm-m
		GJ99 //	$\approx 1.62\mu$Ohm-m
		GJ99 $\perp$	$\approx 1.30\mu$Ohm-m
		0% //	$\approx 1.40\mu$Ohm-m
		0% $\perp$	$\approx 0.706\mu$Ohm-m
		40% //	$\approx 2.23\mu$Ohm-m
		40% $\perp$	$\approx 0.940\mu$Ohm-m
		100% //	$\approx 3.43\mu$Ohm-m
		100% $\perp$	$\approx 1.69\mu$Ohm-m
	200K $< T <$ 300K	Ingot //	$\propto T^{1.60}$
		XY21 //	$\propto T^{1.40}$
		XY21 $\perp$	$\propto T^{1.46}$
		XY146 //	$\propto T^{1.64}$
		XY146 $\perp$	$\propto T^{1.62}$
		XY144 $\perp$	$\propto T^{1.58}$
		GJ99 //	$\propto T^{1.44}$
		GJ99 $\perp$	$\propto T^{1.45}$
		0% //	$\propto T^{1.56}$
		0% $\perp$	$\propto T^{1.61}$
		40% //	$\propto T^{1.54}$
		40% $\perp$	$\propto T^{1.60}$
		100% //	$\propto T^{1.38}$
		100% $\perp$	$\propto T^{1.52}$

Table 3.4: S features for all samples investigated in the temperature ranges 200K $< T <$ 300K. These trends are extracted from the data presented in Figures 3-5 to 3-7 and A-1 to A-4. A similar trend is found among all samples investigated. For 200K $< T <$ 300K, a slope value of 130-140μV/K in S vs. $ln(T)$ is observed for all samples investigated.

Property	*Temperature range*	*Sample*	*Feature*
S vs. $ln(T)$ slope	200K $< T <$ 300K	Ingot //	$\approx$ 141.06μV/ln(K)
		XY21 //	$\approx$ 139.72μV/ln(K)
		XY21 $\perp$	$\approx$ 139.30μV/ln(K)
		XY146 //	$\approx$ 142.66μV/ln(K)
		XY146 $\perp$	$\approx$ 144.57μV/ln(K)
		XY144 $\perp$	$\approx$ 137.40μV/ln(K)
		GJ99 //	$\approx$ 126.93μV/ln(K)
		GJ99 $\perp$	$\approx$ 124.60μV/ln(K)
		0% //	$\approx$ 131.68μV/ln(K)
		0% $\perp$	$\approx$ 124.5μV/ln(K)
		40% //	$\approx$ 135.34μV/ln(K)
		40% $\perp$	$\approx$ 130.35μV/ln(K)
		100% //	$\approx$ 140.08μV/ln(K)
		100% $\perp$	$\approx$ 136.58μV/ln(K)

Table 3.5: κ_{th} and ρ of all nanocomposite samples measured at 297K in both // and $\perp$ directions. Anisotropy in each sample is quantitatively determined using Equation 3.1.

Sample	$\kappa_{th,//}$ *(W/m-K)*	$\kappa_{th,\perp}$ *(W/m-K)*	κ_{th} *ani %*	$\rho_{//}$ *(μOhm-m)*	$\rho_{\perp}$ *(μOhm-m)*	ρ *ani %*
XY21	1.069	1.143	6.47	16.95	15.05	12.62
XY146	1.060	1.172	9.56	16.37	15.83	3.41
XY144		1.327	N/A		11.56	N/A
GJ99	1.257	1.469	14.43	10.33	8.625	19.77
0%	1.119	1.634	31.52	11.36	7.187	58.06
40%	1.027	1.715	40.12	14.81	8.486	74.52
100%	1.060	1.428	25.77	16.40	10.80	51.85

anisotropic behavior of a nanocomposite sample. Thus, care needs be taken during the fabrication process to ensure that no unwanted anisotropic behavior is introduced. As mentioned in Section 3.2, all nanocomposite samples measured in this thesis are made solely for research uses and are purposely fabricated under conditions different from that of the best samples previously reported [2, 1].

3.5.1 Hole Mobility

Before we delve into the various scattering mechanisms embedded in our κ_{th}, S, and ρ data (see Chapter 4), let us take a step back and look at the quantities that do not require the knowledge of the scattering times. The hole mobility μ_p is one of such quantities where

$$\mu_p = R_H/\rho. \tag{3.2}$$

Figures 3-12 to 3-15 together with Figures B-1 to B-6 show the temperature-dependent hole mobility results for all samples investigated. A few observations are worth noting. First, the nanocomposite approach decreases the values of the mobility. The difference is more pronounced as the temperature decreases. Second, the mobility values are always lower in the // direction for nanocomposite samples than in the $\perp$ direction. Finally, the mobility increases with decreasing temperature for both the Ingot // and the nanocomposite samples.

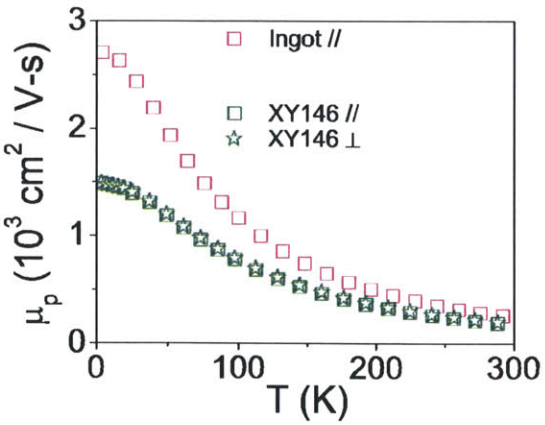

Figure 3-12: Plot of the hole mobility μ_p of samples XY146 and Ingot // as a function of temperature.

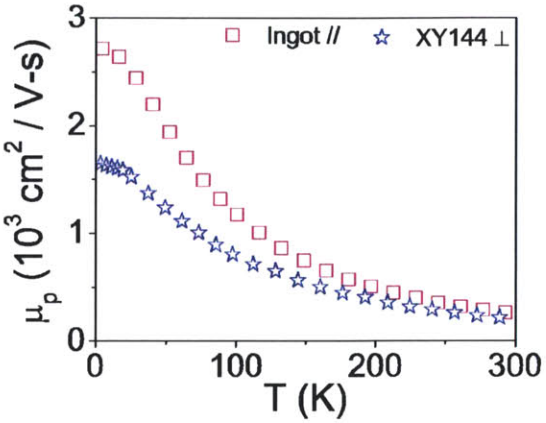

Figure 3-13: Plot of the hole mobility μ_p of samples XY144 and Ingot // as a function of temperature.

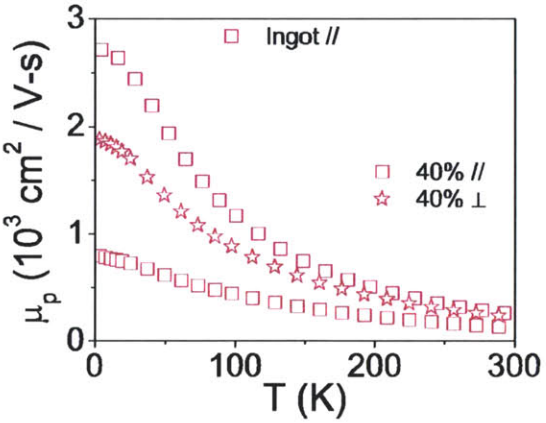

Figure 3-14: Plot of the hole mobility μ_p of samples 40% and Ingot // as a function of temperature.

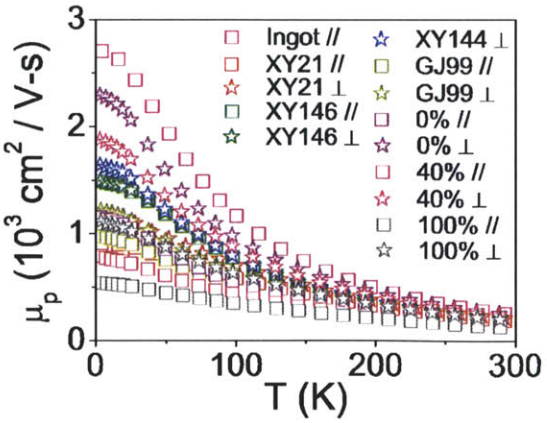

Figure 3-15: Plot of the hole mobility μ_p of all samples investigated as a function of temperature.

3.5.2 Mean Free Path

Following the hole mobility extraction, we now extract the mean free path for both the holes and phonons.

Hole Mean Free Path

In Drude's model [36], the electrical conductivity σ is defined as

$$\sigma = ne^2\tau_e/m^*_{cond}, \tag{3.3}$$

where τ_e is the time the conduction carriers travel without collision, n is the carrier concentration, and m^*_{cond} is the conduction effective mass for the carriers. Assuming the conducting carriers have a velocity v_e (see Equation 4.23), then the mean free path is

$$\ell_e = \frac{m^*_{cond}v_e}{\rho ne^2}. \tag{3.4}$$

Using the m^*_{cond} and v_e from Chapter 4, Figures 3-16 to 3-18 together with Figures C-1 to C-4 show the results of the temperature-dependent hole mean free path. Similar to the case for the mobility, the nanocomposite approach decreases the hole mean free path relative to the bulk ingot. Moreover, ℓ_e is found to be lower in the // direction than in the $\perp$ direction for all nanocomposite samples investigated. Finally, ℓ_e in general is 3 orders of magnitude smaller than ℓ, the average diameter of the grain boundaries (see Section 4.2).

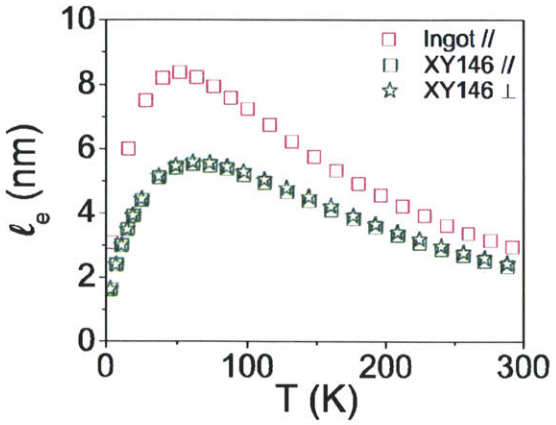

Figure 3-16: Plot of the hole mean free path of samples XY146 and Ingot // as a function of temperature.

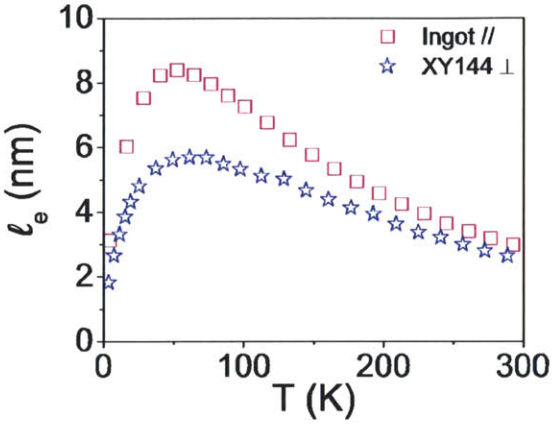

Figure 3-17: Plot of the hole mean free path of samples XY144 and Ingot // as a function of temperature.

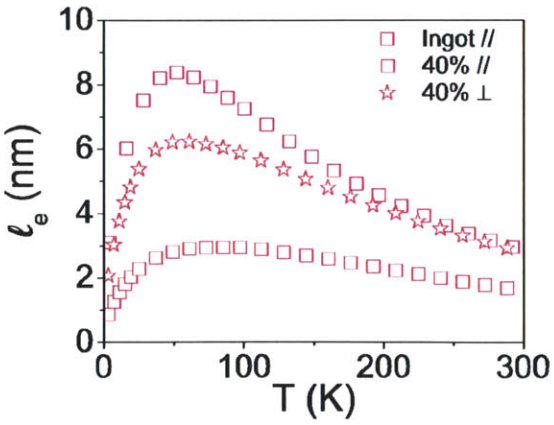

Figure 3-18: Plot of the hole mean free path of samples 40% and Ingot // as a function of temperature.

Phonon Mean Free Path

Using simple kinetic theory under the Debye approximation [37], the lattice thermal conductivity κ_L is defined as

$$\kappa_L = \frac{1}{3} C_v v_s \ell_{ph}, \tag{3.5}$$

$$C_v = 9\frac{N}{\delta^3} k_B \left(\frac{T}{\theta_D}\right)^3 \int_0^{\theta_D/T} \frac{x^4 \exp^x}{(\exp^x - 1)^2} dx, \tag{3.6}$$

$$\tag{3.7}$$

where C_v is the heat capacity per unit volume, v_s is the sound velocity, θ_D is the Debye temperature, N is the number of atoms in a unit cell, and δ^3 is the unit cell volume. Using the θ_D and v_s values from Chapter 4, Figures 3-19 to 3-21 together with Figures D-1 to D-4 show the results of the temperature-dependent phonon mean free path. Because ℓ_{ph} spans over 2 orders of magnitude, log scale is used in plotting ℓ_{ph}. Similar to the case of the mobility, the nanocomposite approach decreases the value of phonon mean free path relative to the bulk ingot. Moreover, ℓ_{ph} is found to be lower in the // direction than in the $\perp$ direction for all nanocomposite samples investigated. Furthermore, ℓ_{ph} has the same temperature dependence for all samples investigated. Finally, ℓ_{ph} in general is 3 orders of magnitude smaller than ℓ (see Section 4.2), except in the low temperature regime ($T < 50$K). Therefore, if one wants to decrease the κ_{th}, a possible solution is to decrease ℓ further. However, in order not to affect the ρ too much, the lower limit for ℓ should be in the nm ranges. As a result, decreasing ℓ would have the biggest effect on κ_{th} at the low temperature regime. Please note that the increase in the phonon mean free path as T decreases is in general due to the decrease in Umklapp scattering at low T.

3.5.3 Lattice Thermal Conductivity κ_L

Another quantity of interest is the κ_{th} values of the nanocomposite samples when ρ reaches infinity (or $\sigma = 1/\rho$ reaches 0). In this instance, $\kappa_e \rightarrow 0$ and $\kappa_{th} \rightarrow \kappa_L$. Please be advised that this approximation is only valid for samples of the same

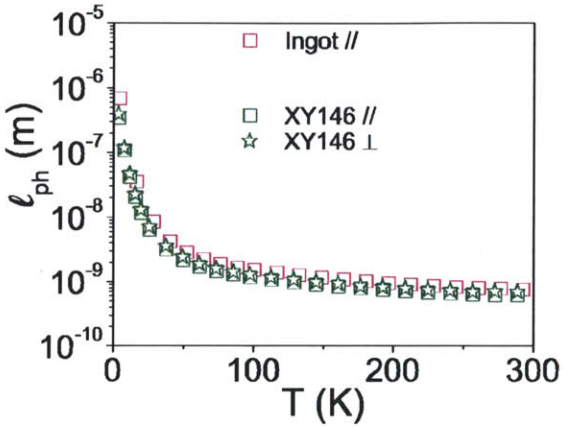

Figure 3-19: Plot of phonon mean free path of samples XY146 and Ingot // as a function of temperature.

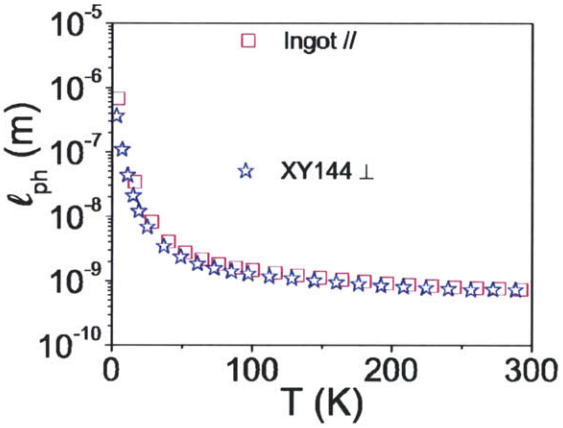

Figure 3-20: Plot of phonon mean free path of samples XY144 and Ingot // as a function of temperature.

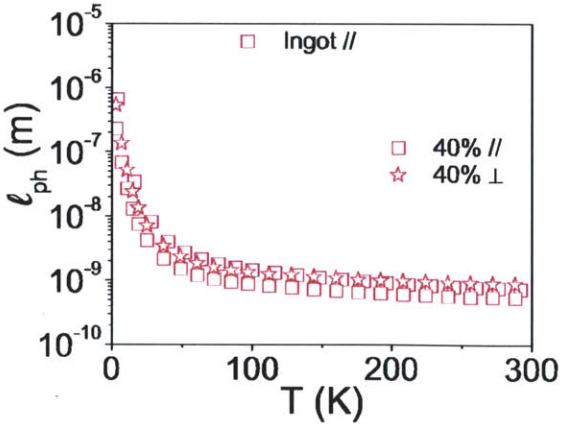

Figure 3-21: Plot of phonon mean free path of samples 40% and Ingot // as a function of temperature.

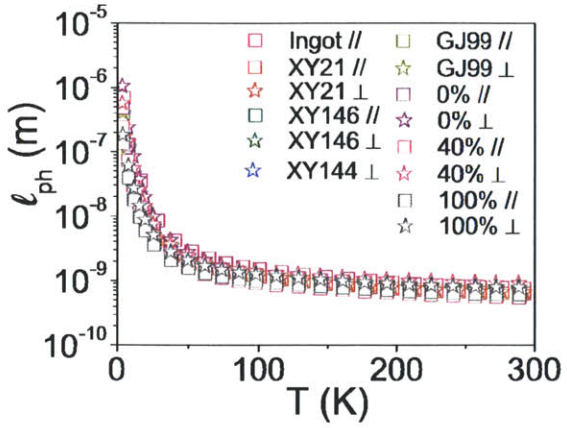

Figure 3-22: Plot of phonon mean free path of all samples investigated as a function of temperature.

materials system that have similar grain sizes (i.e., a similar grain boundary scattering contribution). As reported previously, κ_L at 300K is 1.4W/m-K and 0.9W/m-K for bulk Bi_2Te_3 and bulk $(Bi_{0.3}Sb_{0.7})_2Te_3$, respectively [3, 4]. It is believed that the alloys $(Bi_{0.3}Sb_{0.7})_2Te_3$ has the lowest 300K κ_L values in the $(Bi_ySb_{1-y})_2Te_3$ system. The following are the general steps used for the κ_L value extraction:

1. numerous samples from the same materials system are fabricated
2. measurements are carried out to obtain the κ_{th} and σ values for each sample at various temperatures
3. a plot of κ_{th} vs. σ for all samples is generated for each chosen temperature
4. a best linear fit is applied to the κ_{th} vs. σ plot for each chosen temperature
5. the y-intercept (when σ=0) of the best linear fit is deemed as the κ_L value of the materials system at each chosen temperature

Since different manufacturers build their machines differently, it is likely that the BC and NTU nanocomposite samples cannot be regarded as the same group of materials system in the // direction. However, since all of the nanocomposite samples are fabricated in a 0.5in die with no pressure coming from the side, it is likely that the samples can be treated as the same group of materials system in the ⊥ direction. Lastly, the addition of nanoinclusions prepared via melt spinning in the 40% and 100% nanocomposite samples probably causes deviations in the κ_{th} values from those for the nanocomposite samples made purely from ball-milled particles. Figures 3-23

and 3-24 show κ_{th} as a function of σ for all the nanocomposite samples in the $\perp$ direction at a few interpolated temperatures (297K, 201K, 101K, 50K, and 26K) with and without the 40% and 100% NTU nanocomposite samples, respectively. On the other hand, Figures 3-25 and 3-26 show κ_{th} as a function of σ for all the nanocomposite samples in the // direction at the same set of interpolated temperatures with and without the NTU nanocomposite samples, respectively. Please be advised that more data are needed for Figure 3-26 to further confirm the trend, which is based only on three samples. Table 3.6 summarizes the κ_L extracted using the data in Figures 3-24 and 3-26, and Figure 3-27 graphically displays the $\kappa_{L,\perp}$ results. Since Umklapp scattering is known to be the dominate phonon scattering mechanism in the 300K regime for the $(Bi_ySb_{1-y})_2Te_3$ materials system [38], thus $\kappa_L(297K) > \kappa_L(300K)$. As a result, Figures 3-23 to 3-26 and Table 3.6 show that using the nanocomposite approach can further decrease the already low alloys κ_L values. Using the 297K case as an example, the nanocomposite $\kappa_{L,\perp}$ of 0.76W/m-K is 0.14W/m-K lower than the previously reported 0.9W/m-K κ_L(300K) value for $(Bi_{0.3}Sb_{0.7})_2Te_3$. And this decrease in κ_L is one of the reasons for the previously reported observations of an improvement in ZT in nanocomposite systems [2, 39].

Table 3.6: κ_L values extracted using the data in Figures 3-24 and 3-26. This table shows that using the nanocomposite approach can further decrease the already low alloys κ_L values as seen in the 300K case (going from 0.9W/m-K to 0.76W/m-K). This table also shows the existence of anisotropy in our nanocomposite samples.

T (K)	$\kappa_{L,\perp}$ *of nanocomposite samples fabricated using ball-milled nanoparticles (W/m-K)*	$\kappa_{L,//}$ *of BC nanocomposite samples (W/m-K)*
297	0.76	0.75
201	0.81	0.75
101	1.18	1.06
50	1.53	1.31
26	1.36	1.18

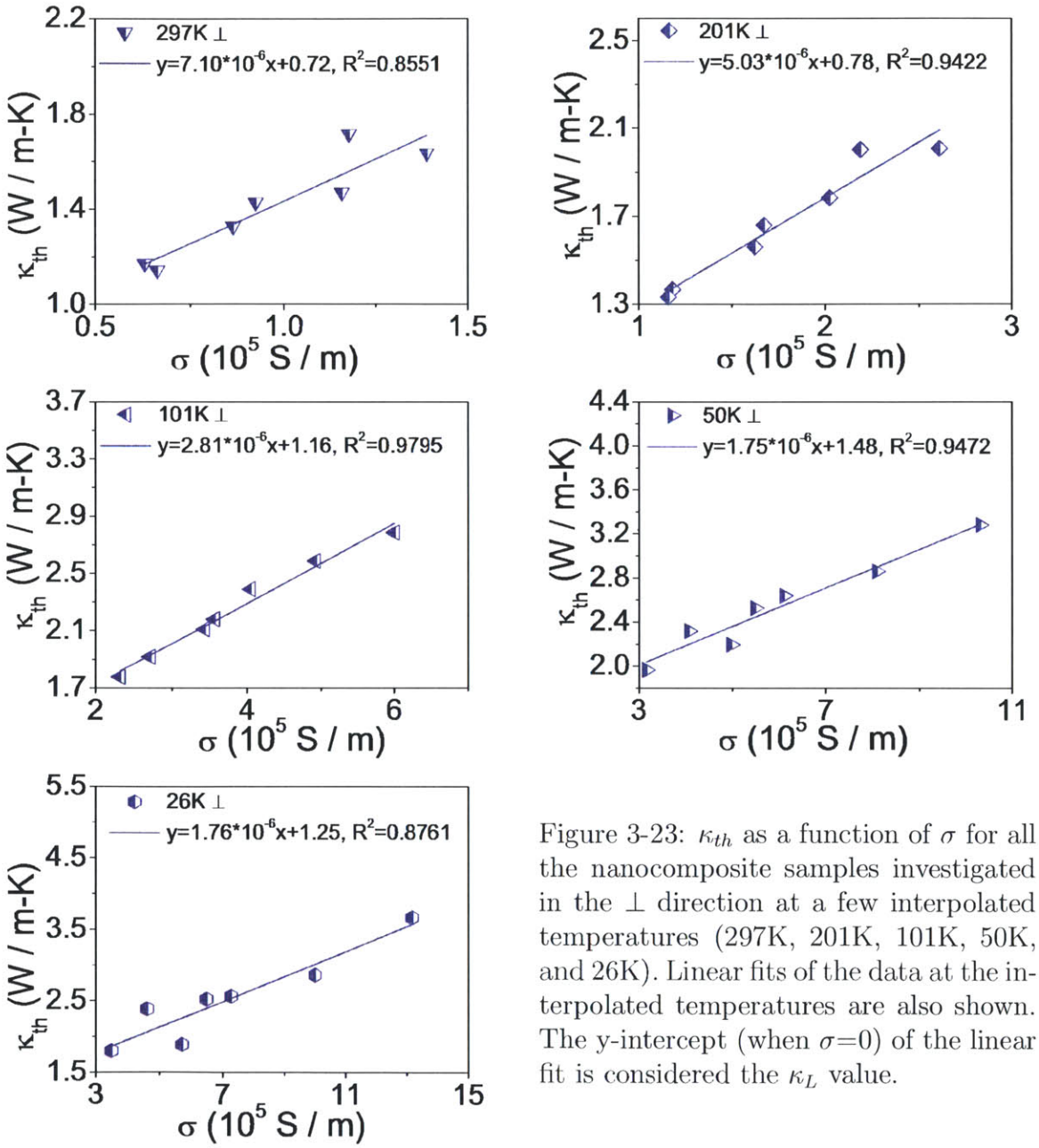

Figure 3-23: κ_{th} as a function of σ for all the nanocomposite samples investigated in the $\perp$ direction at a few interpolated temperatures (297K, 201K, 101K, 50K, and 26K). Linear fits of the data at the interpolated temperatures are also shown. The y-intercept (when σ=0) of the linear fit is considered the κ_L value.

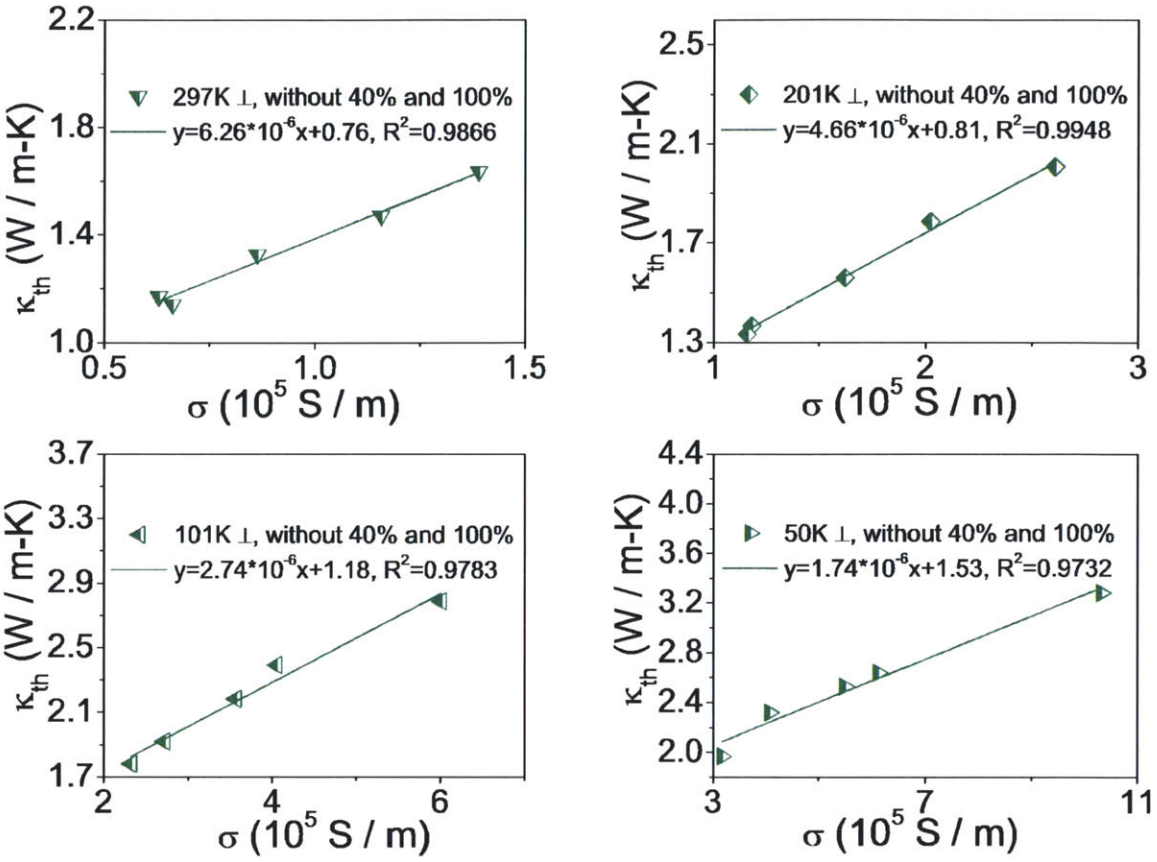

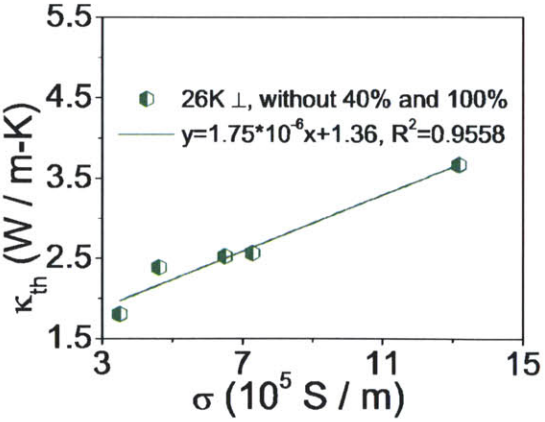

Figure 3-24: κ_{th} as a function of σ for five of the nanocomposite samples investigated (*without the 40% and 100% NTU nanocomposite samples*) in the $\perp$ direction at a few interpolated temperatures (297K, 201K, 101K, 50K, and 26K). Linear fits of the data at the interpolated temperatures are also shown. The y-intercept (when σ=0) of the linear fit is considered the κ_L value. As the plots show, κ_{th} vs. σ produce an excellent linear fit relationship (with $R^2 > 0.95$) when using data from nanocomposite samples fabricated using only ball-milled nanoparticles. This set of data produces a much better κ_{th} vs. σ linear relationship than those in Figure 3-23

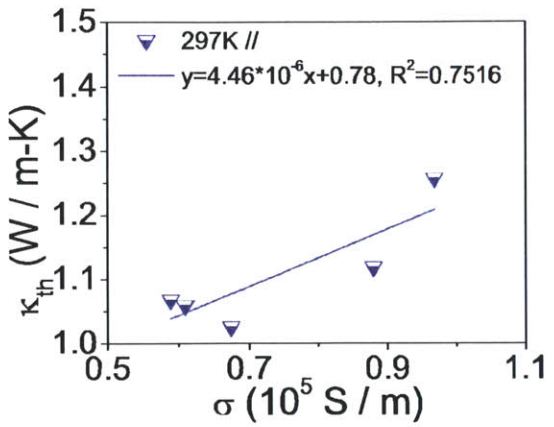

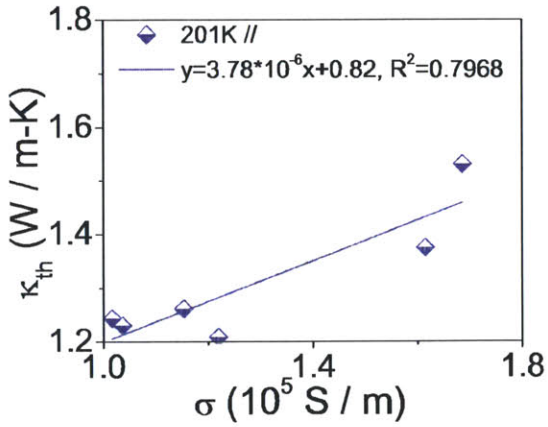

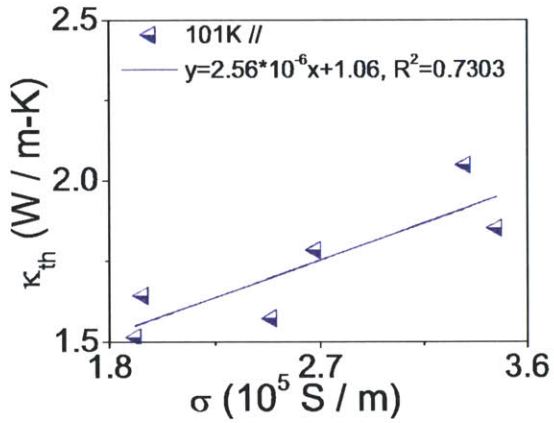

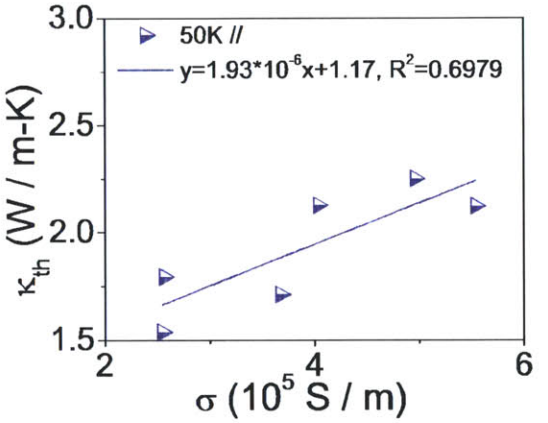

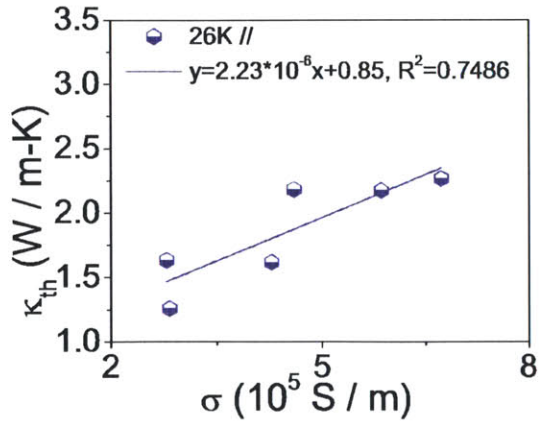

Figure 3-25: κ_{th} as a function of σ for all the nanocomposite samples investigated in the // direction at a few interpolated temperatures (297K, 201K, 101K, 50K, and 26K). Linear fits of the data at the interpolated temperatures are also shown. The y-intercept (when σ=0) of the linear fit is considered the κ_L value. As the plots show, κ_{th} and σ have a rather poor linear fit relationship ($R^2 < 0.8$) when using data from all seven nanocomposite samples investigated.

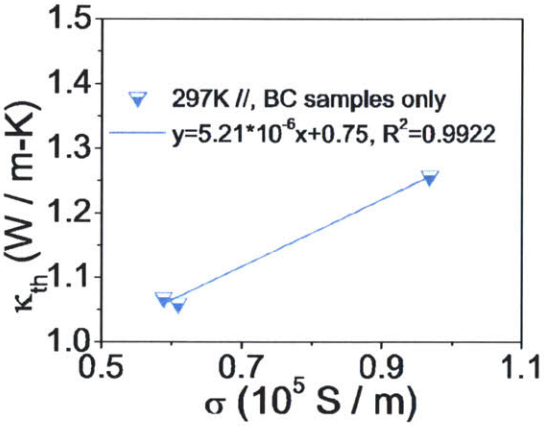

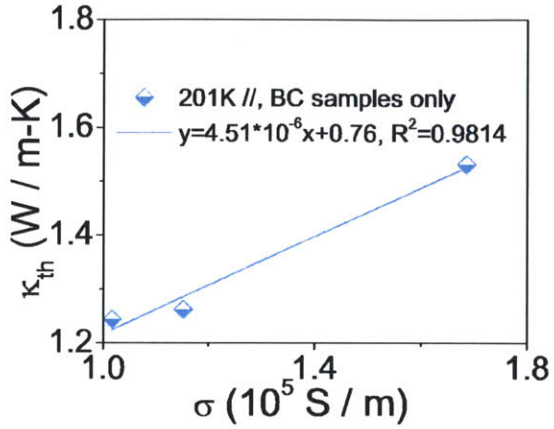

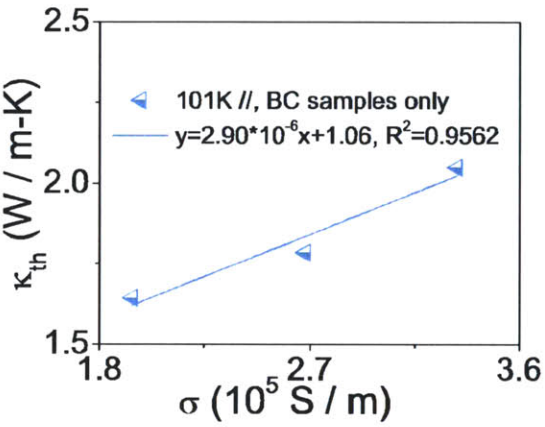

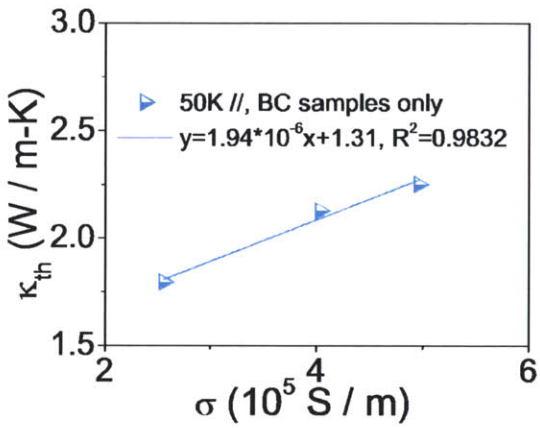

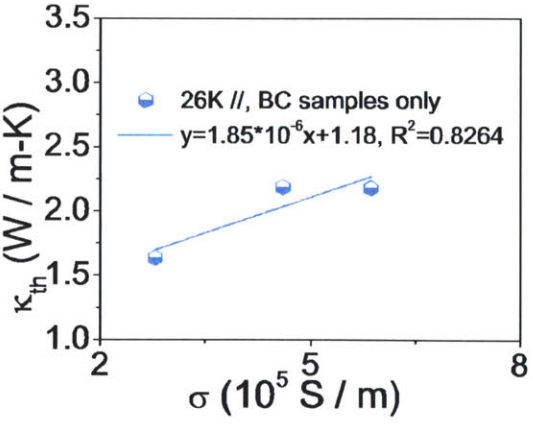

Figure 3-26: κ_{th} as a function of σ for all three BC nanocomposite samples investigated (*without the NTU nanocomposite samples*) in the // direction at a few interpolated temperatures (297K, 201K, 101K, 50K, and 26K). Linear fits of the data at the interpolated temperatures are also shown. The y-intercept (when σ=0) of the linear fit is considered the κ_L value. As the plots show, κ_{th} vs. σ produce an excellent linear fit relationship ($R^2 > 0.95$ for four out of the five plots) when using data from only the BC nanocomposite samples.

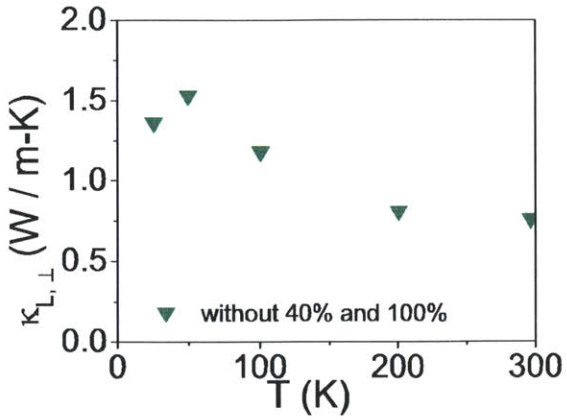

Figure 3-27: Plot of the $\kappa_{L,\perp}$ of nanocomposite samples fabricated using ball-milled nanoparticles as a function of temperature.

3.6 Conclusion

In this chapter, I have shown the results for all nanocomposite samples along with the Ingot sample. Many similarities exist between the samples investigated (see Tables 3.3 and 3.4). The similarities are easily noticed in the carrier concentration plot and the S plot (see Figures 3-9 and 3-8). Moreover, anisotropic behavior in κ_{th} and in ρ are observed in all nanocomposite samples investigated. We also learn that nanocomposite approach decreases μ_p, ℓ_e, and ℓ_{ph}. We conclude that all the samples investigated can be regarded as one materials system in the $\perp$ direction, but not in the // direction. Under this assumption, $\kappa_{\mathrm{L},\perp}$ is found to be 0.76W/m-K at 297K (see Table 3.6). This confirms that using the nanocomposite approach can further reduce the previously reported $(Bi_{0.3}Sb_{0.7})_2Te_3$ alloys κ_L(300K) value of 0.9W/m-K [4].

THIS PAGE INTENTIONALLY LEFT BLANK

Chapter 4

Interpretation of the $(Bi_ySb_{1-y})_2Te_3$ Measurement Results

A semi-classical model is applied in this chapter to further interpret the zero applied magnetic field results in Chapter 3. Section 4.1 gives a brief summary of my electron and phonon models based on semi-classical model. It follows with the numerous scattering mechanisms considered for both the electrons in Section 4.2.1 and the phonons in Section 4.2.2. Simple approximation on S and ρ for $T < 20$K and $200\text{K} < T < 300$K are given in Section 4.3. The fitting approach and the model interpretations of the measurements results are then presented in Sections 4.4 and 4.5, respectively. This chapter concludes with a summary of the findings from the electron and phonon models.

4.1 Semi-Classical Transport Model

We recall from Chapter 1 that the thermoelectric performance of a materials system depends on its dimensionless thermoelectric figure of merit (ZT)

$$ZT = S^2\sigma T/(\kappa_e + \kappa_L) = S^2T/[\rho(\kappa_e + \kappa_L)]. \tag{4.1}$$

According to Equation 4.1, ZT depends on the electrical conductivity (σ), the Seebeck coefficient (S), the electrical thermal conductivity (κ_e), the lattice thermal conductivity (κ_L), and the temperature (T). In Section 4.1.1, the treatment of the terms σ, S, and κ_e is considered one by one, while in Section 4.1.2, the treatment of κ_L is considered.

4.1.1 Electrons

There are two types of conduction carriers in semiconductors: holes and electrons. The model I use in this thesis is written with the assumption that electrons are the conduction carriers. Nevertheless, the model applies readily to the holes because holes are simply the opposite of electrons. The math is the same for both the holes and electrons as long as there is only one dominant conduction carriers in the materials system of interest. As we have seen in Chapter 3 (see Figures 3-8 and 3-9), all of our samples are p-type. Therefore, the electron model presented in this chapter can readily applied to our materials system, as long as we remember that the holes carry a positive charge instead of a negative charge.

The semi-classical model is used to interpret the various transport coefficients ($\sigma = 1/\rho$, S, and κ_e) and is based on the Boltzmann Transport Equation (BTE). The generalized BTE under the relaxation time approximation (RTA) [40]

$$\frac{\partial f}{\partial t} + \mathbf{v} \cdot \frac{\partial}{\partial \mathbf{r}} f + \mathbf{F} \cdot \frac{1}{\hbar} \frac{\partial}{\partial \mathbf{k}} f = -\frac{f(\mathbf{k}) - f^0(\mathbf{k})}{\tau_e(\mathbf{k})} \tag{4.2}$$

has a distribution function solution

$$f(t) = f^0(t) - \int_{-\infty}^{t} dt' P(t,t') \frac{d}{dt'} f^0(t'), \tag{4.3}$$

where $\mathbf{r}$ is the real space coordinates, $\mathbf{F}$ is an external force, $\mathbf{k}$ is the reciprocal space coordinates, and τ_e is the electron relaxation time. Equation 4.3 expresses the distribution function as the local equilibrium distribution $f^0(t)$ plus a correction term, in which $P(t,t')$ denotes the fraction of electrons that actually survive from time t'

to time t without suffering any further collisions. The BTE under the RTA has been studied for 1D, 2D, and 3D systems previously [41, 10, 11, 42]. For a simple one-band model in ζ dimensions, the carrier density (n), the electrical conductivity (σ), the Seebeck coefficient (S), and the electrical thermal conductivity (κ_e) are derived as [41, 10, 11]:

$$n = \int 2\frac{\overrightarrow{dk}}{(2\pi)^\zeta} f_e(E), \tag{4.4}$$

$$\sigma = \mathscr{L}_\zeta^{(0)}, \tag{4.5}$$

$$S = -\frac{1}{eT}\frac{\mathscr{L}_\zeta^{(1)}}{\mathscr{L}_\zeta^{(0)}}, \tag{4.6}$$

$$\kappa_e = \frac{1}{e^2T}(\mathscr{L}_\zeta^{(2)} - \frac{(\mathscr{L}_\zeta^{(1)})^2}{\mathscr{L}_\zeta^{(0)}}), \tag{4.7}$$

where T is the temperature in degrees Kelvin, and the integral function $\mathscr{L}_\zeta^{(\alpha')}$ is given by

$$\mathscr{L}_\zeta^{(\alpha')} = 2e^2 \int \frac{\overrightarrow{dk}}{(2\pi)^\zeta}\left(-\frac{\partial f_e}{\partial E}\right)\tau_e(E(k))v(k)v(k)(E(k)-E_f)^{\alpha'}, \tag{4.8}$$

where the factor of 2 accounts for the two electron spin states, ζ is the dimension of the system under consideration, $\alpha' = 0, 1, 2$, while $\overrightarrow{dk}$ is the differential element in ζ dimensional k space, $E(k)$ denotes the carrier dispersion relation, $\tau_e(E(k))$ is the electron relaxation time which in general depends on $E(k)$, E_f is the Fermi energy, and $f_e(E)$ is the Fermi-Dirac distribution function,

$$f_e(E) = \frac{1}{1+\exp^{(E-E_f)/(k_BT)}}. \tag{4.9}$$

The calculation of Equation (4.8) requires knowledge of the electron relaxation time $\tau_e(E(k))$ for the entire electron distribution. In general, $\tau_e(E(k))$ is a function of both temperature T and energy E. Moreover, different scattering mechanisms have different $\tau_e(E(k))$ terms. To consider the collective contribution of different scattering

mechanisms for practical situations, Matthiessen's rule [40]

$$\frac{1}{\tau_e} = \sum_i \frac{1}{\tau_{e,i}} \tag{4.10}$$

is used. In any actual materials system, there are many energy bands that need to be taken into consideration due to the near degeneracy of the multiple carrier pockets at the conduction band and valence band extrema. For a multi-band system, the n and $\mathscr{L}^{(\alpha')}$'s in Equations 4.4 to 4.7 needs to be replaced by the sum $n_{total} = \sum_b n_b$ and $\mathscr{L}^{(\alpha')}_{\zeta,total} = \sum_b \mathscr{L}^{(\alpha')}_{\zeta,b}$ for contributions from each subband b. The quantities n, σ, S, and κ_e then become

$$n_{total} = \sum_b n_b, \tag{4.11}$$

$$\sigma_{total} = \sum_b \mathscr{L}^{(0)}_{\zeta,b}, \tag{4.12}$$

$$S_{total} = -\frac{1}{eT}\frac{\sum_b \mathscr{L}^{(1)}_{\zeta,b}}{\sum_b \mathscr{L}^{(0)}_{\zeta,b}}, \tag{4.13}$$

$$\kappa_{e,total} = \frac{1}{e^2T}\left(\sum_b \mathscr{L}^{(2)}_{\zeta,b} - \frac{(\sum_b \mathscr{L}^{(1)}_{\zeta,b})^2}{\sum_b \mathscr{L}^{(0)}_{\zeta,b}}\right). \tag{4.14}$$

4.1.2 Phonons

Besides n, σ, S, and κ_e, the lattice thermal conductivity (κ_L) is another quantity of interest for thermoelectric applications. κ_L and κ_e together sum to yield the total thermal conductivity $\kappa_{\text{th}} = \kappa_e + \kappa_L$ of the system. Similar to the electron case, the phonon transport coefficient can also be derived using the BTE under the RTA with the following force $\mathbf{F}$ and distribution function f_{phonon}

$$\mathbf{F} = \nabla T, \tag{4.15}$$

$$f_{phonon} = \frac{1}{\exp^{\hbar\omega/(k_B T)} - 1}. \tag{4.16}$$

Using the Debye approximation, κ_L is derived as [43]

$$\kappa_L = \frac{k_B^4 T^3}{2\pi^2 v_s \hbar^3} \int_0^{\theta_D/T} \tau \frac{x^4 \exp^x}{(\exp^x - 1)^2} dx, \tag{4.17}$$

where θ_D is the Debye temperature, τ is the phonon relaxation time, v_s is the sound velocity, ω is the phonon angular frequency, and $x = \hbar\omega/(k_B T)$ is the dimensionless phonon energy.

4.2 Scattering Mechanisms

4.2.1 Electron Scattering Mechanisms

Six electron scattering mechanisms are considered in this thesis. They are (a) acoustic phonon scattering [44], (b) ionized impurity atom scattering [44, 45], (c) neutral impurity atom scattering [45, 46], (d) alloy scattering for a 3-atom system $I_p II_{1-p} III$ [47, 48], (e) point defect scattering [45], (f) grain boundary scattering [49], and (g) polar optical phonon scattering [50]. Using the above notations, each of the six scattering mechanism relaxation time has been derived previously as follows:

(a) $$\tau_{aph} = \frac{2\pi\hbar^4 \varrho v_s^2}{(pocket) D_A^2 (2m^* k_B T)^{3/2}} \sqrt{\frac{k_B T}{E}}, \tag{4.18}$$

where $m^{*3/2} = \sqrt{m_{t1} m_{t2} m_\ell}$,

(b) $$\tau_{ii} = \frac{(4\pi\varepsilon)^2 \sqrt{2m^*_{cond}} (k_B T)^{3/2}}{\pi e^4 N_i F_{imp}(E)} \left(\frac{E}{k_B T}\right)^{3/2}, \tag{4.19}$$

where $F_{imp}(E) = ln(1+\xi) - \frac{\xi}{1+\xi}$,

$$\xi = \frac{8 m^*_{cond} E r_0^2}{\hbar^2},$$

$$r_0 = \sqrt{\frac{\varepsilon\hbar^2\pi}{m^* e^2}} \left(\frac{\pi}{3n}\right)^{1/3},$$

(c) $$\tau_{ni} = \frac{m^{*2}_{cond} e^2}{80\hbar^3 \varepsilon N_0 \pi}, \tag{4.20}$$

$$\text{(d)} \qquad \tau_a = \frac{8N_A\hbar^4\sqrt{k_BT/E}}{(pocket)3\sqrt{2}\pi C_A(1-C_A)(\Delta E)^2(m^*)^{3/2}\sqrt{k_BT}}, \tag{4.21}$$

$$\text{(e)} \qquad \tau_{PD,e} = \frac{\pi\hbar^4}{m^*\sqrt{2m^*k_BT}U_0^2N_g}\sqrt{\frac{k_B}{T}}, \tag{4.22}$$

$$\text{(f)} \qquad \tau_{b,e} = \frac{\ell}{v_e^2}, \tag{4.23}$$

$$\text{where} \quad \frac{1}{2}m^*_{cond}v_e = \frac{3}{2}k_BT,$$

$$\text{(g)} \qquad \frac{1}{\tau_{PO}} = \frac{1}{\tau_0}\left(\frac{1}{\sqrt{\epsilon}} + \frac{\exp^z}{\sqrt{\epsilon - z}}\right), \tag{4.24}$$

$$\text{where} \quad \tau_0 = \frac{4\sqrt{2}\pi\varepsilon^2 M_{reduced}\delta^3(\hbar\omega_\ell)\sqrt{k_BT}}{(ee^*)^2\sqrt{m^*_{cond}}}\left(\exp^z - 1\right),$$

$$z = \frac{\hbar\omega_\ell}{k_BT},$$

$$\epsilon = \frac{E}{k_BT},$$

respectively. In Equations 4.18 to 4.24, E is the carrier energy, k_B is the Boltzmann constant, T is the temperature, $\hbar$ is Planck's constant divided by 2π, v_s is the sound velocity, ϱ is the mass density, *pocket* denotes the number of equivalent carrier pockets, D_A is the acoustic phonon deformation potential, m_{t1}, m_{t2}, and m_ℓ are the transverse and longitudinal effective mass components of an ellipsoidal model for each carrier pocket, ε is the permittivity, m^*_{cond} is the conduction effective mass, e is the charge of an electron, n is the carrier concentration of a particular carrier type, N_i is the ionized impurity atom concentration, N_0 is the neutral impurity atom concentration, ΔE is the effective bandgap offset between alloys I_0II_1III and I_1II_0III in a 3-atom system $I_pII_{1-p}III$ (Using $(Bi_{0.2}Sb_{0.8})_2Te_3$ as an example, I=Bi, II=Sb, III=Te, and p=0.2), N_A is the number of lattice points I in a 3-atom system $I_pII_{1-p}III$ unit cell, C_A is equal to p in a 3-atom system $I_pII_{1-p}III$, N_g is the point defect concentration, U_0 is the volume integral of the point defect potential, ℓ is the average diameter of the grain boundaries assuming that all grains have a spherical shape, v_e is the carrier velocity, $M_{reduced}$ is the reduced ion mass, δ^3 is the unit cell volume, ω_ℓ is the longitudinal optical phonon angular frequency, and e^* is the Callen effective charge.

Electron Parameters

For $(Bi_ySb_{1-y})_2Te_3$ under the rhombohedral unit cell system in reciprocal spaces, $\hat{x}$ is the binary axis, $\hat{y}$ is the bisectrix axis which is also in the hexagonal plane and normal to the binary axis, and $\hat{z}$ is the trigonal axis which is along the main symmetry c axis. The $\hat{y}$-$\hat{z}$ plane is a reflection plane, $\hat{z}$ is the 3-fold rotation axis, and $\hat{x}$ is the 2-fold rotation axis. For $(Bi_{0.2}Sb_{0.8})_2Te_3$, there are six degenerate hole pockets as mentioned in Chapter 3. For one of the hole pockets that lies in the $\hat{y} - \hat{z}$ plane (denoted as the 1st hole pocket), one of its major axes makes an angle of 47.9^o with the $\hat{y}$ axis. The masses of the hole pocket at 300K are found to be $m_{11} = 0.096m_0$, $m_{22} = 1.73m_0$, and $m_{33} = 0.170m_0$ [32]. The locations of the other five hole pockets can be found by using the following operations: (a) from the 1st hole pocket, rotate 120^o in the $\hat{x}$-$\hat{y}$ plane; (b) from the 1st hole pocket, rotate 240^o in the $\hat{x}$-$\hat{y}$ plane; (c) from the 1st hole pocket, rotate 180^o in the $\hat{x}$-$\hat{z}$ plane; (d) from the 1st hole pocket, rotate 180^o in the $\hat{x}$-$\hat{z}$ plane followed by rotating 120^o in the $\hat{x}$-$\hat{y}$ plane; and (e) from the 1st hole pocket, rotate 180^o in the $\hat{x}$-$\hat{z}$ plane followed by rotating 240^o in the $\hat{x}$-$\hat{y}$ plane.

For describing carrier conduction, the applied electric field is usually given in the lab coordinates instead of the crystal coordinates. Thus, one needs to transform between the crystal and the lab coordinates using the following unitary transformation

$$\sigma_{lab} = \overleftrightarrow{R}_{crystal \to lab}\, \sigma_{crystal}\, \overleftrightarrow{R}_{lab \to crystal} = \overleftrightarrow{R}_{lc}\, \sigma_{crystal}\, \overleftrightarrow{R}_{cl} \tag{4.25}$$

to perform the calculation consistently where $\overleftrightarrow{R}$ is a matrix that rotates the between the lab and crystal axes. For the σ calculation, this simply means that the masses need to be rotated to the proper axes before putting them into Equation 4.12 for calculation. For $(Bi_ySb_{1-y})_2Te_3$, the reciprocal masses in the crystal coordinates can be expressed as

$$\alpha = \begin{pmatrix} 1/m_{t1} & & \\ & 1/m_{t2} & \\ & & 1/m_{\ell} \end{pmatrix}, \tag{4.26}$$

where m_{t1}, m_{t2}, and m_{ℓ} are the mass components along the carrier pocket's ellipsoidal

major axes. After representing the reciprocal masses using the lab axes, the sum of α for all six pockets would be

$$\sum_{crystal \to lab} \overleftrightarrow{R}_{crystal \to lab} \, \alpha \, \overleftrightarrow{R}_{crystal \to lab,inv} = \frac{1}{m_0} \begin{pmatrix} 40.1365 & 0 & 0 \\ 0 & 40.1365 & 0 \\ 0 & 0 & 20.9893 \end{pmatrix}. \tag{4.27}$$

As we can see from Equation 4.27, the conduction mass m^*_{cond} would be $m_0/20.9893$ for transport in the trigonal direction. Since nanocomposite samples are composed of random particles in various orientations, the conduction mass m^*_{cond} should be isotropic and would be approximated by the average of the masses in all directions. Thus,

$$\frac{1}{m^*_{cond,nanocomposite}} = \left(\frac{1}{m_{t1}} + \frac{1}{m_{t2}} + \frac{1}{m_\ell} \right) /3 \tag{4.28}$$

and $m^*_{cond,nanocomposite} = m_0/33.75$ at 300K. From Equation 4.9, we see that the electron distribution function is highly temperature-dependent. Since we expect the energy bands to be parabolic only near the band edge, the mass then should be a temperature-dependent parameter. Using the S data from Figure 3-8, we find that the temperature-dependent form $m^* \propto T^{0.12} \rightarrow m^*(0K) \approx 0.6\ m^*(300K)$ works well with our data (see Section 4.3).

To obtain the rest of the $(Bi_{0.2}Sb_{0.8})_2Te_3$ parameters needed for Equations 4.18 to 4.24, I use a linear interpolation between values of Bi_2Te_3 and Sb_2Te_3. Table 4.1 lists all the parameters used in my electron model.

4.2.2 Phonon Scattering Mechanisms

The phonon scattering mechanisms considered in this thesis are (a) boundary scattering, (b) point defect / alloy scattering, and (c) Umklapp scattering. The point defect scattering and alloy scattering processes are lumped together because they both possess the same temperature and energy dependences. On the other hand, the phonon-phonon normal scattering mechanism is not considered because nanocomposite samples are far from the ideal defect-free pure crystal sample required for the

Table 4.1: Parameters for the electron model. A linear interpolation between values of Bi_2Te_3 and Sb_2Te_3 is used to obtain the values for $(Bi_{0.2}Sb_{0.8})_2Te_3$.

Parameter	*Bi_2Te_3*	*Sb_2Te_3*	*$(Bi_{0.2}Sb_{0.8})_2Te_3$*
energy gap (meV)	140 [27, 28]	290 [27, 28]	260
mass density ϱ (g/cm^3)	7.86 [51]	6.505 [51]	6.776
permittivity $\varepsilon \perp$ c	$290\varepsilon_0$ [52]	$168\varepsilon_0$ [51]	$192.4\varepsilon_0$
permittivity ε // c	$75\varepsilon_0$ [52]	$36.5\varepsilon_0$ [51]	$44.2\varepsilon_0$
permittivity ε average			$118.3\varepsilon_0$
N_A (cm^{-3})			2.48x10^{21}
C_A			0.2
$M_{reduced}$ (kg)			2.68x10^{-25}
m_0 (kg)			9.11x10^{-31}
unit cell volume δ^3 (m^3)			1.61x10^{-28}
ω_ℓ (THz)			2πx2.0267 [52]

normal scattering mechanism to play a major role.

Boundary scattering τ_b [53], point defect / alloy scattering τ_{PD} [54, 55, 56, 57, 58, 59, 60], and Umklapp scattering τ_U [61, 62] relaxation times have been derived previously as

$$\frac{1}{\tau_b} = \frac{v_s}{\ell}, \tag{4.29}$$

$$\frac{1}{\tau_{PD}} = A' \frac{\delta^3 \Gamma' (k_B T)^4}{4\pi v_s^3 \hbar^4} x^4, \tag{4.30}$$

$$\frac{1}{\tau_U} = B' \left(\frac{k_B}{\hbar}\right)^2 x^2 T^3 e^{-C\theta_D/T}, \tag{4.31}$$

respectively, where v_s is the sound velocity, ℓ is the average diameter of the grain boundaries assuming all grains have a spherical shape, δ^3 is the unit cell volume, θ_D is the Debye temperature, Γ' is the scattering parameter, and A', B', and C are the fitting parameters. For a 3-atom system $I_q II_r III_s$, the scattering parameter Γ' is as

Table 4.2: Parameters for the $(Bi_{0.2}Sb_{0.8})_2Te_3$ phonon model obtained based on the values of Bi_2Te_3 and Sb_2Te_3 using an appropriate stoichiometric weighting factor.

Parameter	*Bi_2Te_3*	*Sb_2Te_3*	*$(Bi_{0.2}Sb_{0.8})_2Te_3$*
Debye temperature θ_D	165K at 0K [63]	160K at 80K [51]	165K
sound velocity v_s (m/s)	$2.95\text{x}10^3$ [63]	$2.90\text{x}10^3$ [64]	$2.95\text{x}10^3$
unit cell volume δ^3 (m^3)	$1.69\text{x}10^{-28}$ [51]	$1.60\text{x}10^{-28}$ [51]	$1.61\text{x}10^{-28}$
M for alloy scattering (g/mol)	160.15	125.26	132.24
Γ'	N/A	N/A	0.0297

follows

$$\begin{aligned} 1 &= q + r + s, \\ M &= qM_I + rM_{II} + sM_{III}, \\ \Gamma' &= q(1 - \frac{M_I}{M})^2 + r(1 - \frac{M_{II}}{M})^2 + s(1 - \frac{M_{III}}{M})^2. \end{aligned} \tag{4.32}$$

Similar to the electron case, Matthiessen's rule

$$\frac{1}{\tau} = \sum_i \frac{1}{\tau_i} \tag{4.33}$$

is used to sum the contribution of different phonon scattering mechanisms. Lastly, a linear interpolation is applied to obtain the $(Bi_{0.2}Sb_{0.8})_2Te_3$ parameters needed for Equations 4.29 to 4.31 based on the values of Bi_2Te_3 and Sb_2Te_3. Table 4.2 lists all the parameters used in my phonon model.

4.3 S and ρ approximation for $T < 20$K and for $200\text{K} < T < 300\text{K}$

Instead of going directly into solving the BTE under the RTA with all the complicated relaxation times that we obtained in Section 4.2.1, let us make a few approximations

to get a better sense of the transport coefficients. Assuming the materials system of interest has only one spherical carrier pocket and has one dominant scattering mechanism, Equation 4.8 in 3D becomes

$$\mathscr{L}^{(0)} = \frac{8\pi e^2}{3m^*_{cond}h^3}(2m^*k_BT)^{3/2}\int_{E_0/(k_BT)}^{\infty}\frac{\tau_e(\epsilon-\frac{E_0}{k_BT})^{3/2}\exp^{\epsilon-\eta^*}}{[\exp^{\epsilon-\eta^*}+1]^2}d\epsilon, \tag{4.34}$$

$$\mathscr{L}^{(1)} = \frac{8\pi e^2 k_BT}{3m^*_{cond}h^3}(2m^*k_BT)^{3/2}\int_{E_0/(k_BT)}^{\infty}\frac{\tau_e(\epsilon-\frac{E_0}{k_BT})^{3/2}\exp^{\epsilon-\eta^*}}{[\exp^{\epsilon-\eta^*}+1]^2}(\epsilon-\eta^*)d\epsilon, \tag{4.35}$$

$$\mathscr{L}^{(2)} = \frac{8\pi e^2 (k_BT)^2}{3m^*_{cond}h^3}(2m^*k_BT)^{3/2}\int_{E_0/(k_BT)}^{\infty}\frac{\tau_e(\epsilon-\frac{E_0}{k_BT})^{3/2}\exp^{\epsilon-\eta^*}}{[\exp^{\epsilon-\eta^*}+1]^2}(\epsilon-\eta^*)^2d\epsilon, \tag{4.36}$$

where

$$\epsilon = E/(k_BT), \tag{4.37}$$

$$\eta^* = E_f/(k_BT), \tag{4.38}$$

and E_0 is the band edge energy. From Equations 4.18 to 4.24, the electron relaxation time τ_e can be generalized as

$$\tau_e = aE^{\lambda}(k_BT)^{\beta} \tag{4.39}$$

by considering the dependence of τ on T and E explicitly. Combining Equations 4.34 and 4.35 with 4.39, and applying the uv substitution formula to the integrals give

$$\mathscr{L}^{(0)} \propto (k_BT)^{\frac{3}{2}+\lambda}(\frac{3}{2}+\lambda)\int_0^{\infty}\frac{\epsilon^{\frac{1}{2}+\lambda}}{\exp^{\epsilon-\eta^*}+1}d\epsilon, \tag{4.40}$$

$$\mathscr{L}^{(1)} \propto \left[\left((k_BT)^{\frac{5}{2}+\lambda}(\frac{5}{2}+\lambda)\int_0^{\infty}\frac{\epsilon^{\frac{3}{2}+\lambda}}{\exp^{\epsilon-\eta^*}+1}d\epsilon\right)-\left(k_BT\eta^*\mathscr{L}^{(0)}\right)\right]. \tag{4.41}$$

We quickly see that the transport coefficient calculation for σ and S now boils down to simply the computation of the integrals in Equations 4.40 and 4.41. Remember that the only assumptions made so far are: (a) there is only one spherical carrier pocket for the materials system of interest and (b) there is only one dominant electron scattering

mechanism. Using Sommerfeld's definition for the Fermi-Dirac integral of order j [65]

$$F_j(\eta^*) \triangleq \int_0^\infty \frac{\epsilon^j}{\exp^{\epsilon-\eta^*}+1} d\epsilon \quad (j > -1), \tag{4.42}$$

the result for the high temperature limiting case ($\eta^* \ll -1$) is [66]

$$F_j(\eta^*) \approx \Gamma(j+1)\exp^{\eta^*} \quad (\eta^* \ll -1), \tag{4.43}$$

where $\Gamma(1/2) = \sqrt{\pi}, \Gamma(3/2) = \sqrt{\pi}/2$, and $\Gamma(p+1) = p\Gamma(p)$. Similarly, the result for the low temperature limiting case ($\eta^* \gg 1$) is [66]

$$F_j(\eta^*) \approx \frac{\eta^{*j+1}}{j+1}\left(1 + \frac{\pi^2 j(j+1)}{6\eta^{*2}}\right) \quad (\eta^* \gg 1). \tag{4.44}$$

Since experimental data are readily available for S and σ, let us look at what approximations we can make for the low temperature and high temperature limits for these quantities. Without any approximations, combining Equations 4.40, 4.41, and 4.6 give

$$S = \frac{k_B}{e}\left[\frac{\lambda + \frac{5}{2}}{\lambda + \frac{3}{2}}\frac{F_{\lambda+\frac{3}{2}}(\eta^*)}{F_{\lambda+\frac{1}{2}}(\eta^*)} - \eta^*\right]. \tag{4.45}$$

We now proceed to give the dependence of S and ρ at both the low and high temperature limits.

4.3.1 Seebeck S

At low temperature ($\eta^* \gg 1$), using Equation 4.44, S and n can be approximated to be

$$S \approx \frac{k_B \pi^2 (\lambda + \frac{3}{2})}{3e\eta^*}, \tag{4.46}$$

$$n \approx (pocket)\frac{8}{3\sqrt{\pi}}\left(\frac{2\pi m^* k_B T}{h^2}\right)^{3/2} \eta^{*3/2}. \tag{4.47}$$

As a result, S can be rewritten as

$$S \approx \left[\frac{k_B\pi^2(\lambda+\frac{3}{2})}{3e}\frac{2m^*k_B}{h^2}\left(\frac{(pocket)4\pi}{\frac{3}{2}n}\right)^{2/3}\right]T \quad (\eta^* \gg 1), \tag{4.48}$$

Similarly, at high temperature ($\eta^* \ll -1$), assuming that only one carrier type dominates and using Equation 4.43, S and n can be approximated to be

$$S \approx \frac{k_B}{e}(\lambda+\frac{5}{2}-\eta^*), \tag{4.49}$$

$$n \approx (pocket)2\left(\frac{2\pi m^*k_BT}{h^2}\right)^{3/2}. \tag{4.50}$$

As a result, S can be rewritten as

$$\begin{aligned} S &\approx \frac{k_B}{e}\left(\lambda+\frac{5}{2}+ln(\frac{1}{n})+ln\left[\frac{(pocket)2(2\pi k_B)^{3/2}}{h^3}\right]\right)+\frac{3k_B}{2e}ln(m^*)+\frac{3k_B}{2e}ln(T) \\ &= S_{0,high}+\frac{3k_B}{2e}ln(m^*)+\frac{3k_B}{2e}ln(T) \quad (\eta^* \ll -1), \end{aligned} \tag{4.51}$$

where $S_{0,high}$ is a constant independent of T.

From Equations 4.48 and 4.51, we see that $S \propto T$ at low temperature ($\eta^* \gg 1$) and $S \propto ln(T)$ at high temperature ($\eta^* \ll -1$). Moreover, the only variables in S are λ and the carrier concentration n. We notice that a higher n results in a lower slope value in S vs. T in the low temperature limit, but not in the S vs. $ln(T)$ slope in the high T limit. Furthermore, from Table 3.4, we also notice that the slope in S vs. $ln(T)$ for 200K $< T <$ 300K is $\sim 140\mu V/K > \frac{3k_B}{2e} = 129\mu V/K$. From Equation 4.51, we see that m^* is the only parameter that can change the value of the slope $\partial S/\partial ln(T)$ given n is temperature independent. As a result, we assume $m^* \propto T^{0.12}$ and obtain a slope of $144\mu V/K$, which is much closer to the measured values in the 200K to 300K range. Lastly, the results of Equations 4.48 and 4.51 confirm the isotropic nature of S. These relationships can be readily verified using Figure 3-8.

4.3.2 Resistivity ρ

At low temperature ($\eta^* \gg 1$), using Equations 4.12, 4.39, and 4.44, σ can be approximated to be

$$\sigma \approx \frac{a8\pi e^2}{3m^* h^3}(2m^*)^{3/2}(k_B T)^{\frac{3}{2}+\lambda+\beta}(\eta^*)^{\lambda+\frac{3}{2}}. \tag{4.52}$$

As a result, ρ can be rewritten as

$$\rho = \sigma^{-1} \approx \left(\frac{ae^2 n}{m^*(pocket)} \left[\left(\frac{3n}{(pocket)8\pi} \right)^{2/3} \frac{h^2}{2m^*} \right]^{\lambda} (k_B T)^{\beta} \right)^{-1} \quad (\eta^* \gg 1). \tag{4.53}$$

Similarly, at high temperature ($\eta^* \ll -1$), using Equations 4.12, 4.39, and 4.43, ρ can be approximated to be

$$\rho = \sigma^{-1} \approx \left(\frac{a8\pi e^2}{3m^* h^3}(2m^*)^{3/2}(k_B T)^{\frac{3}{2}+\lambda+\beta}(\lambda+\frac{3}{2})\Gamma(\lambda+\frac{3}{2})\exp^{\eta^*} \right)^{-1}. \tag{4.54}$$

As a result, ρ can be rewritten as

$$\rho = \frac{3m^*\sqrt{\pi}(pocket)}{a4e^2 n(\lambda+\frac{3}{2})\Gamma(\lambda+\frac{3}{2})(k_B)^{\lambda+\beta}} \frac{1}{T^{\lambda+\beta}} \quad (\eta^* \ll -1). \tag{4.55}$$

From Equations 4.53 and 4.55, we see that $\rho \propto T^{-\beta}$ at low temperature ($\eta^* \gg 1$) and $\rho \propto T^{-\lambda-\beta}$ at high temperature ($\eta^* \ll -1$). Once again, the only variables in ρ are λ and the carrier concentration n. We also notice that a higher n results in a lower value in ρ as expected. This relationship can be readily verified using any of the ρ figures in Chapter 3.

One can satisfactorily use Equations 4.53 and 4.55 to get a sense of the dominant scattering mechanism in the low temperature limit and in the high temperature limit, respectively. At low temperature, using Figure 3-9 and Table 3.3, we see that both the carrier concentration and ρ are relatively constant for $T < 20$K. Thus, the low temperature dominant scattering mechanism should have a β value of zero. Assuming that m^* is a function of T in this temperature range, then $\lambda < 0$, which means the only possible scattering mechanisms for our samples are (a) point defect scattering and

(b) alloy scattering. On the other hand, in the high temperature range, all samples have a functional form of ρ that is proportional to $\sim T^{3/2}$. As a result, we conclude that the dominant scattering mechanism for our samples in this temperature range is acoustic phonon scattering.

4.4 Fitting approaches

Since there are more than one fitting parameter and the fitting functions are rather complicated, a simple linear least square fitting technique is not appropriate. Therefore, a non-linear least square fitting approach is used for all data fitting in this thesis. In particular, the Levenberg-Marquardt Algorithm [67, 68] is used for all parameter fitting in this thesis.

To obtain a better understanding of our samples, we fit our data using the equations described in Sections 4.1, 4.2.1, and 4.2.2. For the electron modeling, the Fermi level is first calculated using Equation 4.11 and the carrier concentration data from Figure 3-9. The τ_e values from Equations 4.18 to 4.24 are then added together using Equation 4.10 before substituting them into Equations 4.34 to 4.36 to fit our S and ρ data using the adjustable parameters D_A, N_i, N_0, ΔE, ℓ, and e^*. Once a satisfactory fit is obtained, κ_L is calculated using both the κ_{th} data and the κ_e calculated from the electron model. For the phonon model, the τ values from Equations 4.29 to 4.31 are first summed together using Equation 4.33. The sum is then substituted into Equations 4.17 and κ_L is fitted using adjustable parameters ℓ, A', B', and C. Once a satisfactory fit is obtained, the ℓ obtained is compared with the ℓ value from the electron model. If the difference is not within 1%, then the fitting cycle continues until the ℓ difference reaches below 1%.

4.5 Fitting Results

Figures 4-1 to 4-4 together with Figures F-1 to F-10 show my electron model fitting results for all samples investigated based on my electron model (see Sections 4.1.1

and 4.2.1). κ_e based on my model is plotted as a function of temperature against (a) κ_{th} - κ_{th}(9T), (b) $\mathcal{L}\sigma T$ with $\mathcal{L}$=2x10^{-8}W-Ohm/K^2, and (c) $\mathcal{L}\sigma T$ with $\mathcal{L}$=3x10^{-8}W-Ohm/K^2. For the electron model fitting, it is found that the dominant scattering mechanisms are acoustic phonon scattering, point defect / ionized impurity atom scattering, and neutral impurity atom scattering. As a result, all the fitting results for ρ of each sample are plotted with the relative contribution from acoustic phonon scattering, point defect / ionized impurity atom scattering, and neutral impurity atom scattering. However, alloy scattering, grain boundary scattering, and polar optical phonon scattering are also considered in my electron model. The fitting results confirm the theory mentioned in Section 4.3 that the acoustic phonon scattering mechanism dominates for $T > 200$K, and that the point defect scattering mechanism dominates for $T < 20$K. Moreover, the crossover temperature T_{cross} between these two scattering mechanisms increases from bulk to nanocomposite samples. In general, T_{cross} increases as ℓ decreases (see Figure 4-5. From κ_e, the calculations indicate that $\mathcal{L}$ decreases as T increases. More on $\mathcal{L}$ will be discussed later.

Using κ_{th} and the calculated κ_e, κ_L is computed and fitted using my phonon model (see Sections 4.1.2 and 4.2.2). Figures 4-6 to 4-9 together with G-1 to G-10 show the fitting results of my phonon model for all samples investigated. For my phonon model fitting results, it is found that the boundary scattering, point defect scattering, and Umklapp scattering mechanisms play an important role in the determination of κ_L. To get a better picture of the breakdown of the relative importance of the various scattering mechanisms for the different temperature ranges, the boundary scattering together with the point defect scattering mechanisms (denoted by Boundary & PD), as well as the Umklapp scattering together with the point defect scattering mechanisms (denoted by Umklapp & PD), are plotted along with the κ_L as a function of temperature. From my phonon model, we observe that as the boundary scattering mechanism increases its relative contribution, the peak value for κ_L decreases. As a result, the crossover temperature between [Boundary & PD] and [Umklapp & PD] increases from the sample Ingot // to the nanocomposite samples. We also notice that this crossover temperature is approximately equal to the T_{cross} from the elec-

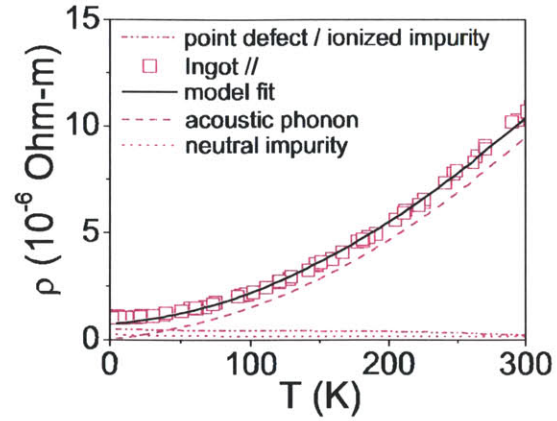

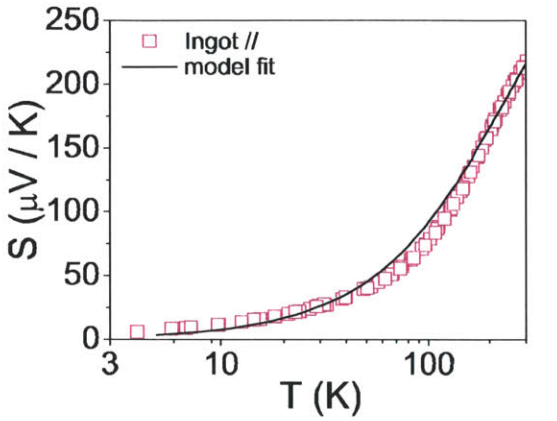

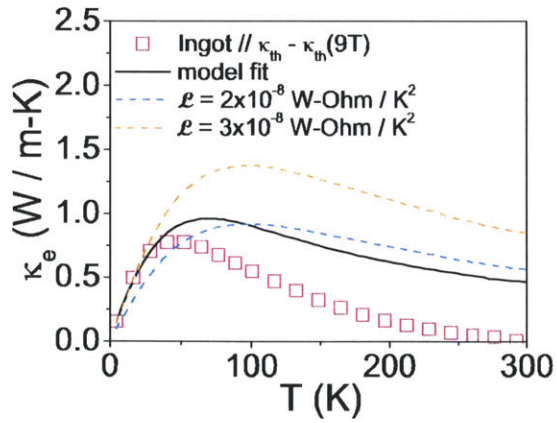

Figure 4-1: Fitting results of sample Ingot // based on the electron model. The contribution to ρ from acoustic phonon scattering, point defect / ionized impurity atom scattering, and neutral impurity atom scattering are plotted as well. The fitting results confirm that the acoustic phonon scattering mechanism dominates for $T > 200$K and that the point defect scattering mechanism dominates for $T < 20$K. From κ_e, $\mathcal{L}$ is calculated to decrease as T increases.

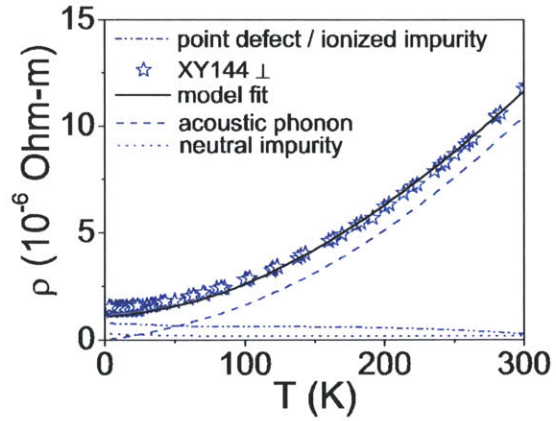

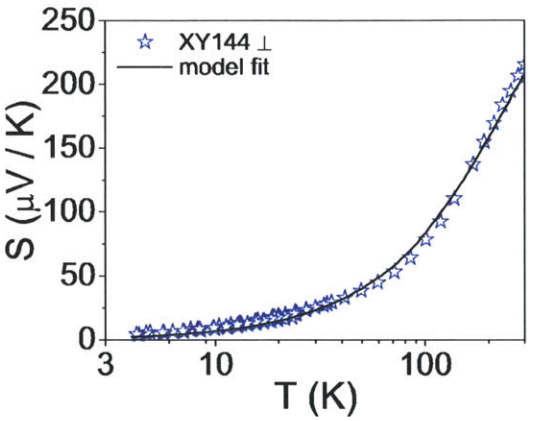

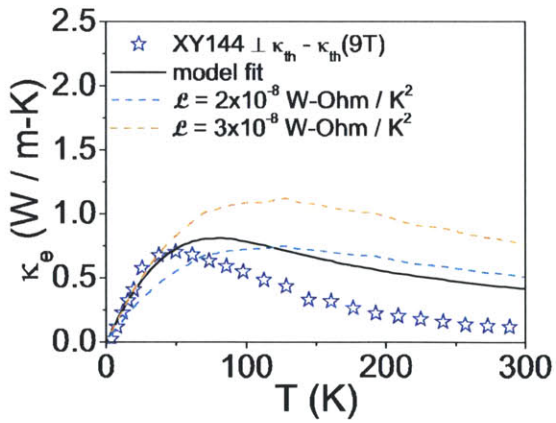

Figure 4-2: Fitting results of sample XY144 $\perp$ based on the electron model. The contribution to ρ from acoustic phonon scattering, point defect / ionized impurity atom scattering, and neutral impurity atom scattering are plotted as well. The fitting results confirm that the acoustic phonon scattering mechanism dominates for $T > 200$K and that the point defect scattering mechanism dominates for $T < 20$K. From κ_e, $\mathcal{L}$ is calculated to decrease as T increases.

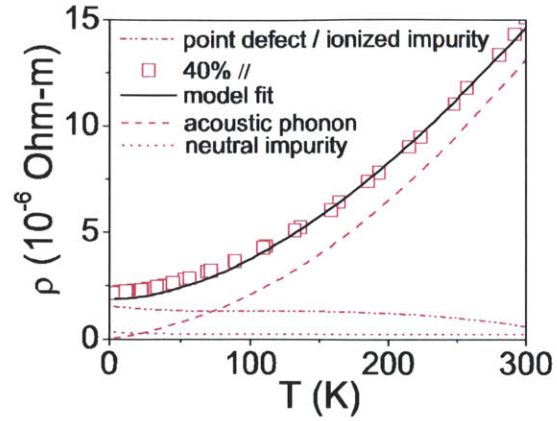

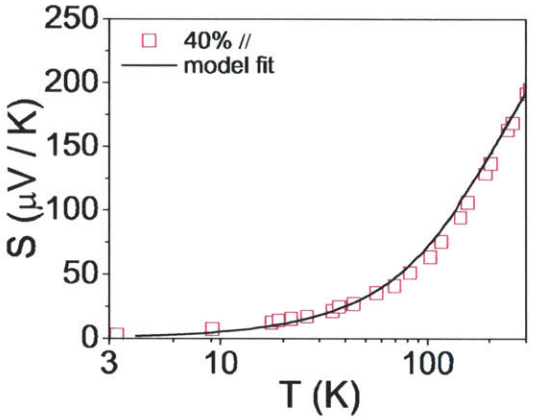

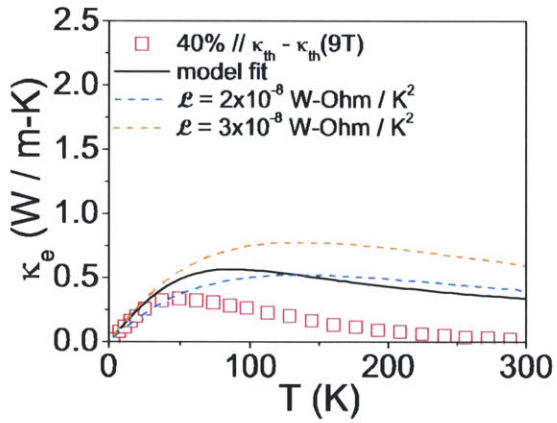

Figure 4-3: Fitting results of sample 40% // based on the electron model. The contribution to ρ from acoustic phonon scattering, point defect / ionized impurity atom scattering, and neutral impurity atom scattering are plotted as well. The fitting results confirm that the acoustic phonon scattering mechanism dominates for $T > 200$K and that the point defect scattering mechanism dominates for $T < 20$K. From κ_e, $\mathcal{L}$ is calculated to decrease as T increases.

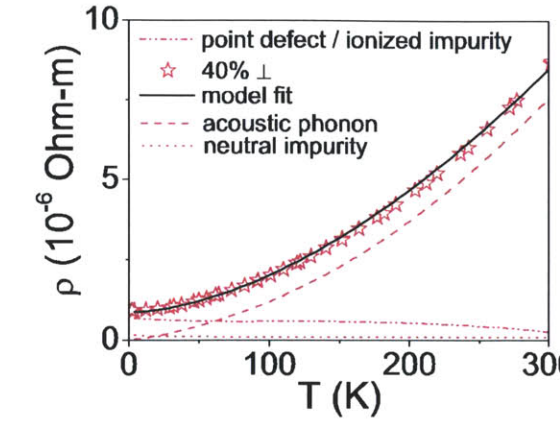

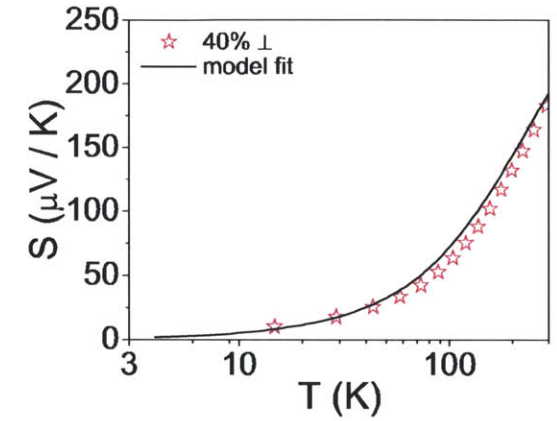

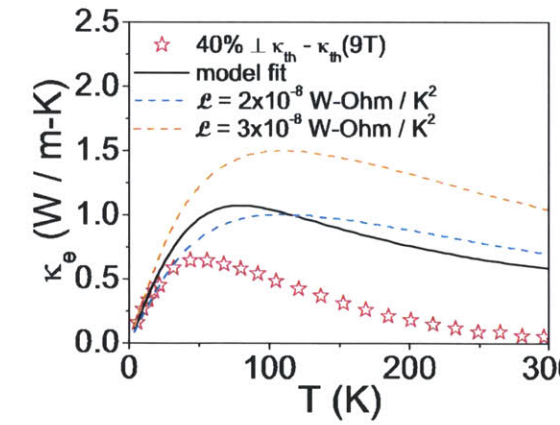

Figure 4-4: Fitting results of sample 40% ⊥ based on the electron model. The contribution to ρ from acoustic phonon scattering, point defect / ionized impurity atom scattering, and neutral impurity atom scattering are plotted as well. The fitting results confirm that the acoustic phonon scattering mechanism dominates for $T > 200$K and that the point defect scattering mechanism dominates for $T < 20$K. From κ_e, $\mathcal{L}$ is calculated to decrease as T increases.

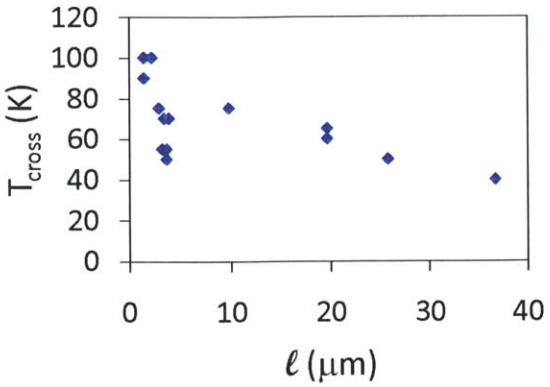

Figure 4-5: Plot of T_{cross} of all samples investigated as a function of ℓ.

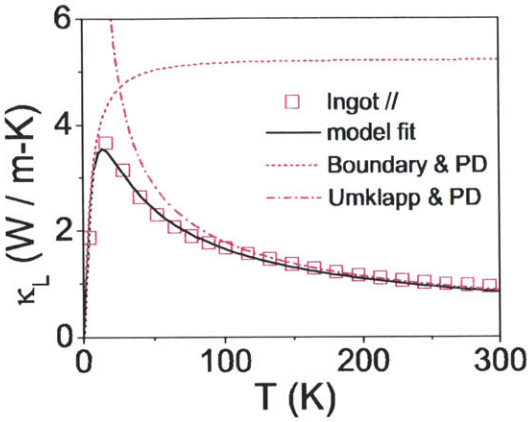

Figure 4-6: Fitting results of sample Ingot // based on the phonon model. The boundary scattering together with the point defect scattering mechanisms (Boundary & PD), as well as the Umklapp scattering together with the point defect scattering mechanisms (Umklapp & PD), are plotted along with κ_L.

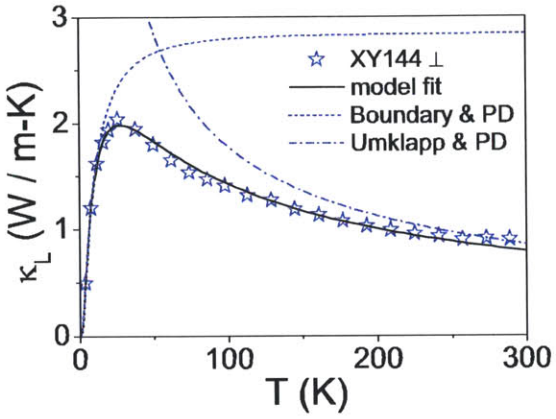

Figure 4-7: Fitting results of sample XY144 ⊥ based on the phonon model. The boundary scattering together with the point defect scattering mechanisms (Boundary & PD), as well as the Umklapp scattering together with the point defect scattering mechanisms (Umklapp & PD), are plotted along with κ_L.

tron model. Tables 4.3 and 4.4 summarize the electron and phonon fitting results, respectively.

For the electron model, from Table 4.3 we observe that the deformation potential D_A seems to be both process dependent and materials dependent. We see that D_A changes from the BC samples to the NTU samples (process dependent). Moreover, D_A changes in the NTU samples when going from 0% to 100% (materials dependent). From the electron model, the ionized impurity atom concentration N_i and the neutral impurity atom concentration N_0 reflect the somewhat anisotropic behavior of all the

Table 4.3: Electron model fitting results. Please refer to Section 4.2.1 for the detailed explanation for each parameter. For a quick summary, D_A denotes the deformation potential in the acoustic phonon scattering mechanism, N_i denotes the point defect / ionized impurity atom concentration in the point defect / ionized impurity atom scattering mechanisms, e^* denotes the Callen effective charge in the optical phonon scattering mechanism, N_0 denotes the neutral impurity atom concentration in the neutral impurity atom scattering mechanism, ΔE denotes the difference in the bandgap in the alloy scattering mechanism, and ℓ denotes the average diameter of the grain boundaries assuming all grains have a spherical shape.

Sample	D_A *(eV)*	N_i *(10^{19} cm^{-3})*	e^* *(e)*	N_0 *(10^{13} cm^{-3})*	ΔE *(eV)*	ℓ *(μm)*	T_{cross} *(K)*
Ingot //	5	2.35		3		36.78	40
XY21 //	5.2	6.5		8		1.47	100
XY21 $\perp$	4.9	5		6		1.47	90
XY146 //	5.4	3.3		6		3.28	55
XY146 $\perp$	5.3	3.3		6		3.69	55
XY144 $\perp$	5.1	3.0	0.1	5.0	0.012	3.69	50
GJ99 //	5.4	7		9.1		3.47	70
GJ99 $\perp$	5	6		7		3.93	70
0% //	5.8	6		5		19.64	60
0% $\perp$	4.6	3.5		3		25.80	50
40% //	6.25	9		8		9.83	75
40% $\perp$	4.75	4		3.5		19.64	65
100% //	6.25	15		12.5		2.27	100
100% $\perp$	5.2	7.0		6.0		2.95	75

Table 4.4: Phonon model fitting results. Please refer to Section 4.2.2 for the detailed explanation for each parameter. For a quick summary, ℓ denotes the average diameter of the grain boundaries assuming all grains have a spherical shape, A' denotes the coefficient of the point defect scattering mechanism, B' denotes the coefficient of the Umklapp scattering mechanism, and C denotes the coefficient of the exponent in the Umklapp scattering mechanism.

Sample	$\ell(\mu m)$	A'	$B'(10^{-18}s/K)$	C
Ingot //	36.78	2.73	9.65	0.13
XY21 //	1.47	2.89	9.84	
XY21 $\perp$	1.47	2.65	9.83	
XY146 //	3.28	2.76	12.16	
XY146 $\perp$	3.69	2.51	10.99	
XY144 $\perp$	3.69	2.69	9.88	
GJ99 //	3.47	3.17	10.81	
GJ99 $\perp$	3.93	2.63	9.35	
0% //	19.64	6.17	9.35	
0% $\perp$	25.80	2.90	9.35	
40% //	9.83	8.24	6.53	
40% $\perp$	19.64	5.19	4.38	
100% //	2.27	5.92	4.43	
100% $\perp$	2.95	4.19	4.43	

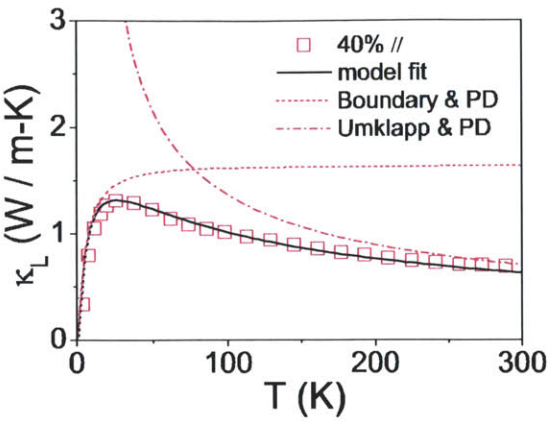

Figure 4-8: Fitting results of sample 40% // based on the phonon model. The boundary scattering together with the point defect scattering mechanisms (Boundary & PD), as well as the Umklapp scattering together with the point defect scattering mechanisms (Umklapp & PD), are plotted along with κ_L.

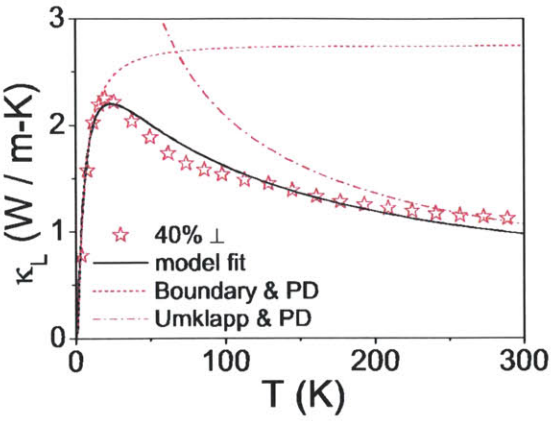

Figure 4-9: Fitting results of sample 40% ⊥ based on the phonon model. The boundary scattering together with the point defect scattering mechanisms (Boundary & PD), as well as the Umklapp scattering together with the point defect scattering mechanisms (Umklapp & PD), are plotted along with κ_L.

samples investigated. Lastly, ℓ seems to play only a small role in the determination of ρ.

For the phonon model, from Table 4.4 we observe that ℓ plays a rather important role in the determination of κ_L, especially at low temperatures. The value of ℓ seems to be consistently lower for the BC samples than for the NTU sample (0 %) for the nanocomposite samples made solely from ball-milled nanoparticles. It could be interesting to see what kind of ℓ values would result by combining the starting materials from NTU and the fabrication procedures from BC. We also see that the Umklapp scattering contribution (B') has a materials dependent factor, where B' decreases from $\approx$10x10^{-18}s/K for the nanoparticles nanocomposite samples to $\approx$4x10^{-18}s/K for the nanocomposite sample made using 100% nanoinclusions prepared via melt spinning. Furthermore, we see that the point defect contribution (A') reaches the highest value when both the nanoparticles and nanoinclusions prepared via melt spinning are present in the nanocomposite samples (e.g. the 40% sample), similar to the alloying effect on the thermal conductivity.

As we will show in Chapter 5, κ_{th} reaches a plateau for the samples investigated

under an applied magnetic field of 9T at low temperatures ($T < 26$K). This implies that the applied B field has truly pushed the electrons aside and $\kappa_{th} \rightarrow \kappa_L$. Thus, we expect that κ_e from my electron model should be approximately equal to the values of κ_{th} - κ_{th}(9T) in the low temperature regime where magnetic field saturation occurs. As Figures 4-1 to 4-4 and F-1 to F-10 show, my κ_e results meet this expectation. To further demonstrate this point, and to get a better sense of the breakdown between the electronic and lattice contribution to the thermal conductivity, the calculated κ_L and calculated κ_e are plotted against κ_{th} (and κ_{th}(9T) when such data are available) (see Figures 4-10 to 4-13 and H-1 to H-10). From these figures, the Lorenz Number $\mathcal{L}$ can be extracted. Figure 4-14 shows the $\mathcal{L}$ values as a function of temperature for all samples investigated. There are a few observations regarding these data that are worth noting. First, $\mathcal{L}$ is isotropic. Second, $\mathcal{L}$ for all samples follow the same temperature dependence trend. Third, $\mathcal{L}$ for each sample investigated reaches the same value of 2.44x10^{-8}W-Ohm/K^2 as $T \rightarrow 0$K (completely degenerate limit of $\frac{\pi^2}{3}\left(\frac{k_B}{e}\right)^2$). Lastly, $\mathcal{L}$ and the hole carrier concentration (see Figures 3-8 and 3-9) follow the same trend. In other words, the higher the hole concentration the sample has, the higher its $\mathcal{L}$ value is at a given temperature.

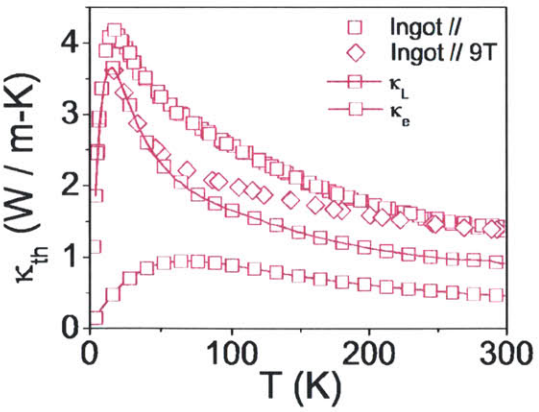

Figure 4-10: Plot of the calculated κ_L, calculated κ_e, κ_{th}, and κ_{th}(9T) of sample Ingot // as a function of temperature.

We would also like to learn whether the ℓ obtained from my electron and phonon models has any relationship with any other quantities. To do that, we compare ℓ with the ZT value at 297K, as well as ℓ with the carrier concentration value at 297K. Table 4.5 summarizes the results and we note a few interesting observations drawn from the table. First, the carrier concentration decreases as ℓ decreases for both the

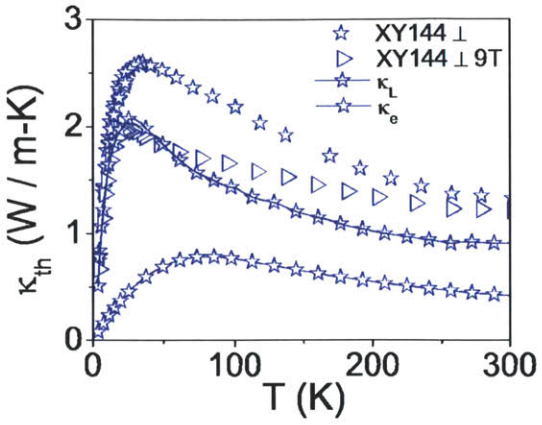

Figure 4-11: Plot of the calculated κ_L, calculated κ_e, κ_{th}, and κ_{th}(9T) of sample XY144 $\perp$ as a function of temperature.

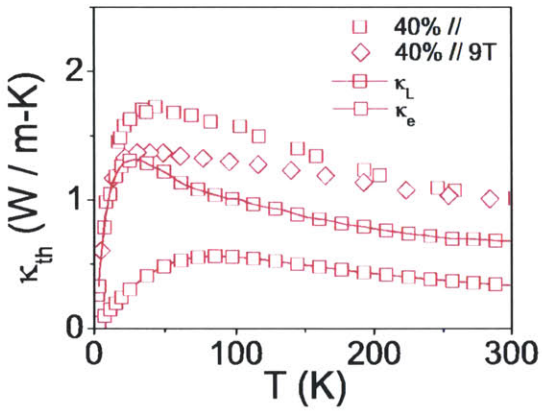

Figure 4-12: Plot of the calculated κ_L, calculated κ_e, κ_{th}, and κ_{th}(9T) of sample 40% // as a function of temperature.

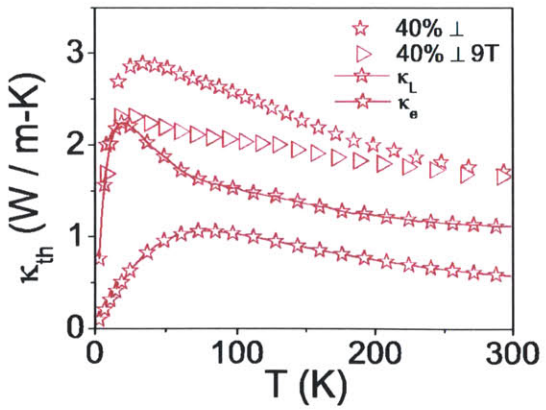

Figure 4-13: Plot of the calculated κ_L, calculated κ_e, κ_{th}, and κ_{th}(9T) of sample 40% $\perp$ as a function of temperature.

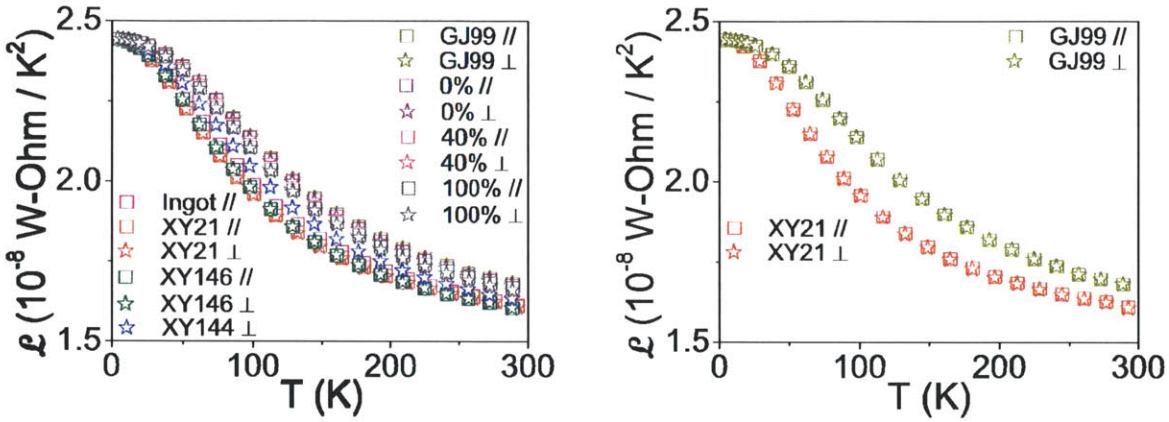

Figure 4-14: Plots of the Lorenz Number $\mathcal{L}$ of all samples investigated (left) and of samples XY21 and GJ99 (right) as a function of temperature. Sample XY21 has the lowest carrier concentration and sample GJ99 has the highest carrier concentration among all the measured samples. A few observations are worth noting. First, $\mathcal{L}$ is isotropic. Second, $\mathcal{L}$ for all samples follow the same temperature dependence trend. Third, $\mathcal{L}$ for each sample investigated reaches the same value of $2.44\text{x}10^{-8}$W-Ohm/K^2 as $T \rightarrow 0$K (completely degenerate limit of $\frac{\pi^2}{3}\left(\frac{k_B}{e}\right)^2$). Lastly, $\mathcal{L}$ and the hole carrier concentration (see Figures 3-9 and 3-8) follow the same trend. In other words, the higher the hole concentration the sample has, the higher its $\mathcal{L}$ value is at a given temperature.

Table 4.5: Comparison between the carrier concentration, ℓ, and ZT in both the // and $\perp$ directions.

Sample	*Maker*	*conc.*$(10^{19}cm^{-3})$ $T = 297K$	$\ell \perp$ (μm)	$ZT \perp$ $T = 297K$	ℓ // (μm)	ZT // $T = 297K$
GJ99	BC	3.520	3.93	0.761	3.47	0.755
0%	NTU	3.512	25.8	0.767	19.64	0.723
40%	NTU	3.203	19.64	0.695	9.83	0.690
100%	NTU	3.006	2.95	0.668	2.27	0.616
XY144	BC	2.616	3.69	0.882		
Ingot	Marlow	2.316			36.78	0.946
XY146	BC	2.054	3.69	0.888	3.28	0.925
XY21	BC	1.930	1.47	0.910	1.47	0.869

BC samples and the NTU samples. Second, for the BC samples measured in the $\perp$ direction, ZT increases as the carrier concentration decreases (or as ℓ decreases). Lastly, for the NTU samples measured in both the // and $\perp$ directions, ZT decreases as the % of nanoinclusions prepared via melt spinning in the nanocomposite sample increases (or as ℓ decreases).

4.6 Conclusions

In this chapter, the zero applied field experimental results are interpreted using both the semi-classical electron model and the semi-classical phonon model. From the electron model, we see that S depends only on the m^*, carrier concentration n, and λ, but not on other factors. Thus, for a materials system, S should be isotropic. Moreover, it is rather difficult to change S other than by changing its carrier concentration, as long as the dominant scattering mechanism does not change.

From the electron model fitting results, we observe that the dominant electron scattering mechanisms are acoustic phonon scattering, point defect / ionized impurity atom scattering, and neutral impurity atom scattering. We also observe that ℓ does not play a major role in the determination of ρ. Moreover, we find that the acoustic phonon scattering is the dominant electron scattering mechanism for $T >$

200K, while the point defect scattering mechanism is the dominant electron scattering mechanism for $T < 20$K. Furthermore, the deformation potential D_A is found to be both process dependent and materials dependent. Lastly, the ionized impurity atom concentration N_i and the neutral impurity atom concentration N_0 both reflect the somewhat anisotropic behavior in ρ of all samples investigated.

From the phonon model fitting results, we learn that ℓ plays a rather important role in the determination of κ_L, especially at low temperatures. We see that the Umklapp scattering contribution (B') has a materials dependent factor, where B' decreases from $\approx$10x10^{-18}s/K for the nanoparticles nanocomposite samples to $\approx$4x10^{-18}s/K for the nanocomposite sample made using 100% nanoinclusions prepared via melt spinning. Furthermore, we see that the point defect contribution (A') reaches the highest value when both the nanoparticles and nanoinclusions prepared via melt spinning are present in the nanocomposite samples (e.g. the 40% sample), similar to the alloying effect on the thermal conductivity. In general, it is desirable to increase the values of A' and B', resulting in a decrease in the κ_L values. However, care needs to be taken to ensure that the phonon parameters are independent of the electron parameters so that no adverse effect in ZT would result.

The determination of $\mathcal{L}$ is also carried out based on my electron model findings. We observe that $\mathcal{L}$ is isotropic. Moreover, $\mathcal{L}$ for each sample investigated reaches the same value of 2.44x10^{-8}W-Ohm/K^2 as $T \rightarrow 0$K (completely degenerate limit of $\frac{\pi^2}{3}\left(\frac{k_B}{e}\right)^2$). Furthermore, the higher the hole concentration the sample has, the higher is its $\mathcal{L}$ value at a given temperature. Lastly, I find that a lower ℓ leads to higher ZT values at 297K for the BC nanocomposite samples measured in the $\perp$ direction. On the other hand, a lower ℓ leads to lower ZT values at 297K for NTU nanocomposite samples measured in both the // and $\perp$ directions.

THIS PAGE INTENTIONALLY LEFT BLANK

Chapter 5

$(Bi_ySb_{1-y})_2Te_3$ Measurement Results Under an Applied Magnetic Field

This chapter examines the magnetic field effect on the $(Bi_ySb_{1-y})_2Te_3$ materials system. Measurement results are presented both as a function of temperature and magnetic field. The chapter concludes with a discussion of a simple analysis of the results.

5.1 Transport Measurement Results Under an Applied Magnetic Field

5.1.1 Results Using B = 3, 6, 9T

The transport properties for a few selected samples are studied under an applied magnetic field. The scenario where the field is applied perpendicular to the transport direction (denoted by B $\perp$ Q) is carried out. Figures 5-1 to 5-3 together with Figures E-1 to E-6 show the results of all the measurements taken on all samples under an applied magnetic field. Please note that due to the limitations in sample size and in QD PPMS, the ρ data under an applied B field for samples in the // direction are not available. From the figures noted above, we clearly see that an applied B field

affects the conduction carriers by slowing their heat and current conducting ability (i.e. by decreasing the κ_{th} values while increasing the S and ρ values of the conduction carriers). The effect is especially pronounced below 200K. As a result, an increase in ZT at low temperature is observed.

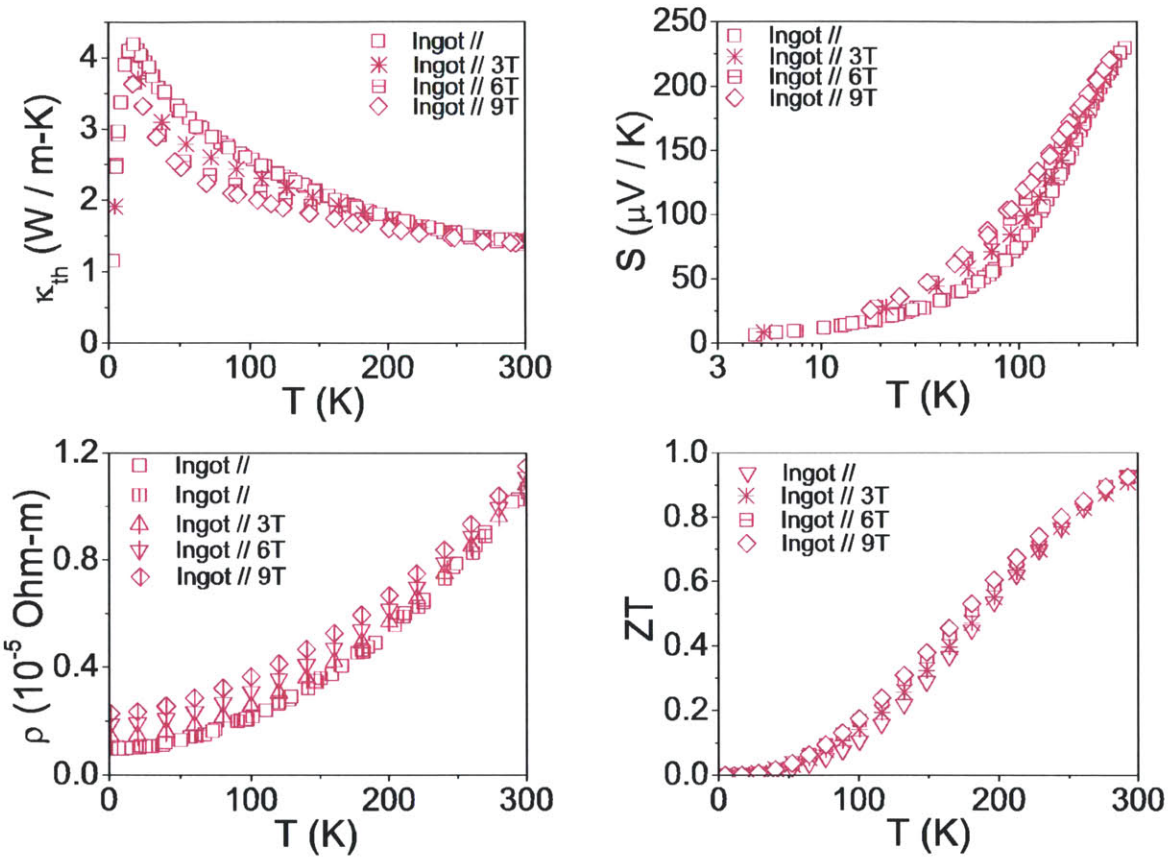

Figure 5-1: Plots of κ_{th}, S, ρ, and ZT of sample Ingot // as a function of temperature under applied magnetic field strengths of 0, 3, 6, and 9T. The plots clearly show that the applied B field decreases the sample's κ_{th} values, while increasing the sample's S and ρ values. As a result, an increase in ZT at low temperature is observed. The effect is especially pronounced below 200K.

5.1.2 Results Using B = 1, 2, 3, 4, 5, 6, 7, 8, 9T

For the samples to which we apply various magnetic fields, it is interesting to observe that the κ_{th} values below certain temperature ranges do not change with increasing

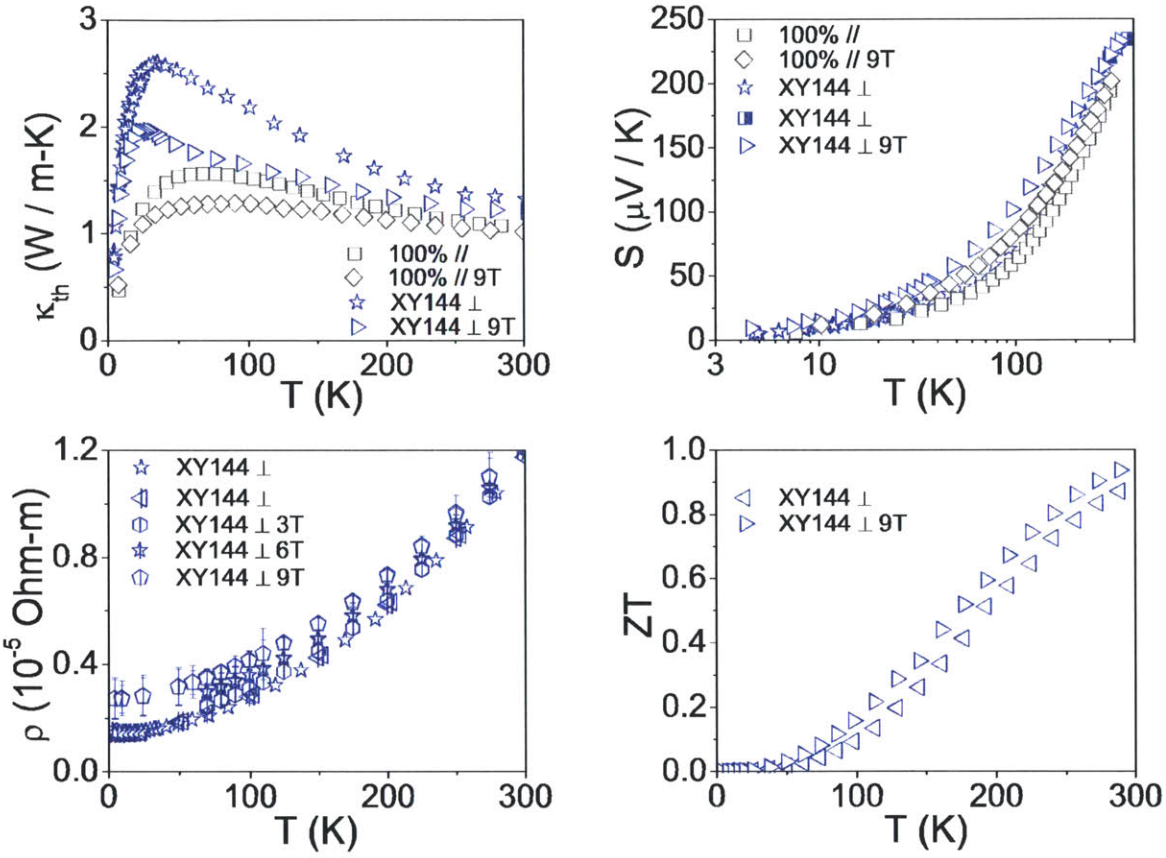

Figure 5-2: Plots of κ_{th}, S, ρ, and ZT of sample XY144 $\perp$ as a function of temperature under applied magnetic field strengths of 0 and 9T, along with the effect of 6T and 9T fields on XY144 $\perp$'s ρ. Also shown is the plot of κ_{th} and S of sample 100% as a function of temperature under applied magnetic field strengths of 0 and 9T. The plots clearly show that the applied B field decreases the sample's κ_{th} values, while increasing the sample's S and ρ values. As a result, an increase in ZT at low temperature is observed. The effect is especially pronounced below 200K.

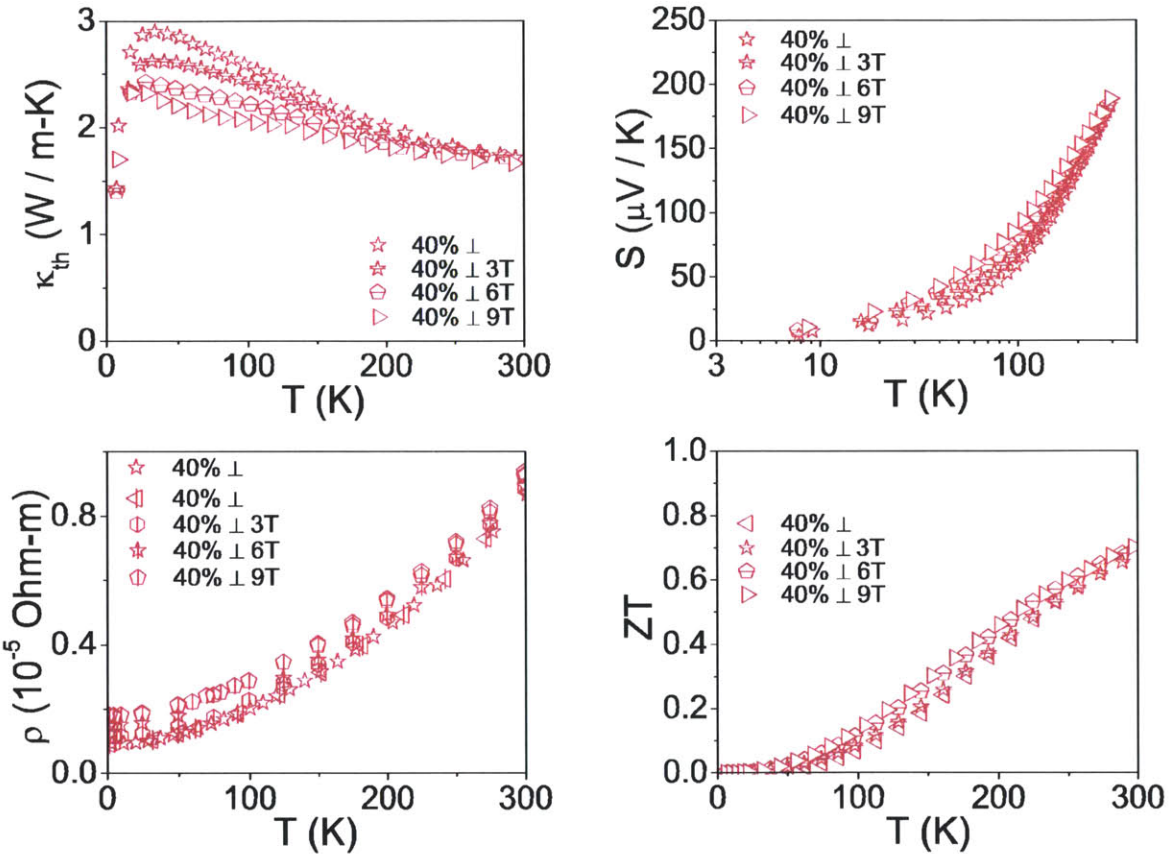

Figure 5-3: Plots of κ_{th}, S, ρ, and ZT of sample 40% $\perp$ as a function of temperature under applied magnetic field strengths of 0, 3, 6, and 9T. The plots clearly show that the applied B field decreases the sample's κ_{th} values, while increasing the sample's S and ρ values. As a result, an increase in ZT at low temperature is observed. The effect is especially pronounced below 200K.

magnetic field strength. This piece of information is extremely important as it leads to the extraction of the actual Lorenz Number ($\mathcal{L}$) of the sample. To pursue this research direction further, we study samples Ingot //, 40% //, and 40% $\perp$ under six more magnetic field strengths below 100K (see Figures 5-4 to 5-6). Please be advised that the goals of plotting these three figures in this fashion are simply (a) to illustrate the vast amount of data collected, (b) to demonstrate that the temperature-dependenct plots may not necessarily provide the most intuitive approach to looking at the data, and (c) the magnitude of the error bars for the ρ measurements typically increases with increasing applied magnetic field strength.

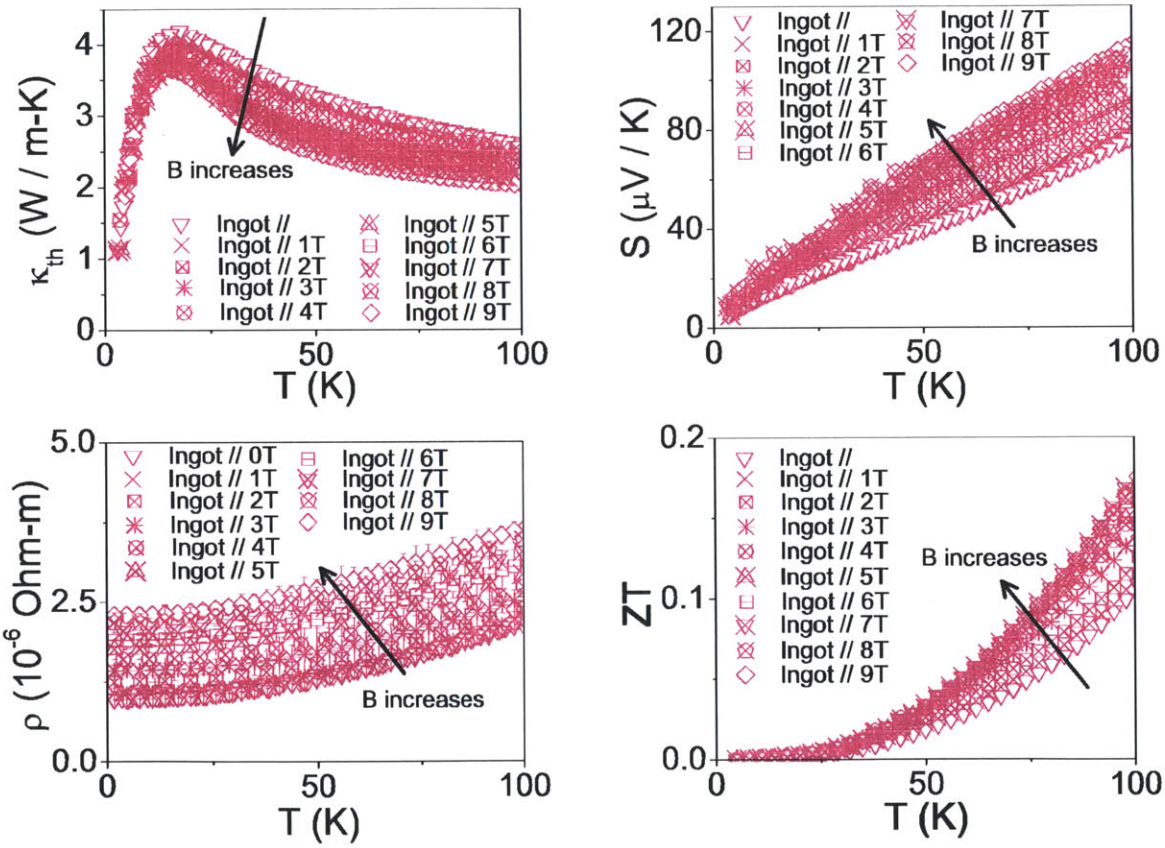

Figure 5-4: Plots of κ_{th}, S, and ρ of sample Ingot // as a function of temperature under applied magnetic field strengths of 0, 1, 2, 3, 4, 5, 6, 7, 8, and 9T. This figure shows that the ρ's error bar typically increases with increasing applied magnetic field strength. The goal of showing this figure is to illustrate the vast amount of data collected.

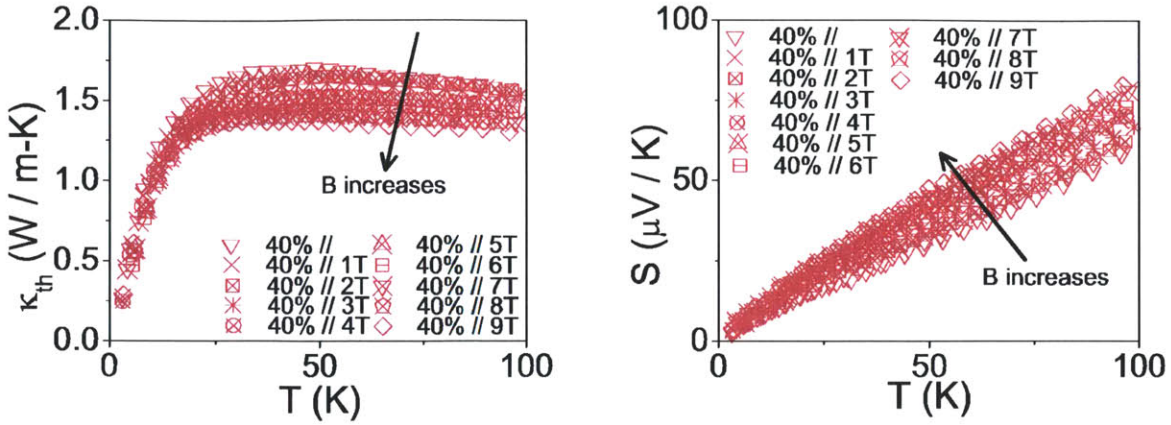

Figure 5-5: Plots of κ_{th} and S of sample 40% // as a function of temperature under applied magnetic field strengths of 0, 1, 2, 3, 4, 5, 6, 7, 8, and 9T. The goal of showing this figure is to illustrate the vast amount of data collected.

To better visualize the effect of the applied magnetic field on κ_{th}, S, ρ, and ZT, we interpolate the results in T, divide each κ_{th}, S, ρ, and ZT value by its B=0T counterpart at an interpolated temperature (denoted as the κ_{th} ratio, S ratio, ρ ratio, and ZT ratio), and plot them against B for numerous temperature values (see Figures 5-7 to 5-15). Please note that each interpolated T is represented by one colored symbol. Let us use an example to better demonstrate my "ratio" definition. At interpolated T = 26K, Ingot // has the following properties: (a) κ_{th}(0T) = 3.95W/(m-K), (b) κ_{th}(9T) = 3.27W/(m-K), (c) S(0T) = 23.80μV/K, (d) S(9T) = 37.86μV/K, (e) ρ(0T) = 1.083μOhm-m, (f) ρ(9T) = 2.407μOhm-m, (g) ZT(0T) = 0.00344, and (h) ZT(9T) = 0.00473. As a result, at 26K Ingot //'s 9T κ_{th} ratio = 3.27/3.95 = 0.828, 9T S ratio = 37.86/23.80 = 1.591, 9T ρ ratio = 2.407/1.083 = 2.22, and 9T ZT ratio = 0.00473/0.00344 = 1.377.

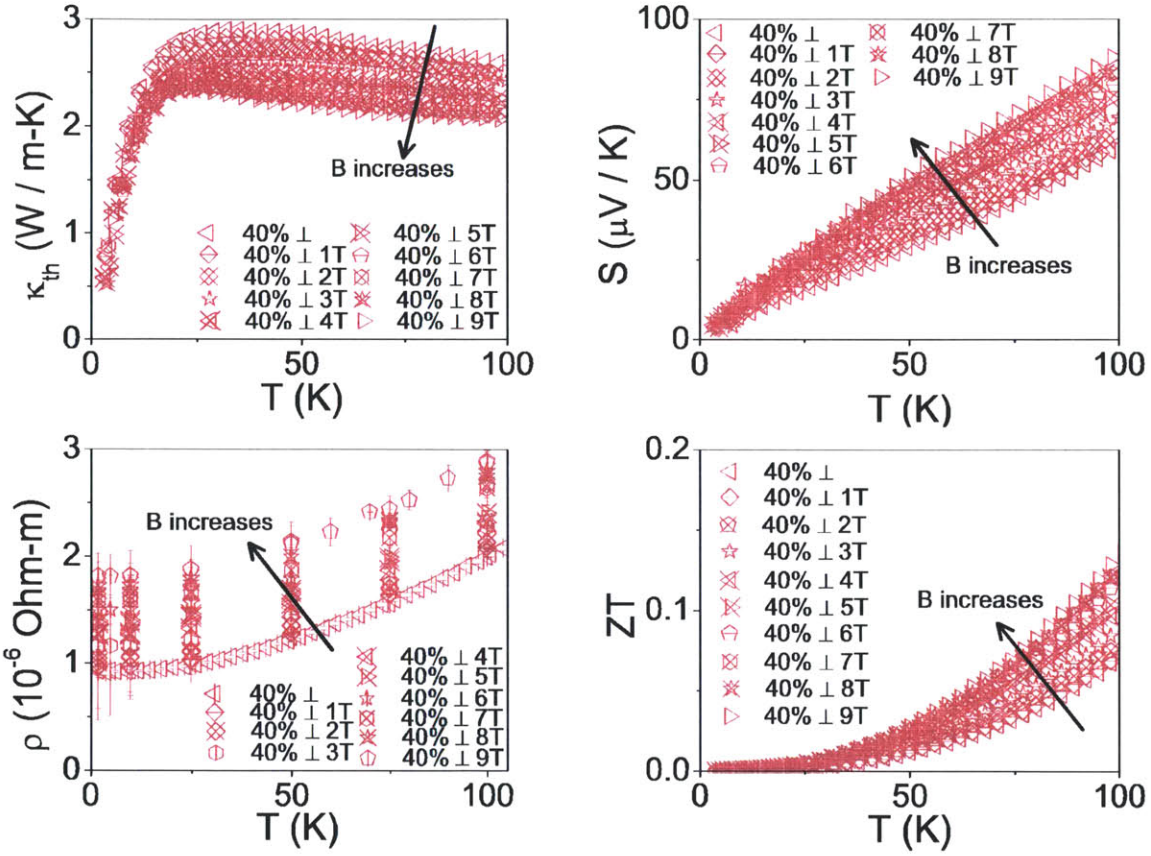

Figure 5-6: Plots of κ_{th}, S, and ρ of sample 40% $\perp$ as a function of temperature under applied magnetic field strengths of 0, 1, 2, 3, 4, 5, 6, 7, 8, and 9T. This figure shows that the ρ's error bar typically increases with increasing applied magnetic field strength. The goal of showing this figure is to illustrate the vast amount of data collected.

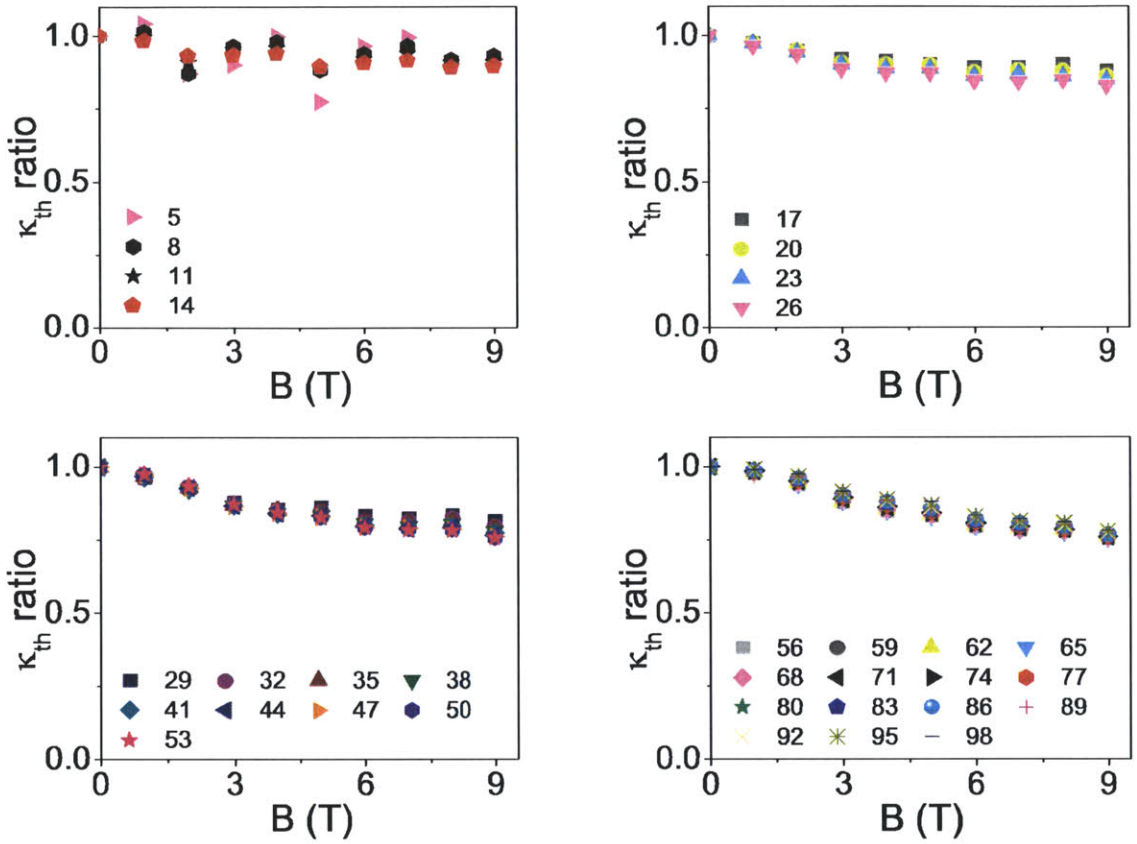

Figure 5-7: Plots of the κ_{th} ratio of sample Ingot // as a function of applied magnetic field at numerous interpolated temperatures for T < 100K. The numbers in each plot represent the interpolated temperatures. The κ_{th} ratio value is obtained through dividing its value by its B=0T counterpart. For example, at interpolated T=26K, Ingot //'s $\kappa_{th}(0T)$ = 3.95W/(m-K) and $\kappa_{th}(9T)$ = 3.27W/(m-K). As a result, Ingot //'s 9T κ_{th} ratio at 26K = 3.27/3.95 = 0.828.

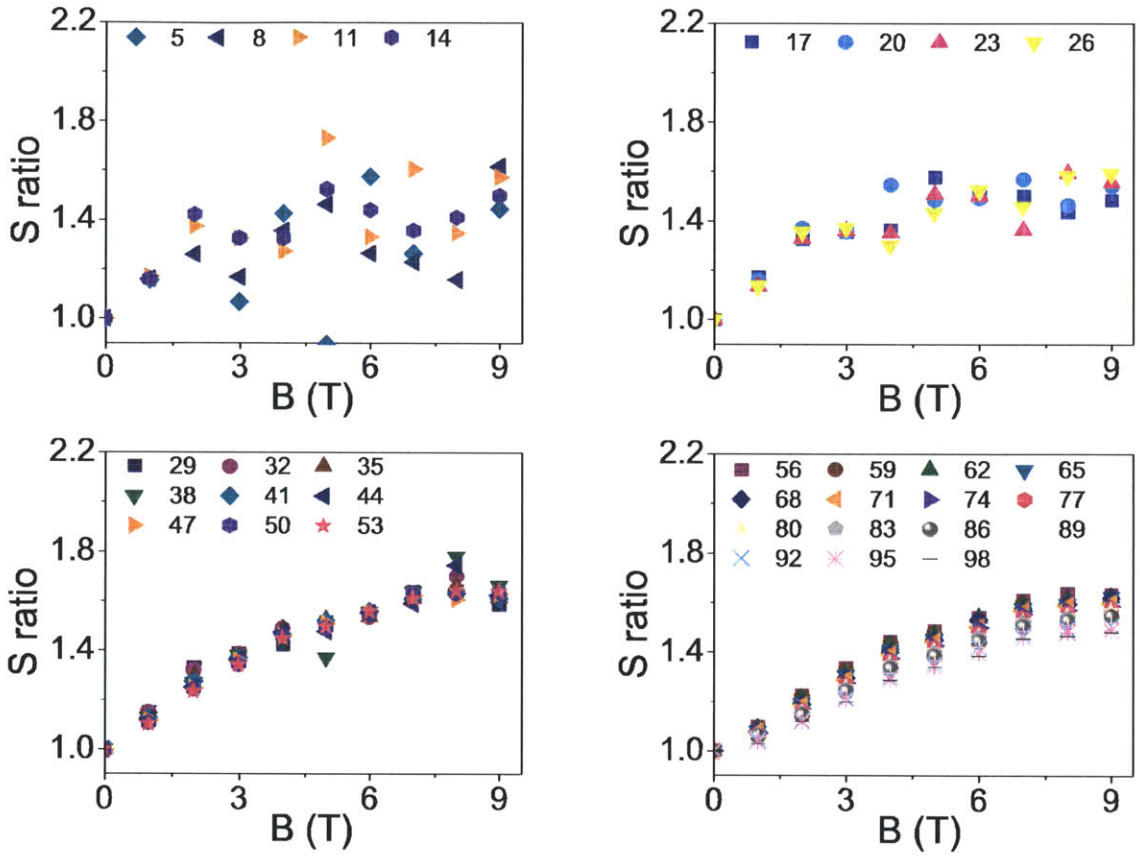

Figure 5-8: Plot of the S ratio of sample Ingot // as a function of applied magnetic field at numerous interpolated temperatures for T $<$ 100K. The numbers in each plot represent the interpolated temperatures. The S ratio value is obtained through dividing its value by its B=0T counterpart. For example, at interpolated T=26K, Ingot //'s $S(0\text{T}) = 23.80\mu\text{V/K}$ and $S(9\text{T}) = 37.86\mu\text{V/K}$. As a result, Ingot //'s 9T S ratio at 26K $= 37.86/23.80 = 1.591$.

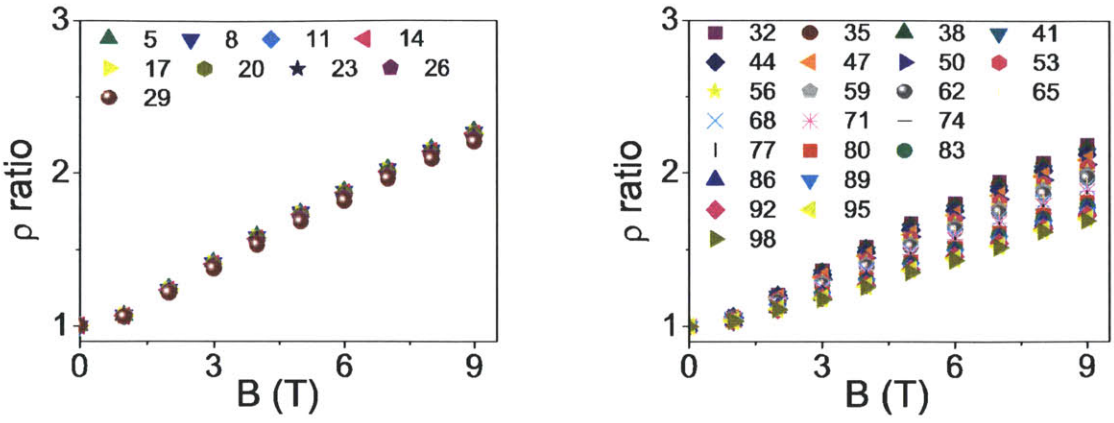

Figure 5-9: Plot of the ρ ratio of sample Ingot // as a function of applied magnetic field at numerous interpolated temperatures for T < 100K. The numbers in each plot represent the interpolated temperatures. The ρ ratio value is obtained through dividing its value by its B=0T counterpart. For example, at interpolated T=26K, Ingot //'s ρ(0T) = 1.083μOhm-m and ρ(9T) = 2.407μOhm-m. As a result, Ingot //'s 9T ρ ratio at 26K = 2.407/1.083 = 2.22.

5.2 Discussions

5.2.1 Magnetic Field Dependent Behaviors

Figures 5-7 to 5-16 show that a plateau in κ_{th} is reached below a certain temperature with B approaching 9T for all samples investigated. This information allows one to extract $\mathcal{L}$ experimentally in this temperature range. Moreover, this serves as an important guideline to confidentially extend the $\mathcal{L}$ calculation beyond this temperature range as we have seen in Section 4.5. Furthermore, the κ_{th} data show that the applied magnetic field pushes the holes away in Ingot // more effectively than in the nanocomposite samples for measurements carried out at the same temperature. We also observe that both S and ρ of all samples investigated increase with magnetic field below 100K, with ρ increasing linearly with the magnetic field. The only exception is that S for Ingot // reaches a plateau above a certain magnetic field strength. The overall effect is that the ZT ratio always increases with increasing B field, especially for the 40% $\perp$ nanocomposite sample. We also notice that the ZT

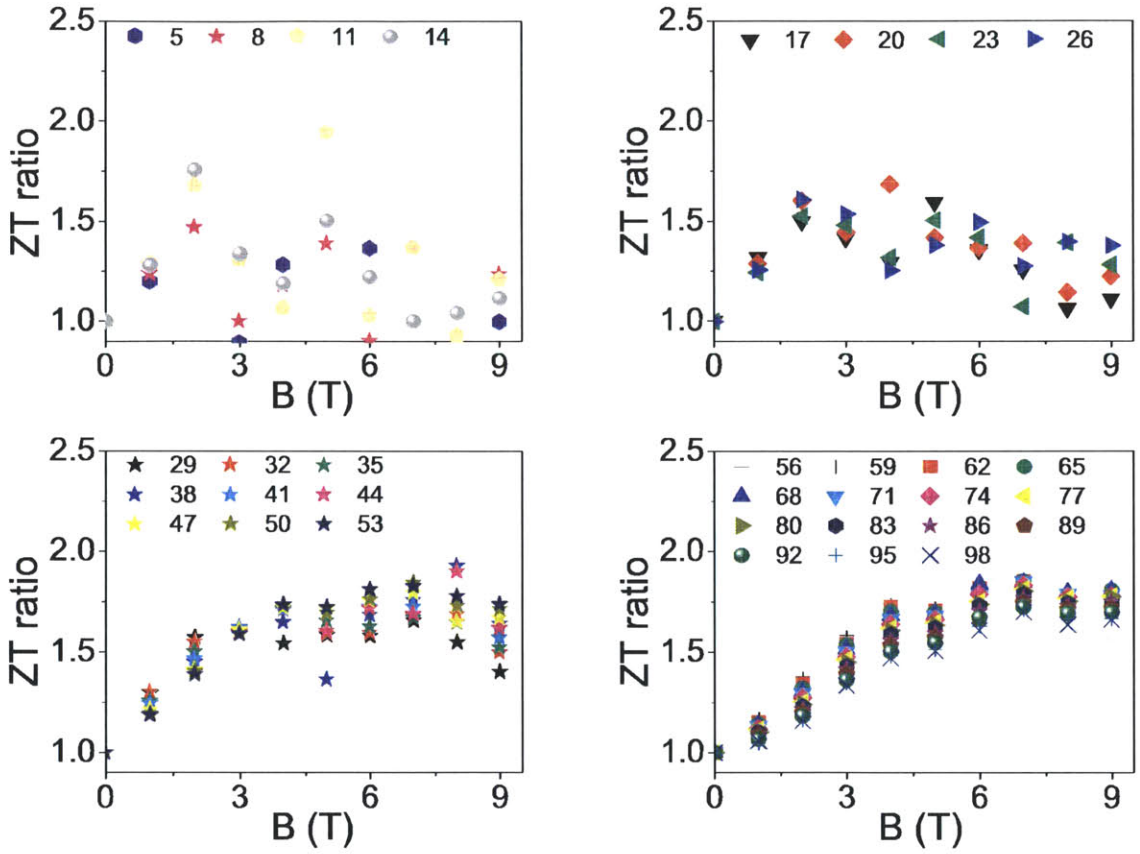

Figure 5-10: Plot of the ZT ratio of sample Ingot // as a function of applied magnetic field at numerous interpolated temperatures for T < 100K. The numbers in each plot represent the interpolated temperatures. The ZT ratio value is obtained through dividing its value by its B=0T counterpart. For example, at interpolated T=26K, Ingot //'s $ZT(0\text{T}) = 0.00344$ and $ZT(9\text{T}) = 0.00473$. As a result, Ingot //'s 9T ZT ratio at 26K = 0.00473/0.00344 = 1.377.

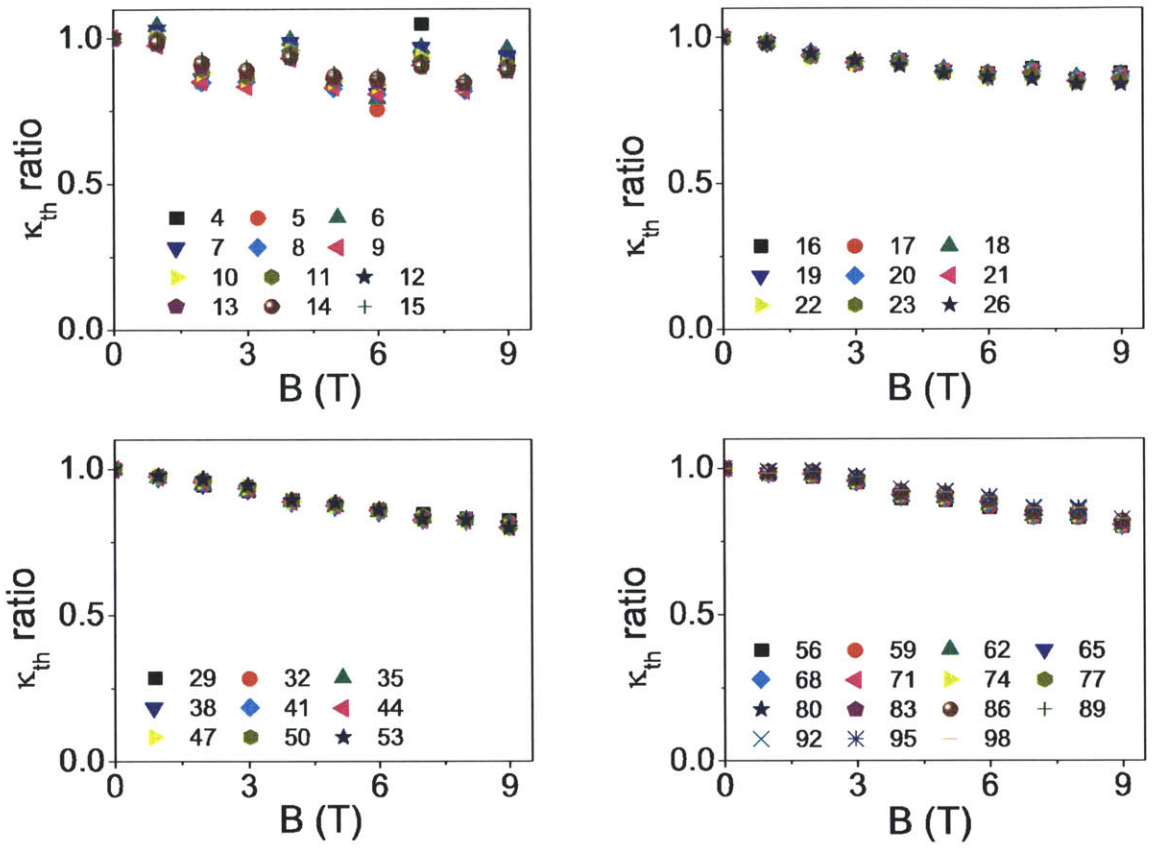

Figure 5-11: Plots of the κ_{th} ratio of sample 40% // as a function of applied magnetic field at numerous interpolated temperatures for T < 100K. The numbers in each plot represent the interpolated temperatures. The κ_{th} ratio value is obtained through dividing its value by its B=0T counterpart. For example, at interpolated T=26K, Ingot //'s κ_{th}(0T) = 3.95W/(m-K) and κ_{th}(9T) = 3.27W/(m-K). As a result, Ingot //'s 9T κ_{th} ratio at 26K = 3.27/3.95 = 0.828.

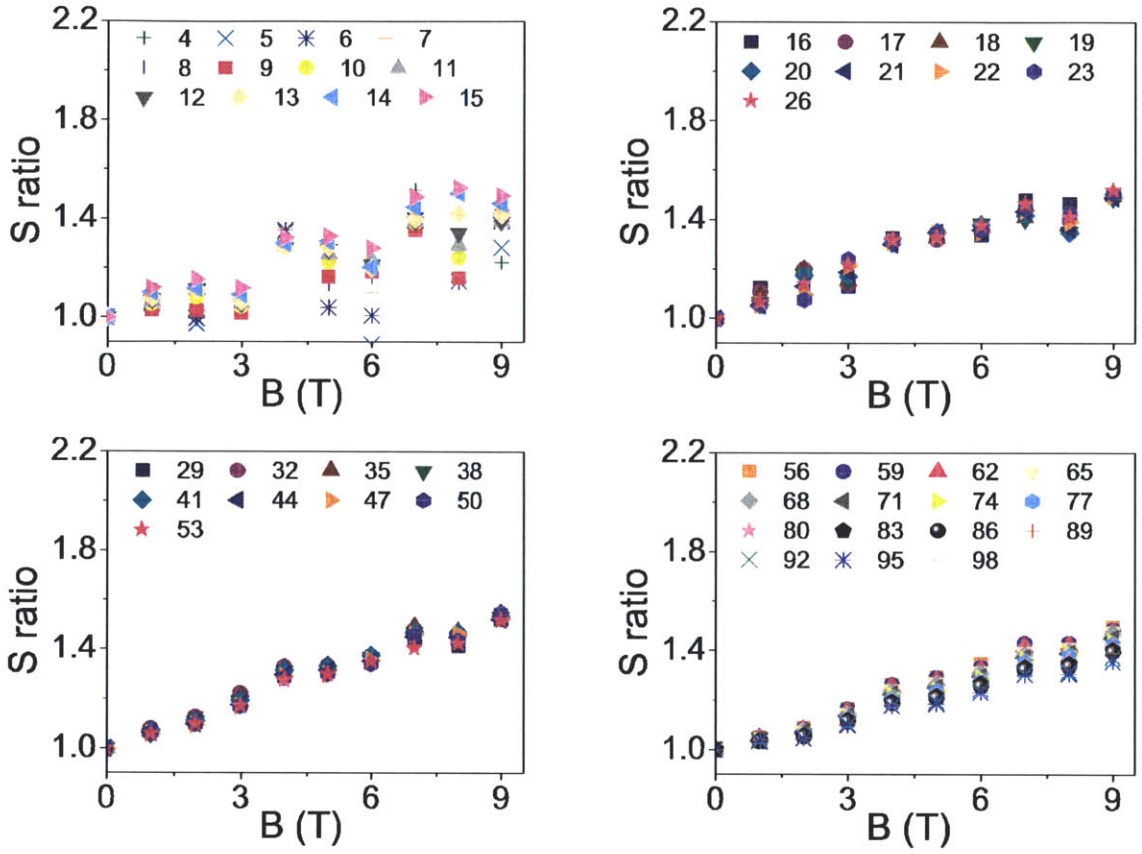

Figure 5-12: Plot of the S ratio of sample 40% // as a function of applied magnetic field at numerous interpolated temperatures for T < 100K. The numbers in each plot represent the interpolated temperatures. The S ratio value is obtained through dividing its value by its B=0T counterpart. For example, at interpolated T=26K, Ingot //'s $S(0\text{T}) = 23.80\mu\text{V/K}$ and $S(9\text{T}) = 37.86\mu\text{V/K}$. As a result, Ingot //'s 9T S ratio at 26K = 37.86/23.80 = 1.591.

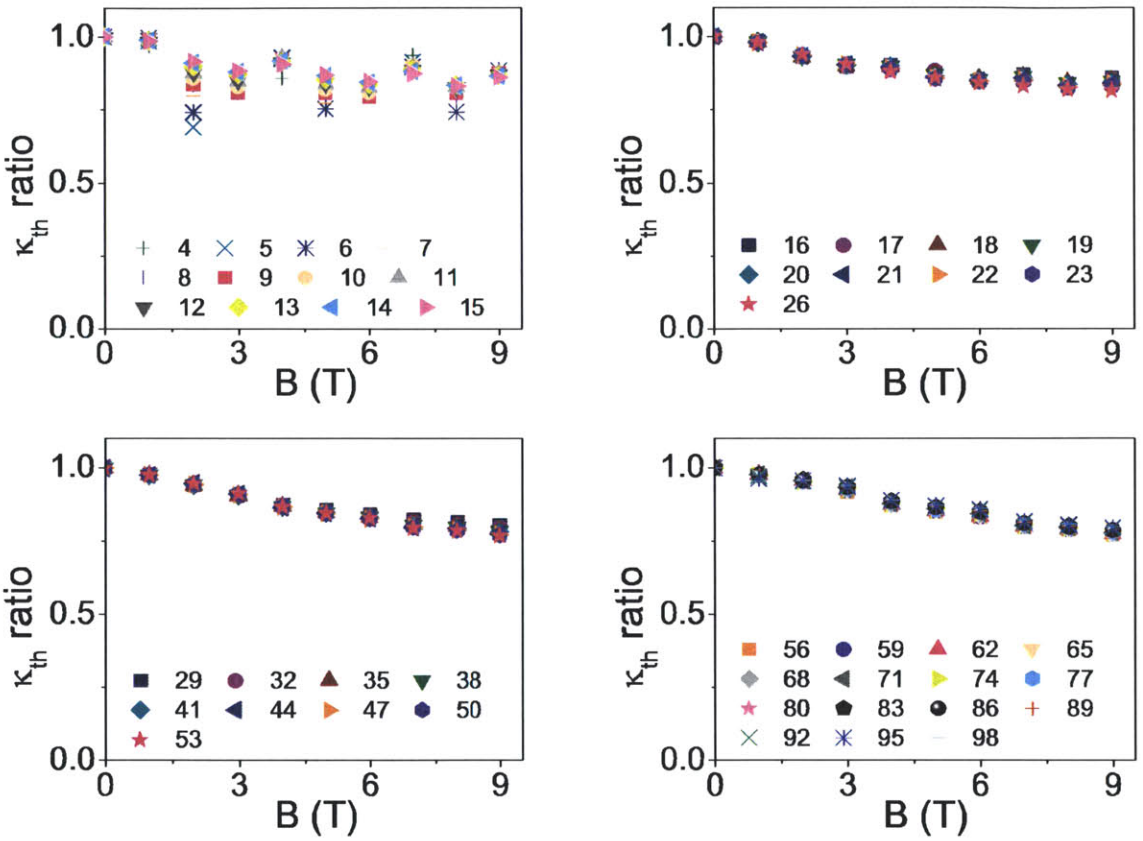

Figure 5-13: Plots of the κ_{th} ratio of sample 40% $\perp$ as a function of applied magnetic field at numerous interpolated temperatures for T $<$ 100K. The numbers in each plot represent the interpolated temperatures. The κ_{th} ratio value is obtained through dividing its value by its B=0T counterpart. For example, at interpolated T=26K, Ingot //'s κ_{th}(0T) = 3.95W/(m-K) and κ_{th}(9T) = 3.27W/(m-K). As a result, Ingot //'s 9T κ_{th} ratio at 26K = 3.27/3.95 = 0.828.

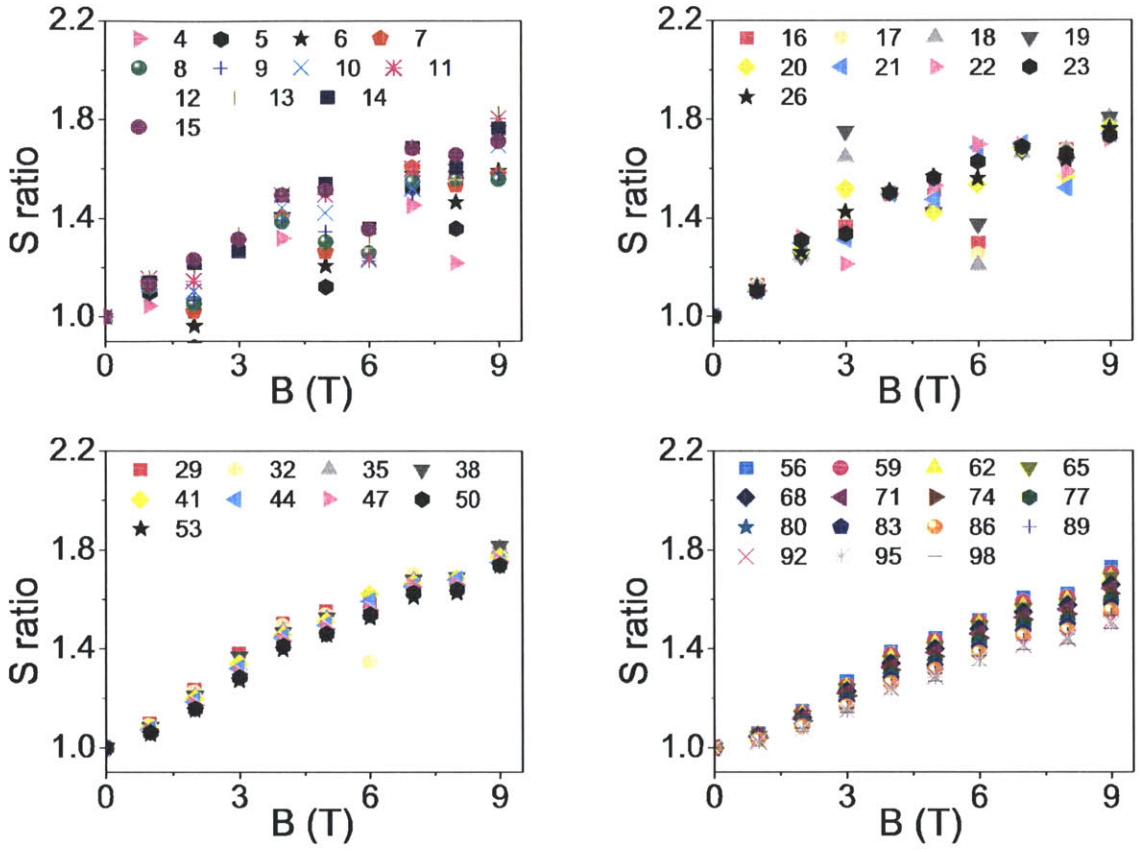

Figure 5-14: Plot of the S ratio of sample 40% $\perp$ as a function of applied magnetic field at numerous interpolated temperatures for T $<$ 100K. The numbers in each plot represent the interpolated temperatures. The S ratio value is obtained through dividing its value by its B=0T counterpart. For example, at interpolated T=26K, Ingot //'s $S(0\text{T}) = 23.80\mu\text{V/K}$ and $S(9\text{T}) = 37.86\mu\text{V/K}$. As a result, Ingot //'s 9T S ratio at 26K $= 37.86/23.80 = 1.591$.

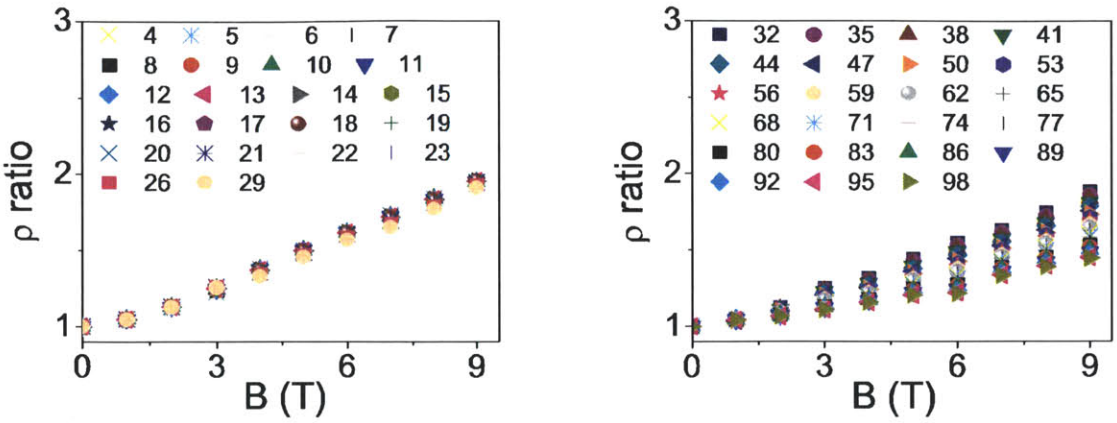

Figure 5-15: Plot of the ρ ratio of sample 40% $\perp$ as a function of applied magnetic field at numerous interpolated temperatures for T $<$ 100K. The numbers in each plot represent the interpolated temperatures. The ρ ratio value is obtained through dividing its value by its B=0T counterpart. For example, at interpolated T=26K, Ingot //'s ρ(0T) = 1.083μOhm-m and ρ(9T) = 2.407μOhm-m. As a result, Ingot //'s 9T ρ ratio at 26K = 2.407/1.083 = 2.22.

ratio behavior follows closely with the S ratio behavior (i.e. a plateau is observed in ZT ratio if a plateau is observed in S ratio). It seems that S ratio plays a bigger role in determining the ZT ratio. This finding suggests that applying a magnetic field is one of the low-hanging fruit ways of increasing the performance of a thermoelectric material. Table 5.1 summaries the observations from Figures 5-7 to 5-15.

The S ratio data under an applied magnetic field look rather noisy at a first glance. This noisy S ratio behavior at low T is believed to be due to the fact that $S \rightarrow 0\mu$V/K as $T \rightarrow$ 0K. As a result, the S signal-to-noise ratio decreases as T decreases. However, upon closer examination on the κ_{th} and S data, there seem to exist an oscillatory pattern in the low temperature data, especially for the NTU 40% sample. More studies need to be carried out to confirm this interesting phenomenon.

5.2.2 Comparison between κ_L and $\kappa_{th,\text{plateau}}$

Although the 40% sample is not fabricated using solely ball-milled nanoparticles, it is still interesting to compare the κ_{th} plateau value ($\kappa_{th,\text{plateau}}$) found in the 40% $\perp$

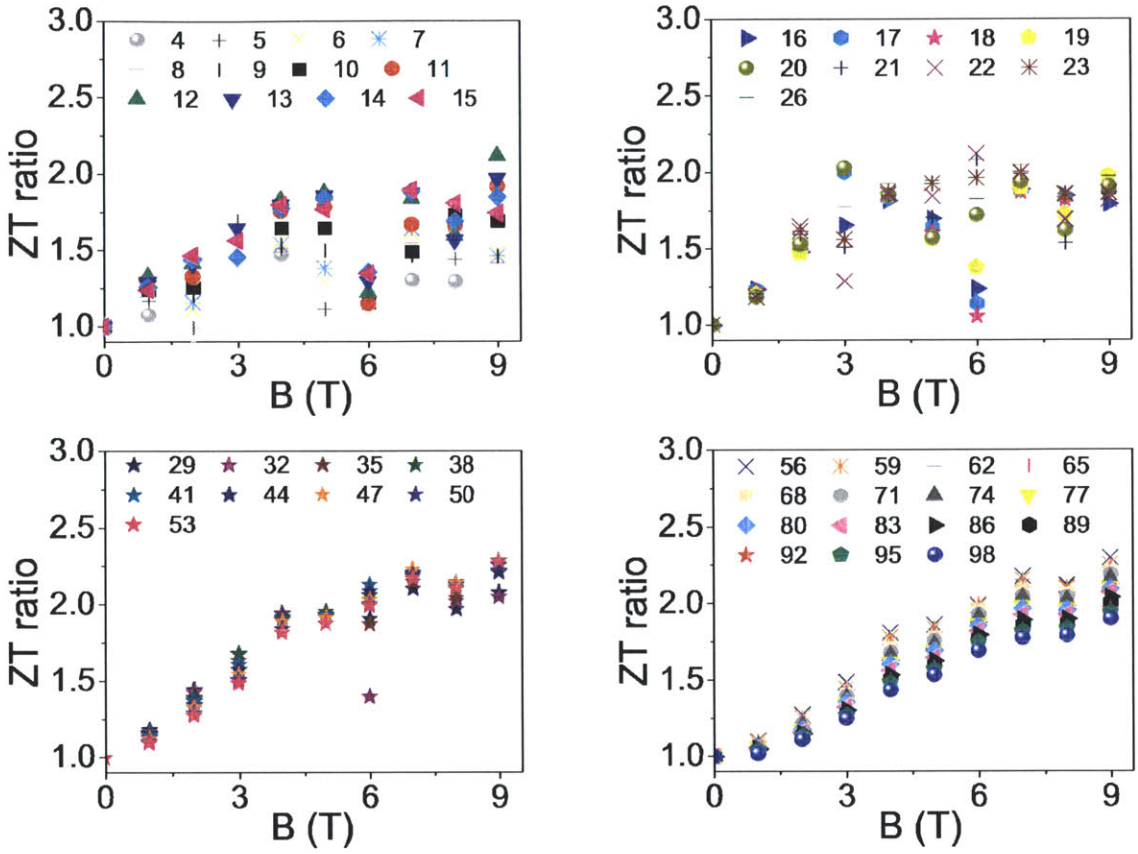

Figure 5-16: Plot of the ZT ratio of sample 40% $\perp$ as a function of applied magnetic field at numerous interpolated temperatures for T < 100K. The numbers in each plot represent the interpolated temperatures. The ZT ratio value is obtained through dividing its value by its B=0T counterpart. For example, at interpolated T=26K, Ingot //'s $ZT(0\text{T}) = 0.00344$ and $ZT(9\text{T}) = 0.00473$. As a result, Ingot //'s 9T ZT ratio at 26K = 0.00473/0.00344 = 1.377.

Table 5.1: The applied magnetic field dependence of various features in the κ_{th} ratio, the S ratio, and the ρ ratio for samples Ingot //, 40% //, and 40% $\perp$ samples for $T < 100$K. The features are extracted from Figures 5-7 to Figures 5-16, and the temperature ranges for different behaviors are described.

Sample	*Property*	*T (K)*	*Feature*
Ingot //	κ_{th} ratio	5-14	Plateau is quickly reached $\sim$ 2T
		17-26	Plateau is reached $\sim$ 6T
		29-53	Plateau is reached $\sim$ 8T
		56-98	Plateau is not reached by 9T
	S ratio	5-14	too noisy to conclude
		17-26	Plateau is reached $\sim$ 4T
		29-53	Plateau is reached $\sim$ 8T
		56-98	Plateau is reached $\sim$ 8T, but the rate of the ratio increase $\downarrow$ as $T \uparrow$
	ρ ratio	5-29	ratio $\uparrow$ linearly
		32-98	ratio $\uparrow$ linearly, but the rate of the ratio increase $\downarrow$ as $T \uparrow$
	ZT ratio	5-26	too noisy to conclude
		29-98	Plateau is reached $\sim$ 6T
40% //	κ_{th} ratio	4-15	Plateau is quickly reached $\sim$ 3T
		16-26	Plateau is reached $\sim$ 8-9T
		29-53	Plateau is not reached by 9T
		56-98	Plateau is not reached by 9T
	S ratio	4-15	too noisy to conclude
		16-26	ratio $\uparrow$
		29-53	ratio $\uparrow$
		56-98	ratio $\uparrow$, but the rate of the ratio increase $\downarrow$ as $T \uparrow$
40% $\perp$	κ_{th} ratio	4-15	Plateau is quickly reached $\sim$ 3T
		16-26	Plateau is reached $\sim$ 8-9T
		29-53	Plateau is not reached by 9T
		56-98	Plateau is not reached by 9T
	S ratio	4-15	too noisy to conclude
		16-26	ratio $\uparrow$
		29-53	ratio $\uparrow$
		56-98	ratio $\uparrow$, but the rate of the ratio increase $\downarrow$ as $T \uparrow$
	ρ ratio	4-29	ratio $\uparrow$ linearly
		32-98	ratio $\uparrow$ linearly, but the rate of the ρ ratio increase $\downarrow$ as $T \uparrow$
	ZT ratio	4-26	too noisy to conclude
		29-53	Plateau is reached $\sim$ 8T
		56-98	ratio $\uparrow$, but the rate of the ratio increase $\downarrow$ as $T \uparrow$

sample with the $\kappa_{L,\perp}$ from Table 3.6 (see Table 5.2). We notice that the ($\kappa_{th,\text{plateau}}$) values obtained are much higher than the κ_L values extracted in Chapter 3. This finding is indeed expected since it is almost impossible to increase any sample's ρ to infinity without breaking it. As a result, we should always treat the κ_L values extracted under the method described in Section 3.5 as the theoretical limit, whereas the $\kappa_{th,\text{plateau}}$ values obtained under the method described in this section should be considered as the realistic values for κ_L in the practical limit.

Table 5.2: Comparison between $\kappa_{L,\perp}$ from Table 3.6 and the plateau κ_{th} ($\kappa_{th,\text{plateau}}$) from Figures 5-6 and 5-13. The difference between the two values suggests that the κ_L values extracted under the method described in Section 3.5 should be treated as the theoretical limit, whereas the $\kappa_{th,\text{plateau}}$ values obtained under the method described in this section should be considered as the realistic values in the practical limit.

T (K)	$\kappa_{L,\perp}$ *from Table 3.6 (W/m-K)*	$\kappa_{th,plateau}$ *from Figures 5-6 and 5-13 (W/m-K)*
50	1.53	2.20
26	1.36	2.34

5.2.3 9T Ratio as a Function of Temperature

From Figures 5-7 to 5-16, we observe that some of the ratio quantities seem to be temperature independent. To further examine the ratio temperature-dependent behavior, the 9T ratio of all quantities of various samples are plotted together (see Figure 5-17).

Figure 5-17 shows numerous interesting phenomena for both the Ingot // and the nanocomposite samples under an 9T applied magnetic field. First, the ρ ratio is found to be constant up to a certain temperature T_{flat} for nanocomposite samples. From Section 4.5, we know that the dominant scattering mechanism for carriers for $T < T_{flat}$ is point defect scattering. Moreover, we see that our results obey Kohler's rule [69]. In other words, a higher B field is needed for samples with higher point defect concentration to give the same magnetoresistance results. Second, the minimum of the κ_{th} ratio occurs at a temperature $T_{min} > T_{flat}$. Third, the peak of the S

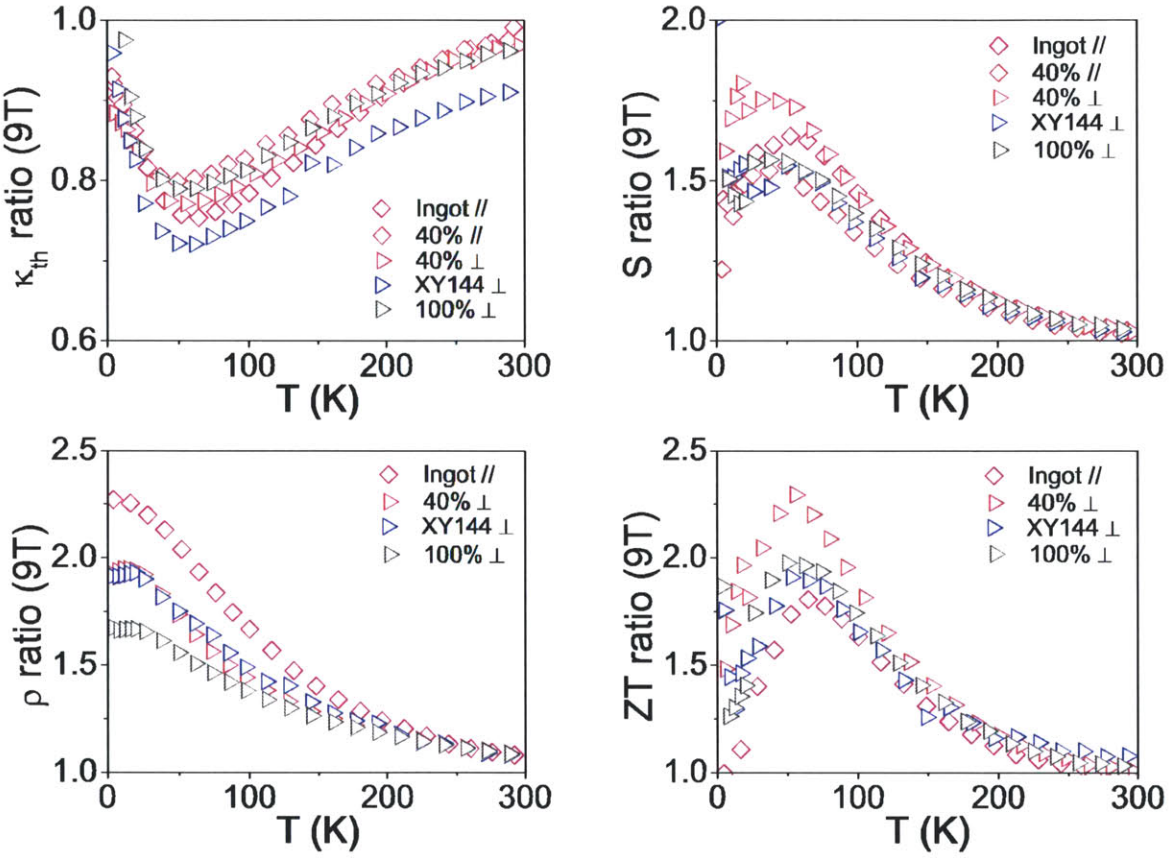

Figure 5-17: Plots of the κ_{th} ratio, S ratio, ρ ratio, and ZT ratio of various samples as a function of temperature with an applied magnetic field of 9T.

ratio and ZT ratio occur at a temperature $T_{peak} > T_{flat}$. And not surprisingly, $T_{min} \sim T_{peak} \sim T_{cross}$. Thus, the temperature at which various scattering mechanisms switch their role of dominance is an important temperature from a physics perspective. Lastly, we observe that the S ratio increases the most for the 40% sample. From these observations, we conclude that an applied magnetic field has a greater effect on carriers when the point defect scattering is the dominant carrier scattering mechanism. It is interesting to wonder what would happen to the ZT ratio if the point defect scattering dominant region is extended to higher temperatures. Will the ZT peak shift to a higher T?

5.3 Conclusions

From the magnetic field studies on the Ingot and on the 40% samples, a few important facts are demonstrated. First, an applied magnetic field can be used to effectively increase the ZT of $(Bi_ySb_{1-y})_2Te_3$, especially at temperatures below 200K. Use of a magnetic field might theoretically extend the effective temperature ranges over which $(Bi_ySb_{1-y})_2Te_3$ materials can be used for refrigeration. Second, the data under various applied B fields allow me to confidently calculate the $\mathcal{L}$ value below the temperature ranges where a plateau has occurred. Third, the data under various applied B fields serve as an important guideline for both validating any electron model and extrapolating values for $\mathcal{L}$ above the plateau occurrence temperatures. As a result, this allows me to get some insights into the temperature dependence of $\mathcal{L}$ (see Figure 4-14). Fourth, from the magnetic field dependent transport studies on our samples, we observe that the applied B field pushes away the holes more effectively in the Ingot // than the holes in the nanocomposite samples. Moreover, an oscillatory pattern seems to exist in the low temperature data, especially for the NTU 40% sample. More studies need to be carried out to confirm this interesting phenomenon. Furthermore, we also find that the $\kappa_{th,\text{plateau}}$ values obtained under the magnetic field study serve as a more realistic and practical limit for κ_L. Lastly, from the magnetic field dependent studies, we find that having point defects as the dominant scattering

mechanism for the carriers results in an increase in ZT under an applied magnetic field. It would be extremely useful if one could make a sample such that the point defect dominant regime is extended to higher temperatures, resulting in a shift of the increase in the ZT ratio regime under an applied magnetic field to a temperature range closer to room temperature (300K). However, care needs to be taken to ensure that such modifications would result in an increase in the ZT values under an applied magnetic field.

Chapter 6

Conclusions and Future Directions

This thesis concludes with a brief summary of the findings and some thoughts for future research studies. These are summarized in the following sections.

6.1 Conclusions

In this thesis, I demonstrate that our QD PPMS apparatus is well calibrated and can produce accurate data through numerous benchmark efforts. The mass density, XRD, SEM, κ_{th}, S, ρ, and carrier concentration measurements are carried out on eight $(Bi_{0.2}Sb_{0.8})_2Te_3$ samples. The sample set includes: (a) a bulk ingot from Marlow (Ingot), (b) four nanocomposite samples (XY21, XY146, XY144, and GJ99) made by collaborators from Boston College (BC) where the letters simply indicate the sample maker's initials, and (c) three nanocomposite samples (0%, 40%, and 100%) made by collaborators from Nanyang Technological University (NTU) in Singapore where the % denotes the weight % of the nanoinclusions prepared via melt spinning [1] in the sample.

From our results, we observe that the addition of nanoinclusions prepared via melt sinning decreases the mass density of a sample. We also find that the carrier concentration varies among the samples investigated (see Figure 3-9), leading us to believe that the carrier concentration is an extremely fabrication process dependent parameter. Moreover, we observe that κ_{th} and ρ are somewhat anisotropic, while S is

isotropic in all of the nanocomposite samples investigated. Furthermore, we observe that the nanocomposite approach decreases the values of the carrier mobility, the values of ℓ_e, and the values of ℓ_{ph}, especially for $T < 200$K. Nevertheless, ℓ_e and ℓ_{ph} are still a few orders of magnitude smaller than the average size of the grain boundaries ℓ estimated from my electron and phonon models. Due to the uniaxial pressing nature of the fabrication process of a nanocomposite sample, samples with the same composition made using machines from different manufacturers probably cannot be regarded as one materials system in the // press direction. However, since there is no pressure coming from the sides during the nanocomposite fabrication, samples with the same composition made using machines from different manufacturers can indeed be considered as one materials system in the $\perp$ press direction (see Figures 3-24). This assumption is only valid if all the samples under investigation have similar ℓ values. Additionally, the nanocomposite approach is found to be able to further lower the κ_L value (see Section 3.5 for the κ_L extraction procedures). Using the 297K case as an example, the nanocomposite $\kappa_{L,\perp}$ of 0.76W/m-K is 0.14W/m-K lower than the previously reported 0.9W/m-K κ_L(300K) value for $(Bi_{0.3}Sb_{0.7})_2Te_3$ [4]. In this quick comparison, $(Bi_{0.3}Sb_{0.7})_2Te_3$ is assumed to have the lowest κ_L(300K) values among all the $(Bi_ySb_{1-y})_2Te_3$ alloys.

An electron model and a phonon model based on the semi-classical transport model are used to interpret the zero applied B field results. Using my models, the hole masses are found to be temperature-dependent ($m^* \propto T^{0.12}$). We also find that the acoustic phonon scattering mechanism dominates for $T > 200$K and the point defect scattering mechanism dominates for $T < 20$K for the holes. On the other hand, the boundary scattering, point defect / alloy scattering, and Umklapp scattering mechanisms all play a role for the phonon transport. Moreover, we find that the calculated ℓ values (which are in the μm ranges) play a major role in the phonon transport, but not in the carrier transport. Comparing the magnitudes between ℓ_e, ℓ_{ph}, and ℓ, it is believed that the values of ℓ could be lowered even further to further reduce κ_{th} without affecting the electrical carriers too much. The Lorenz Number $\mathcal{L}$ is found to be isotropic, to decrease with increasing temperature, and to

have a correlation with the carrier concentration (the higher the hole concentration the sample has, the higher its $\mathcal{L}$ value is at a given temperature). Furthermore, $\mathcal{L}$ reaches the same value of 2.44x10^{-8}W-Ohm/K^2 as $T \rightarrow$ 0K (which is the completely degenerate limit of $\frac{\pi^2}{3}\left(\frac{k_B}{e}\right)^2$). We also find that the carrier concentration decreases as ℓ decreases, and that ZT increases as the carrier concentration decreases (or as ℓ decreases) for all the samples investigated. Nevertheless, the carrier concentration cannot be decreased indefinitely since carriers are needed for the thermoelectric device itself.

Lastly, from our magnetic field dependence studies, we find that S and ρ increase under an applied B field, while κ_{th} decreases. The overall effect is an increase in the ZT values under an applied B field, especially for $T <$ 200K. Moreover, we also find that the applied B field pushes away the holes in the Ingot // more effectively than the holes in the nanocomposite samples. At low enough temperatures ($T <$ 26K), a plateau in κ_{th} is observed with an applied B field greater than 6T for the Ingot // sample and for a B field greater than 8T for the 40% nanocomposite samples, respectively. The existence of a plateau in κ_{th} under an applied B field is a great way to compute the $\mathcal{L}$ values experimentally. The plateau can also be used for validating any electron models and serves as a guidance for extrapolating $\mathcal{L}$ to temperatures outside the plateau existence regions. Using the 40% $\perp$ sample to compare the $\kappa_{th,\text{plateau}}$ with the $\kappa_{L,\perp}$ extracted (see Section 3.5), we found that the $\kappa_{th,\text{plateau}}$ values are much higher than the $\kappa_{L,\perp}$ extracted values (see Table 5.2). The difference between the two values suggests that the κ_L values extracted under the method described in Section 3.5 should be treated as the theoretical limit, whereas the $\kappa_{th,\text{plateau}}$ values obtained under the method described in Section 5.1 should be considered as the realistic values in the practical limit.

Finally, from the magnetic field dependent studies, we find that having point defects as the dominant scattering mechanism for the carriers results in an increase in ZT under an applied magnetic field. It would be extremely useful if one could make a sample such that the point defect dominant regime is extended to higher temperatures, resulting in a shift of the increase in the ZT ratio regime to a temperature

range closer to room temperature (300K). However, care needs to be taken to ensure that such modifications would result in an increase in the ZT values under an applied magnetic field.

6.2 Future Directions

In this thesis, I have shown many interesting findings, especially under the variations of temperature and applied magnetic field. It would be interesting to further study my observed phenomena under an applied magnetic field greater than 9T. From my findings, it is concluded that the magnetic field has the most pronounced effect on increasing ZT values when the point defect scattering mechanism is the dominating carrier scattering mechanism. It would be interesting to test this concept on a materials system that has a relatively large point defect scattering contribution. As Professor Dresselhaus suggested, an ion implanted sample with controlled fluences would be an ideal candidate for this experiment. Moreover, we observe that the decrease in ℓ through the nanocomposite approach results in an improvement in ZT, mainly due to the increase in scattering of phonons without too much increase in the scattering of the carriers. It would be interesting to test whether this belief is the ultimate correct approach. The reason is that the improvement in ZT values under an applied B field is mainly due to the increase in the S values. Therefore, it would be interesting to test whether some degree of carrier scattering is beneficial. As suggested by Professor Hagelstein, materials system such as Indium Antimonide (InSb) that is known to have long mean free path would be a good candidate for this test. Similarly, one could also study nanocomposite samples with ℓ omthe order of nm instead of μm. Furthermore, we should confirm whether the electrons behave similarly to the holes regarding the behaviors found in this thesis. In addition, it would be ideal that others can confirm my findings with a different nanocomposite samples set, especially about the relationship between the ZT, ℓ, and carrier concentration. Finally, it would also be valuable to understand the fabrication parameters that lead to the anisotropic behavior observed in the thermoelectric properties of the

nanocomposite samples.

THIS PAGE INTENTIONALLY LEFT BLANK

Appendix A

Additional Transport Measurement Results

Appendix A shows the results of the temperature-dependent κ_{th}, S, and ρ measurements under no applied magnetic field for samples for which my results are not displayed in Section 3.5. Please refer back to Section 3.4 for the complete sample's description and to Section 3.5 for the detailed discussion of these results.

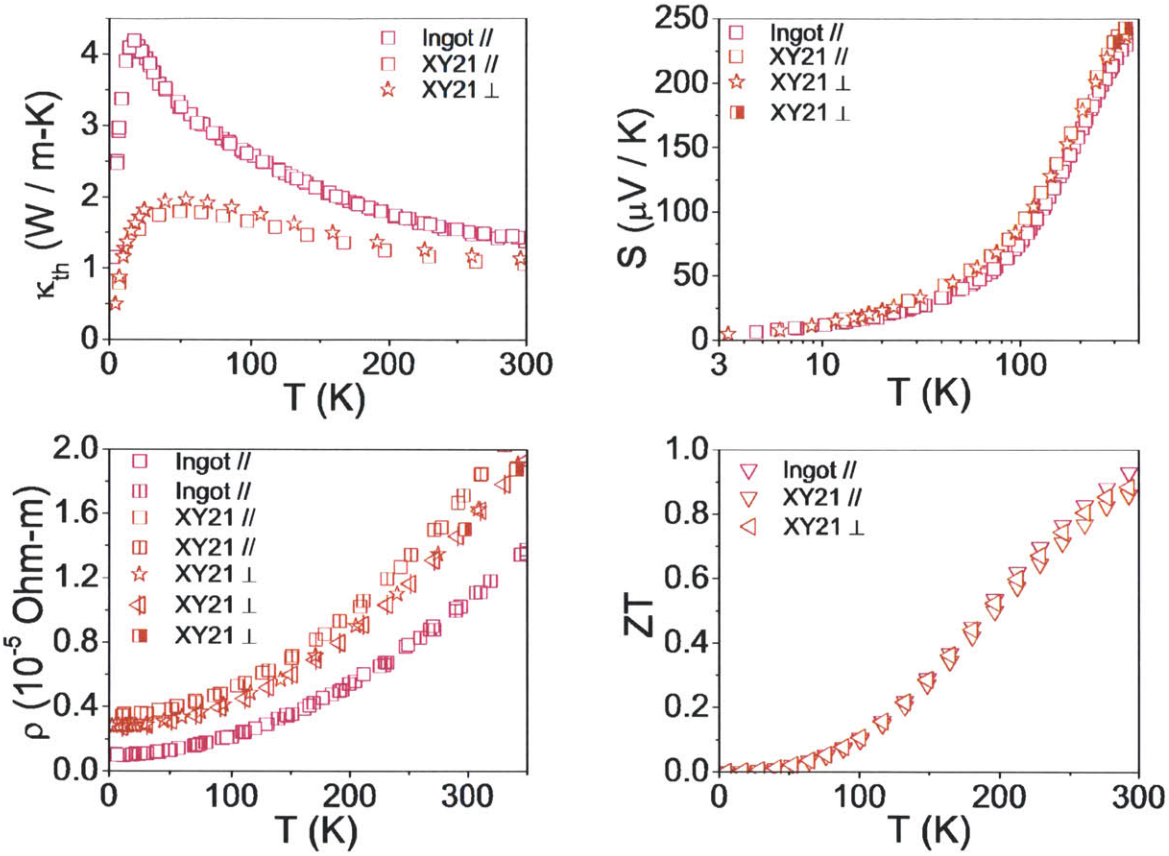

Figure A-1: Plots of κ_{th}, S, ρ, and ZT of samples XY21 and Ingot // as a function of temperature. Anisotropic behavior is observed in κ_{th} and ρ, but not in S. No significant difference is observed between results from (a) QD PPMS vs. ZEM3, and (b) 2-pt ρ (TTO) vs. 4-pt ρ (ACT) (see Table 3.3 for the representation of each symbol and color). A data display control is used for sample XY21 to show only one out of every five to ten points, while a data display control is used for sample Ingot // to show only one out of every five to thirty points.

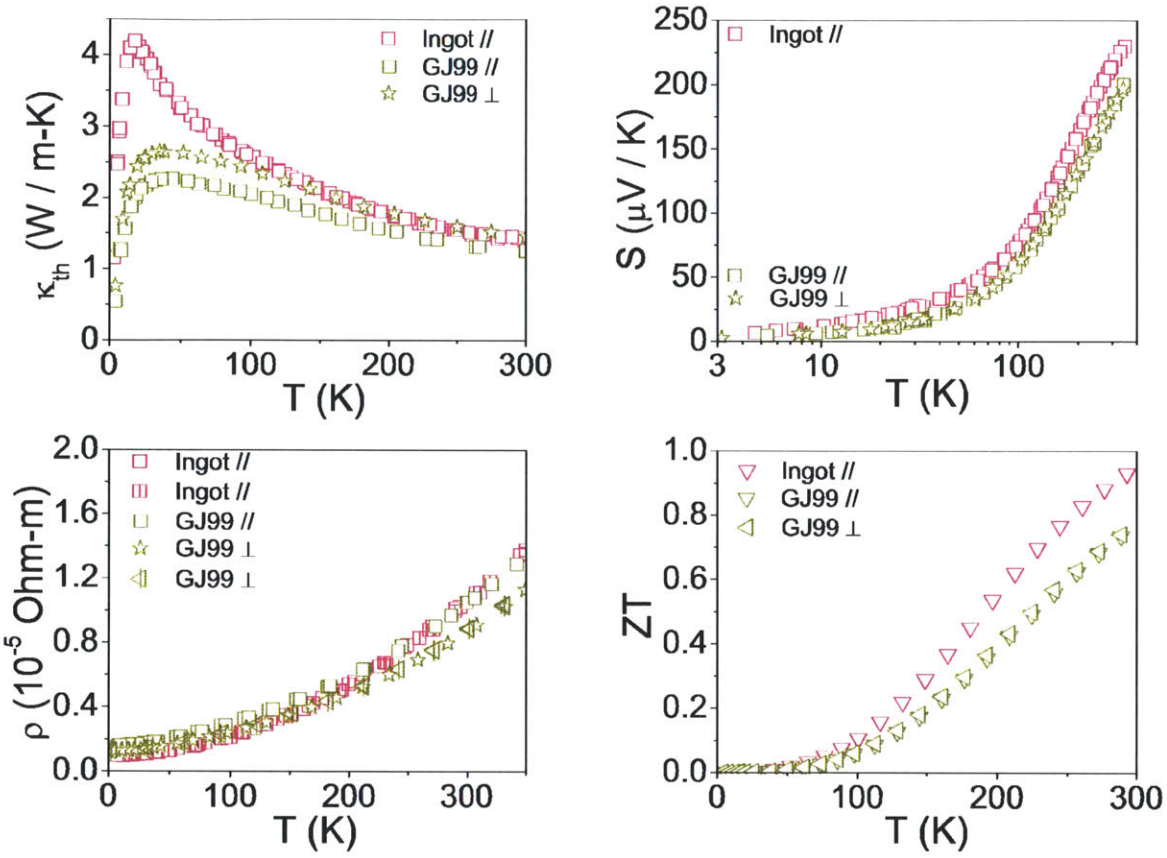

Figure A-2: Plots of κ_{th}, S, ρ, and ZT of samples GJ99 and Ingot // as a function of temperature. Anisotropic behavior is observed in κ_{th} and ρ, but not in S. No significant difference is observed between results from 2-pt ρ (TTO) vs. 4-pt ρ (ACT) (see Table 3.3 for the representation of each symbol and color). A data display control is used for sample GJ99 to show only one out of every three to thirty points, while a data display control is used for sample Ingot // to show only one out of every five to thirty points.

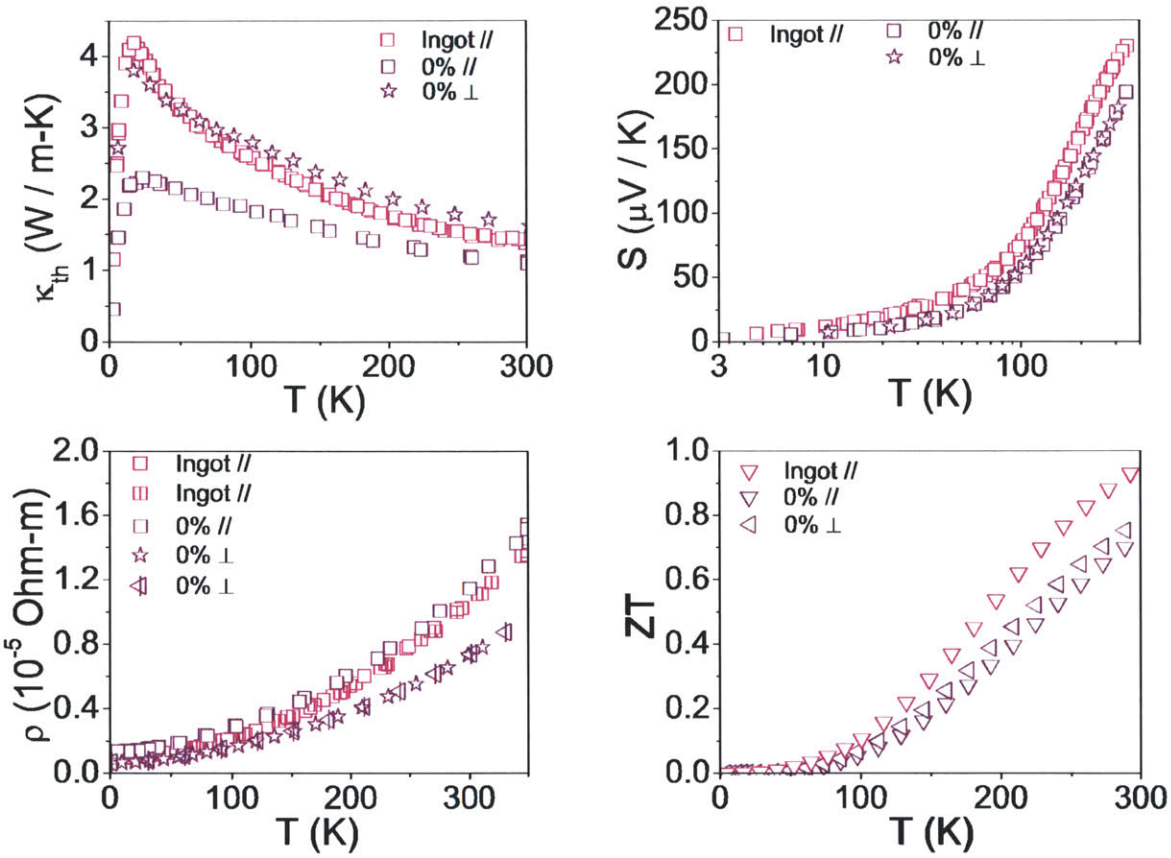

Figure A-3: Plots of κ_{th}, S, ρ, and ZT of samples 0% and Ingot // as a function of temperature. Anisotropic behavior is observed in κ_{th} and ρ, but not in S. No significant difference is observed between results from 2-pt ρ (TTO) vs. 4-pt ρ (ACT) (see Table 3.3 for the representation of each symbol and color). A data display control is used for sample 0% to show only one out of every three to thirty points, while a data display control is used for sample Ingot // to show only one out of every five to thirty points.

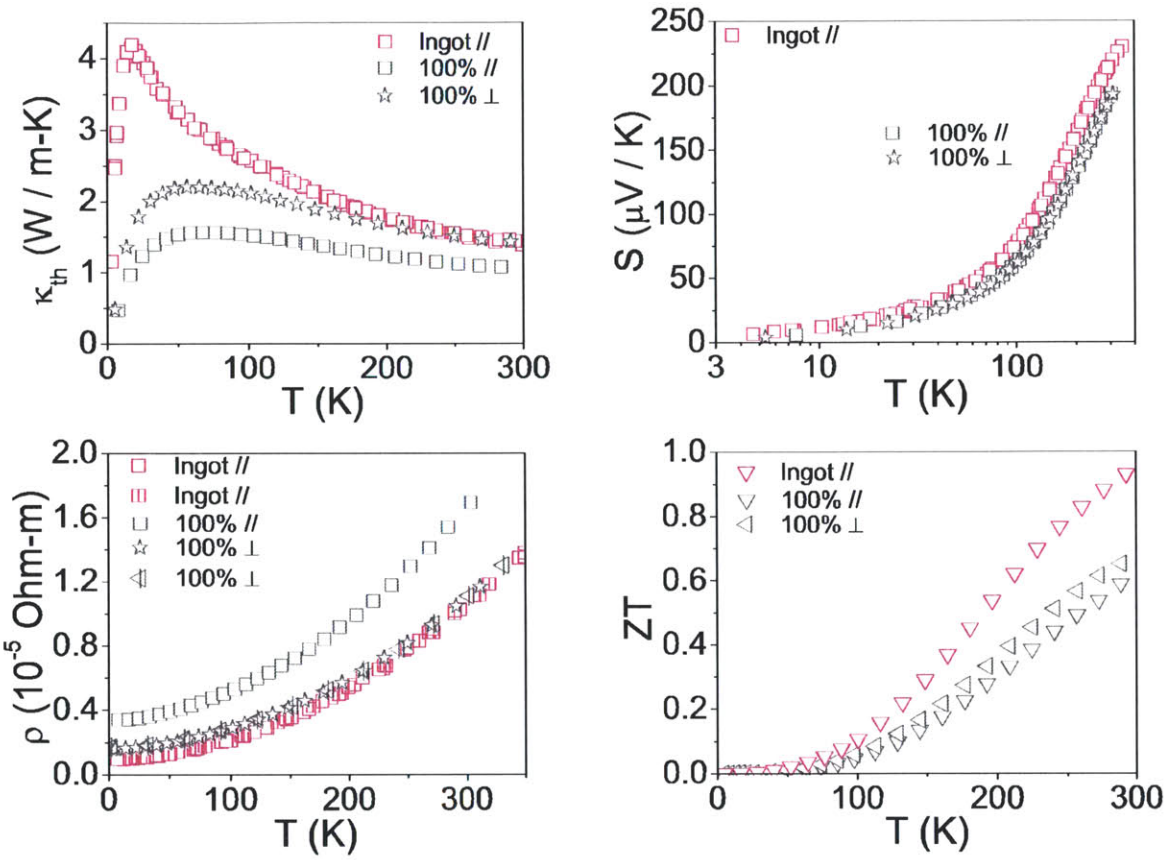

Figure A-4: Plots of κ_{th}, S, ρ, and ZT of samples 100% and Ingot // as a function of temperature. Anisotropic behavior is observed in κ_{th} and ρ, but not in S. No significant difference is observed between results from 2-pt ρ (TTO) vs. 4-pt ρ (ACT) (see Table 3.3 for the representation of each symbol and color). A data display control is used for sample 100% to show only one out of every three to thirty points, while a data display control is used for sample Ingot // to show only one out of every five to thirty points.

THIS PAGE INTENTIONALLY LEFT BLANK

Appendix B

Additional Hole Mobility Results

Appendix B shows the results of the temperature-dependent hole mobility results for samples for which my results are not displayed in Section 3.5.1. Please refer back to Section 3.4 for the complete sample's description and to Section 3.5.1 for the detailed discussion of these results.

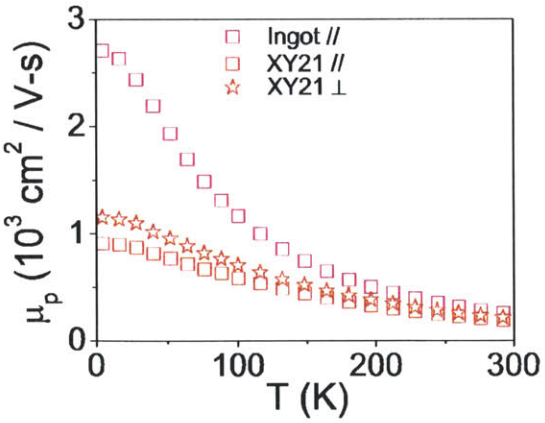

Figure B-1: Plot of the hole mobility μ_p of samples XY21 and Ingot // as a function of temperature.

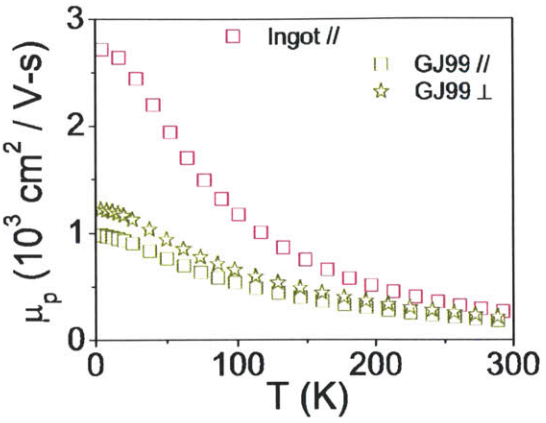

Figure B-2: Plot of the hole mobility μ_p of samples GJ99 and Ingot // as a function of temperature.

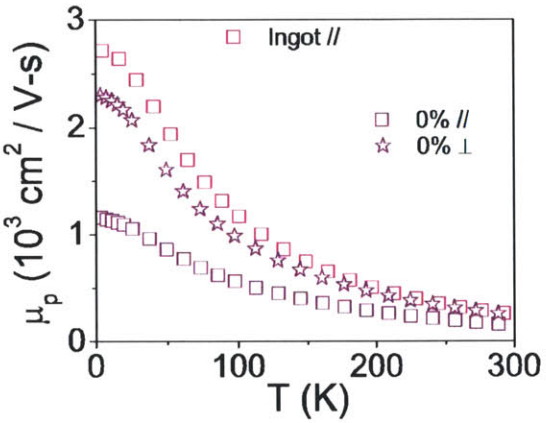

Figure B-3: Plot of the hole mobility μ_p of samples 0% and Ingot // as a function of temperature.

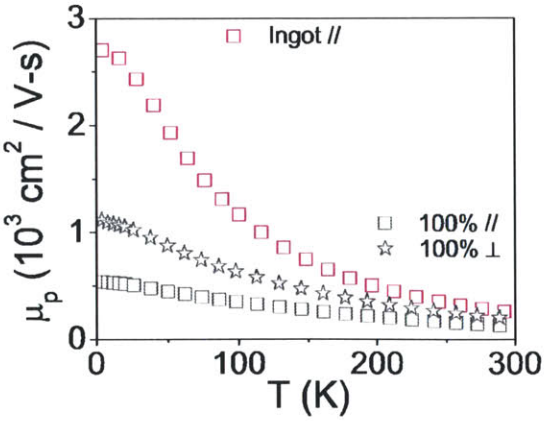

Figure B-4: Plot of the hole mobility μ_p of samples 100% and Ingot // as a function of temperature.

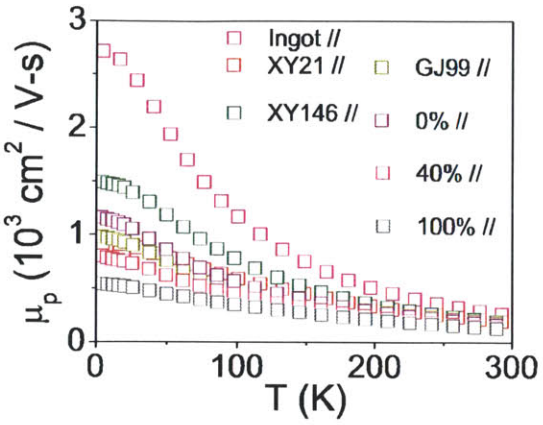

Figure B-5: Plot of the hole mobility μ_p of all nanocomposite samples measured in the // direction and sample Ingot // as a function of temperature.

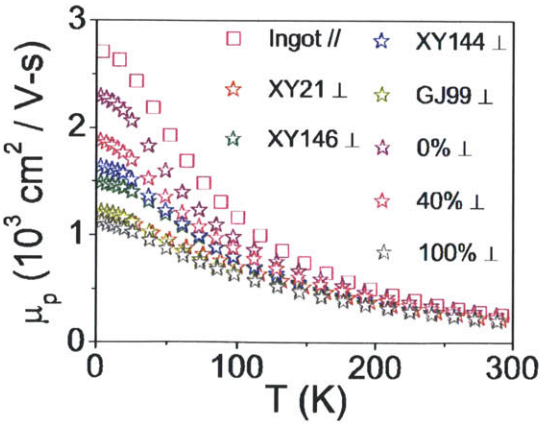

Figure B-6: Plot of the hole mobility μ_p of all nanocomposite samples measured in the $\perp$ direction and sample Ingot // as a function of temperature.

THIS PAGE INTENTIONALLY LEFT BLANK

Appendix C

Additional Hole Mean Free Path Results

Appendix C shows the results of the temperature-dependent hole mean free path results for samples for which my results are not displayed in Section 3.5.2. Please refer back to Section 3.4 for the complete sample's description and to Section 3.5.2 for the detailed discussion of these results.

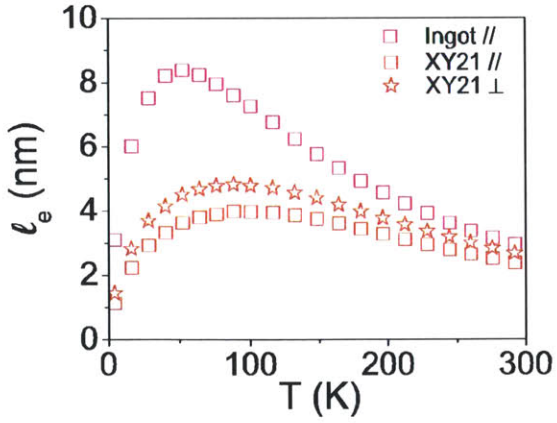

Figure C-1: Plot of the hole mean free path of samples XY21 and Ingot // as a function of temperature.

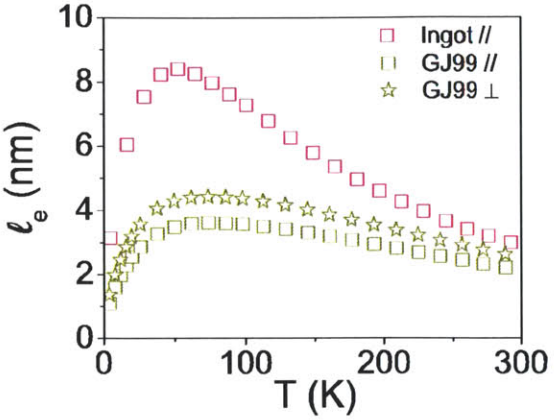

Figure C-2: Plot of the hole mean free path of samples GJ99 and Ingot // as a function of temperature.

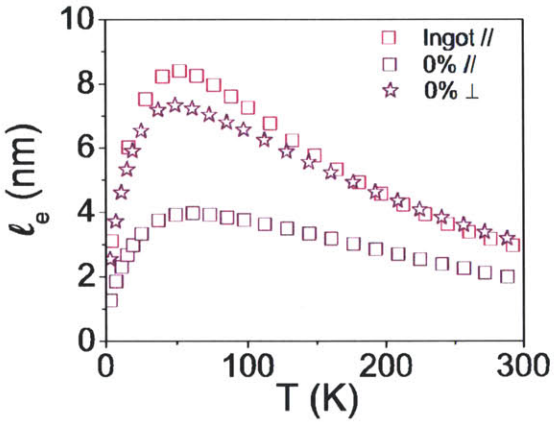

Figure C-3: Plot of the hole mean free path of samples 0% and Ingot // as a function of temperature.

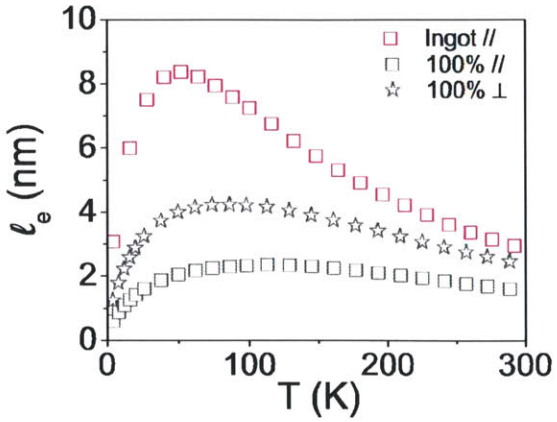

Figure C-4: Plot of the hole mean free path of samples 100% and Ingot // as a function of temperature.

Appendix D

Additional Phonon Mean Free Path Results

Appendix D shows the results of the temperature-dependent phonon mean free path results for samples for which my results are not displayed in Section 3.5.2. Please refer back to Section 3.4 for the complete sample's description and to Section 3.5.2 for the detailed discussion of these results.

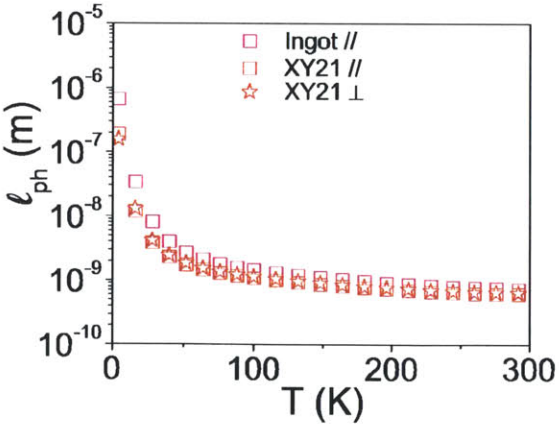

Figure D-1: Plot of phonon mean free path of samples XY21 and Ingot // as a function of temperature.

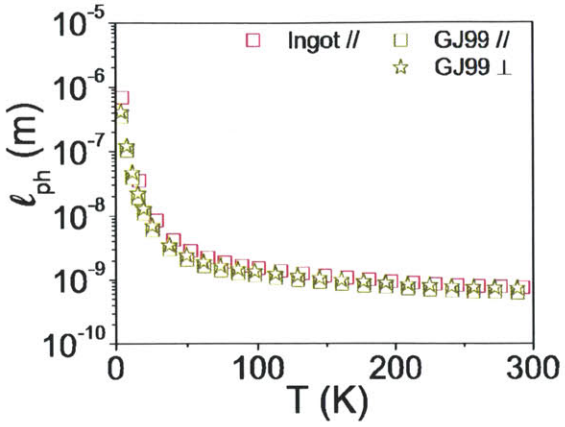

Figure D-2: Plot of phonon mean free path of samples GJ99 and Ingot // as a function of temperature.

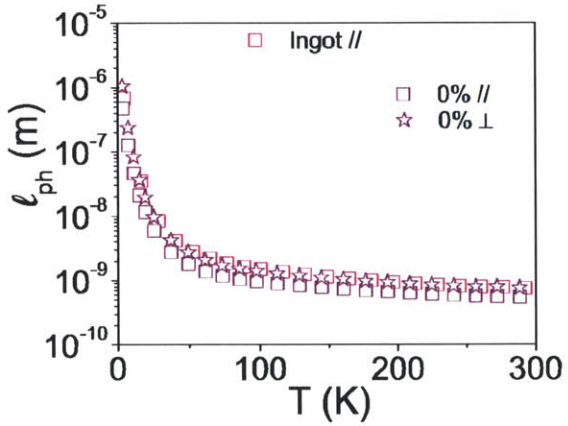

Figure D-3: Plot of phonon mean free path of samples 0% and Ingot // as a function of temperature.

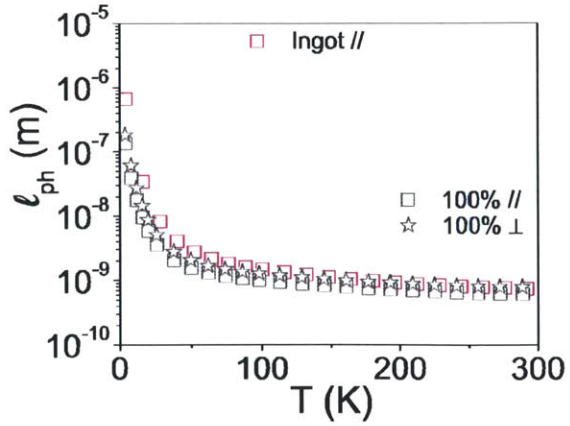

Figure D-4: Plot of phonon mean free path of samples 100% and Ingot // as a function of temperature.

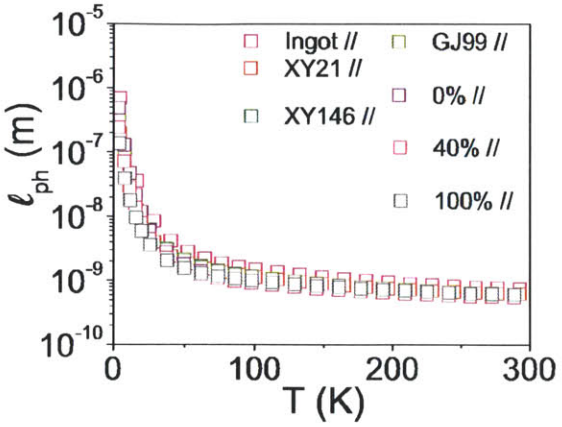

Figure D-5: Plot of phonon mean free path of all nanocomposite samples measured in the // direction and sample Ingot // as a function of temperature.

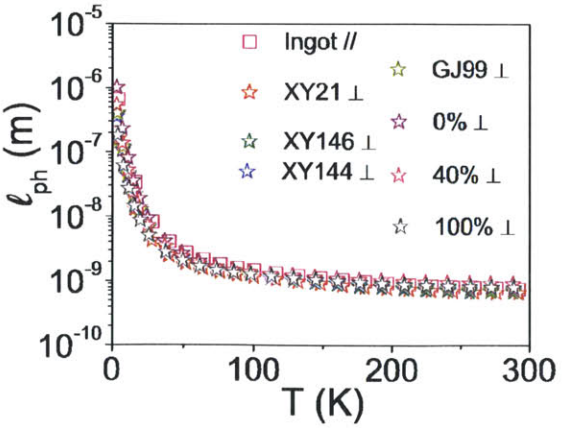

Figure D-6: Plot of phonon mean free path of all nanocomposite samples measured in the ⊥ direction and sample Ingot // as a function of temperature.

THIS PAGE INTENTIONALLY LEFT BLANK

Appendix E

Additional Transport Measurement Results Under an Applied Magnetic Field

Appendix E shows the results of κ_{th}, S, ρ measurements results for samples for which my results are not displayed in Section 5.1. Please refer back to Section 3.4 for the complete sample's description and to Section 5.1 for the detailed discussion of these results.

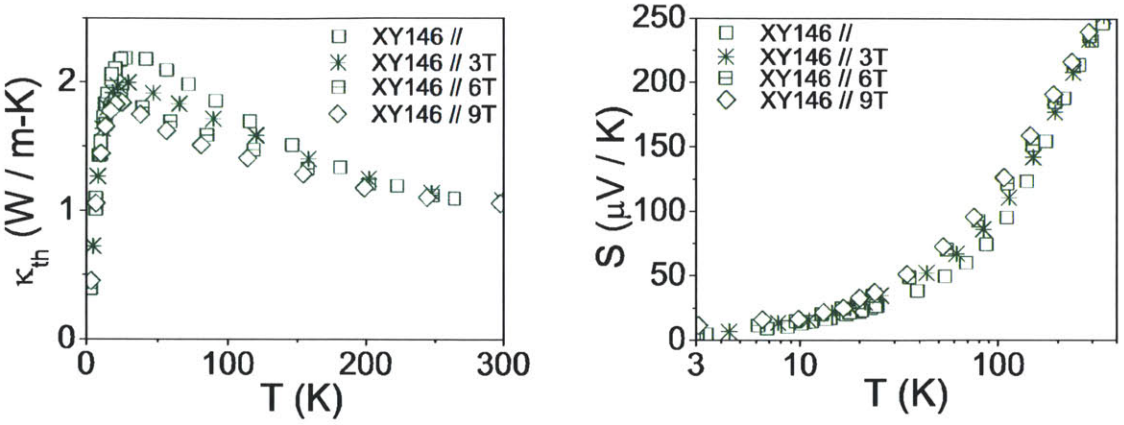

Figure E-1: Plots of κ_{th} and S of sample XY146 // as a function of temperature under applied magnetic field strengths of 0, 3, 6, and 9T. The plots clearly show that the applied B field decreases the sample's κ_{th} values, while increasing the sample's S. The effect is especially pronounced below 200K.

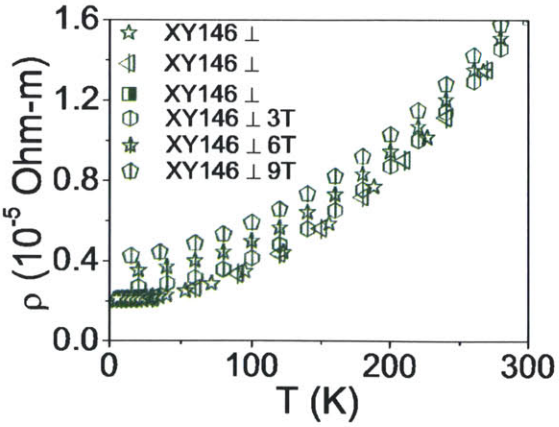

Figure E-2: Plot of ρ of sample XY146 $\perp$ as a function of temperature under applied magnetic field strengths of 0, 3, 6, and 9T. The plots clearly show that the applied B field increases its ρ values. The effect is especially pronounced below 200K.

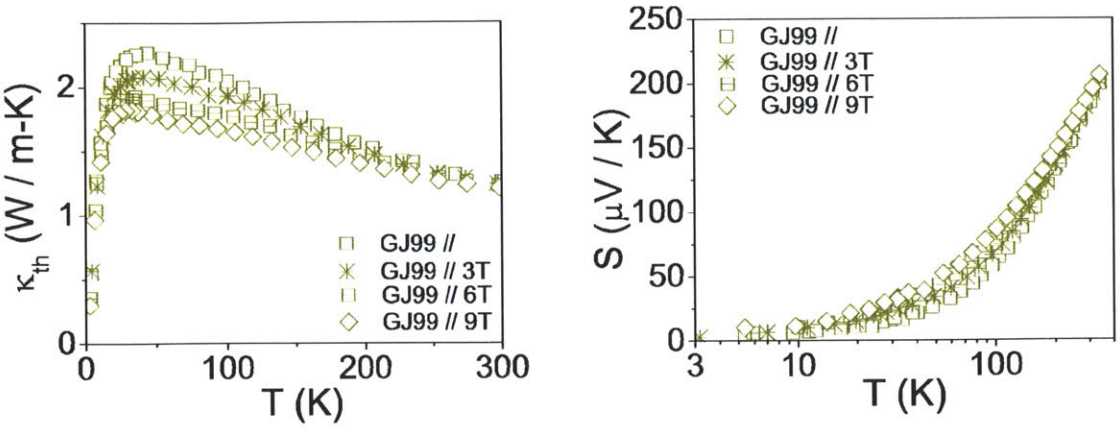

Figure E-3: Plots of κ_{th} and S of sample GJ99 // as a function of temperature under applied magnetic field strengths of 0, 3, 6, and 9T. The plots clearly show that the applied B field decreases the sample's κ_{th} values, while increasing the sample's S. The effect is especially pronounced below 200K.

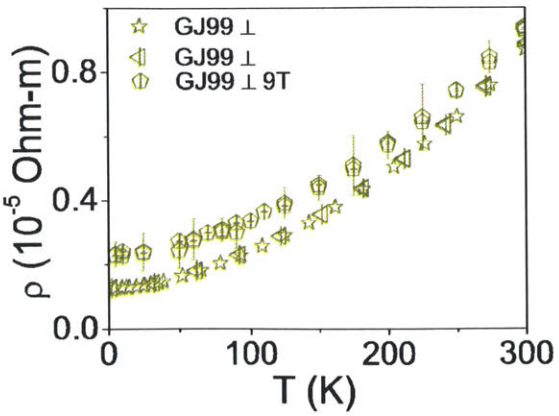

Figure E-4: Plot of ρ of sample GJ99 $\perp$ as a function of temperature under applied magnetic field strengths of 0 and 9T. The plots clearly show that the applied B field increases its ρ values. The effect is especially pronounced below 200K.

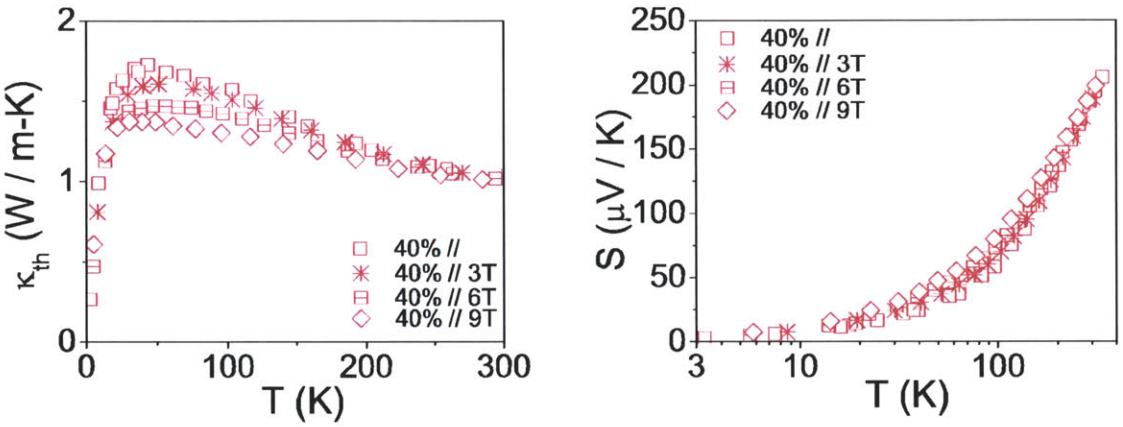

Figure E-5: Plots of κ_{th} and S of sample 40% // as a function of temperature under applied magnetic field strengths of 0, 3, 6, and 9T. The plots clearly show that the applied B field decreases the sample's κ_{th} values, while increasing the sample's S. The effect is especially pronounced below 200K.

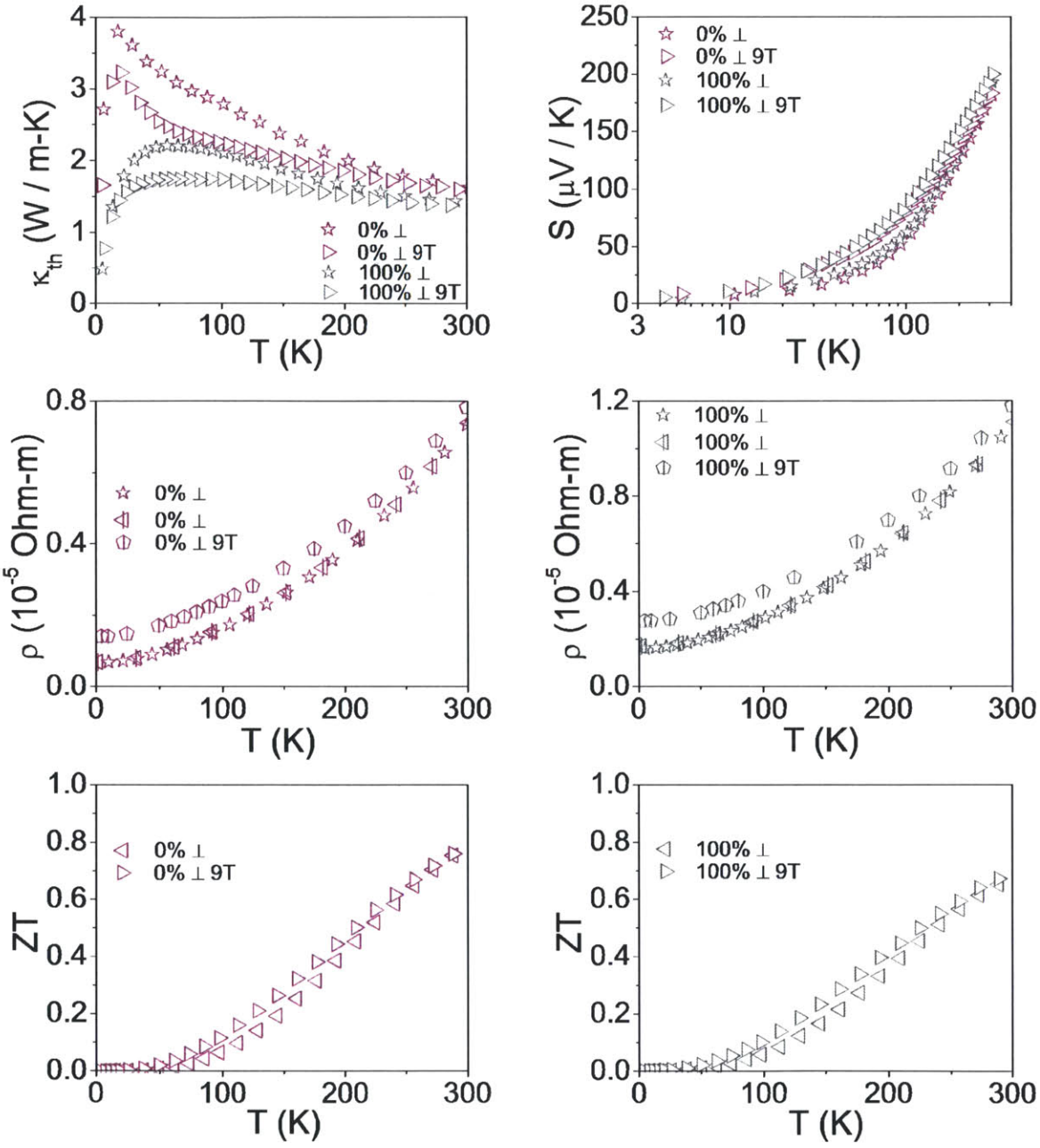

Figure E-6: Plots of κ_{th}, S, ρ, and ZT of samples 0% $\perp$ and 100% $\perp$ as a function of temperature under applied magnetic field strengths of 0 and 9T. The plots clearly show that the applied B field decreases the sample's κ_{th} values, while increasing the sample's S and ρ values. As a result, an increase in ZT at low temperature is observed. The effect is especially pronounced below 200K.

THIS PAGE INTENTIONALLY LEFT BLANK

Appendix F

Additional Electron Model Fitting Results

Appendix F shows my electron model fitting results for samples for which my results are not displayed in Section 4.5. Please refer back to Section 3.4 for the complete sample's description, Sections 4.1.1 and 4.2.1 for the description of my electron model, and Section 4.5 for the detailed discussion of these results.

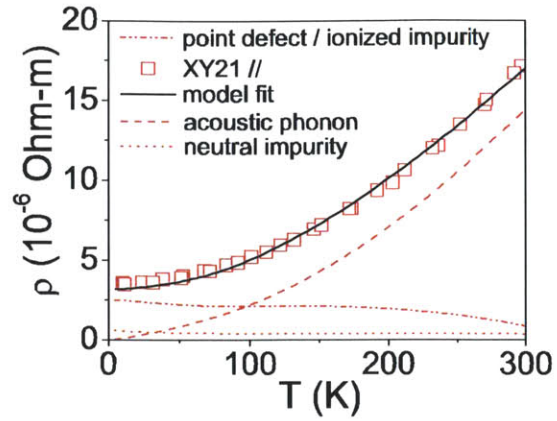

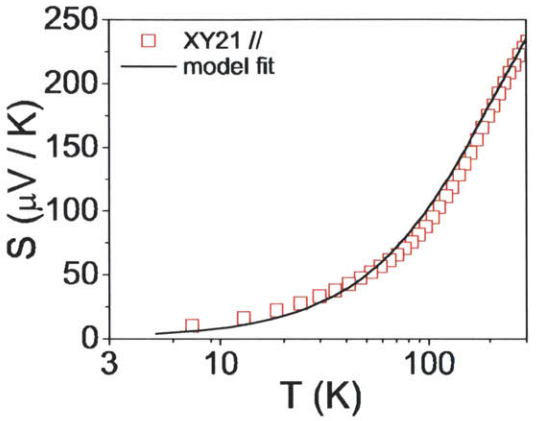

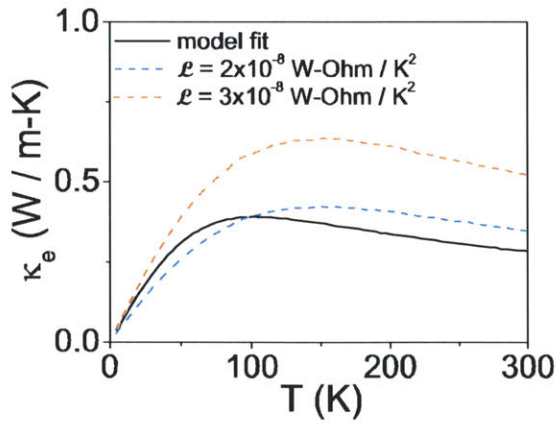

Figure F-1: Fitting results of sample XY21 // based on the electron model. The contribution to ρ from acoustic phonon scattering, point defect / ionized impurity atom scattering, and neutral impurity atom scattering are plotted as well. The fitting results confirm that the acoustic phonon scattering mechanism dominates for $T > 200$K and that the point defect scattering mechanism dominates for $T < 20$K. From κ_e, $\mathcal{L}$ is calculated to decrease as T increases.

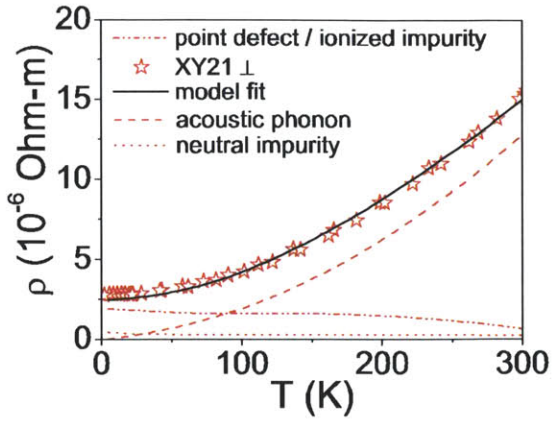

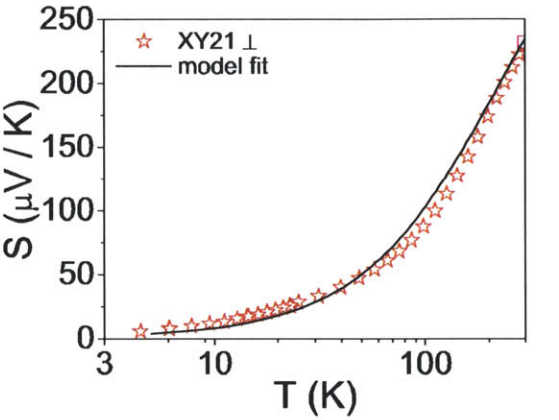

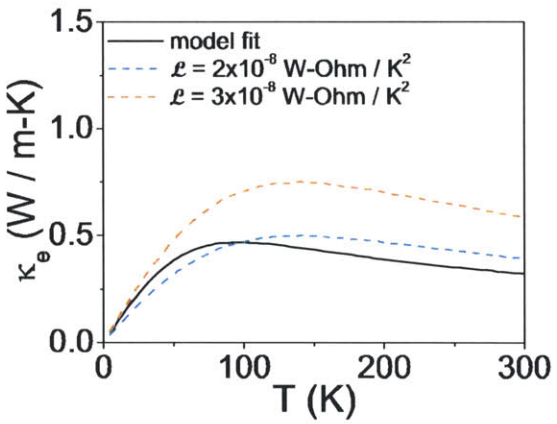

Figure F-2: Fitting results of sample XY21 $\perp$ based on the electron model. The contribution to ρ from acoustic phonon scattering, point defect / ionized impurity atom scattering, and neutral impurity atom scattering are plotted as well. The fitting results confirm that the acoustic phonon scattering mechanism dominates for $T > 200$K and that the point defect scattering mechanism dominates for $T < 20$K. From κ_e, $\mathcal{L}$ is calculated to decrease as T increases.

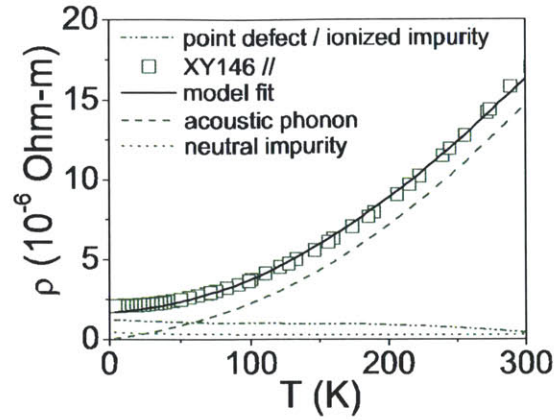

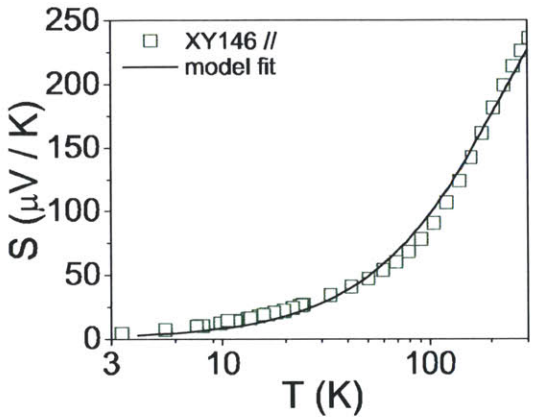

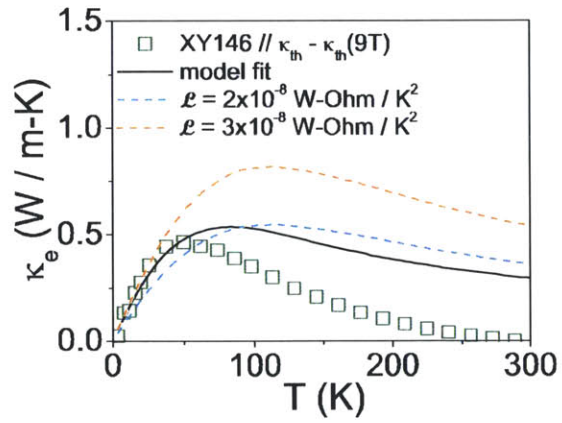

Figure F-3: Fitting results of sample XY146 // based on the electron model. The contribution to ρ from acoustic phonon scattering, point defect / ionized impurity atom scattering, and neutral impurity atom scattering are plotted as well. The fitting results confirm that the acoustic phonon scattering mechanism dominates for $T > 200$K and that the point defect scattering mechanism dominates for $T < 20$K. From κ_e, $\mathcal{L}$ is calculated to decrease as T increases.

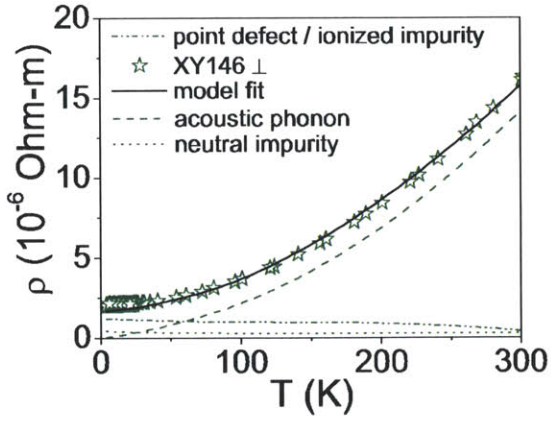

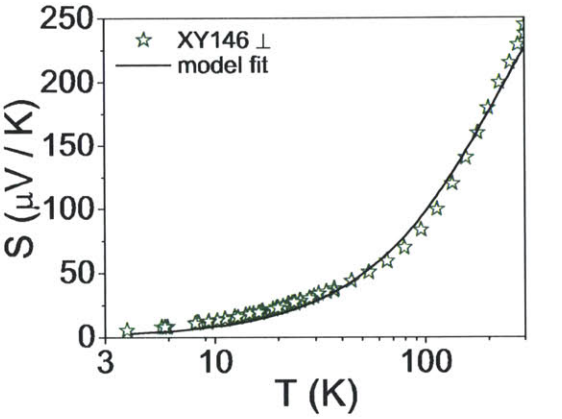

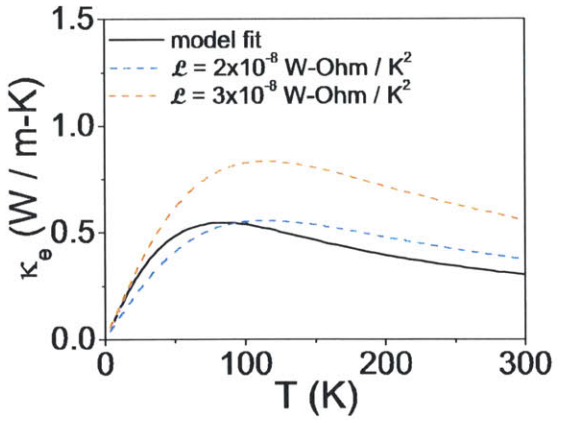

Figure F-4: Fitting results of sample XY146 $\perp$ based on the electron model. The contribution to ρ from acoustic phonon scattering, point defect / ionized impurity atom scattering, and neutral impurity atom scattering are plotted as well. The fitting results confirm that the acoustic phonon scattering mechanism dominates for $T > 200$K and that the point defect scattering mechanism dominates for $T < 20$K. From κ_e, $\mathcal{L}$ is calculated to decrease as T increases.

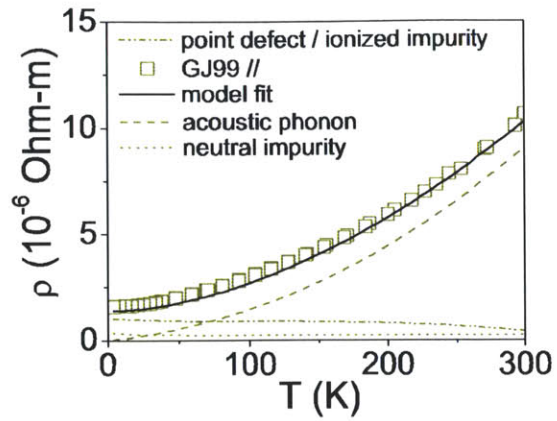

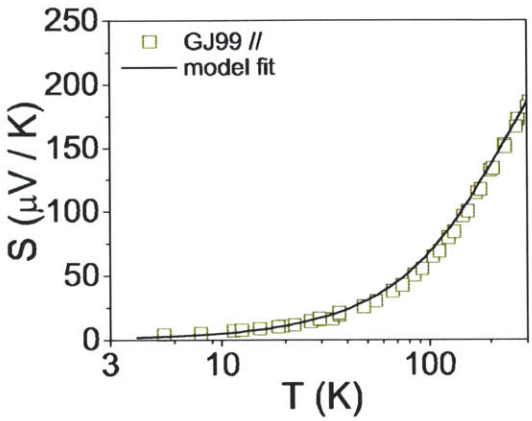

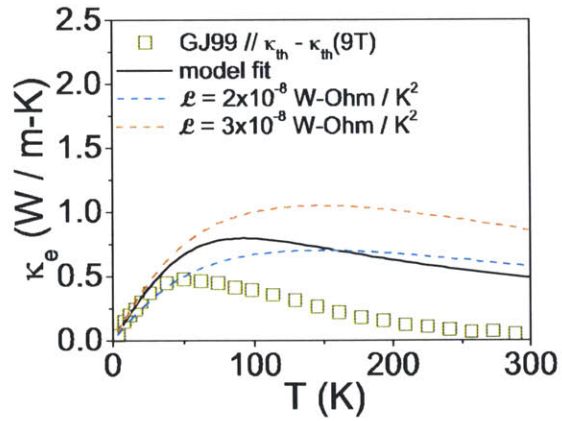

Figure F-5: Fitting results of sample GJ99 // based on the electron model. The contribution to ρ from acoustic phonon scattering, point defect / ionized impurity atom scattering, and neutral impurity atom scattering are plotted as well. The fitting results confirm that the acoustic phonon scattering mechanism dominates for $T > 200$K and that the point defect scattering mechanism dominates for $T < 20$K. From κ_e, $\mathcal{L}$ is calculated to decrease as T increases.

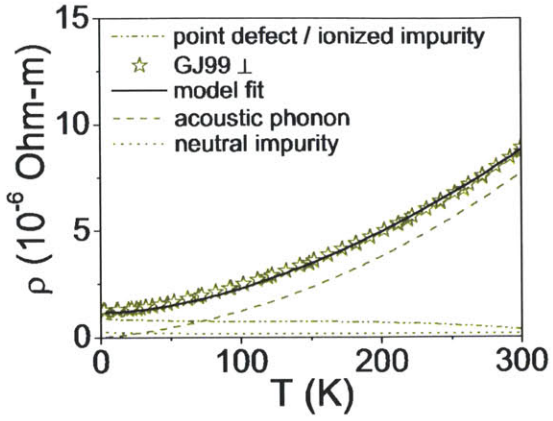

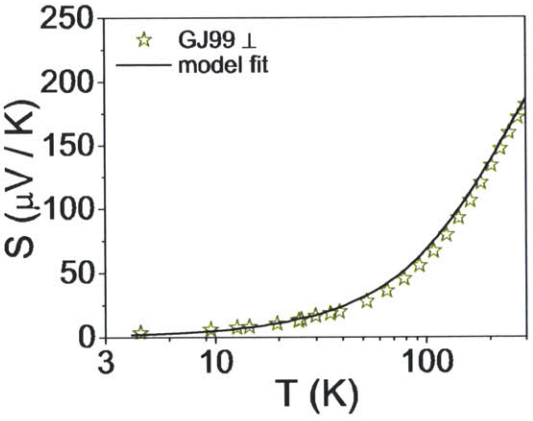

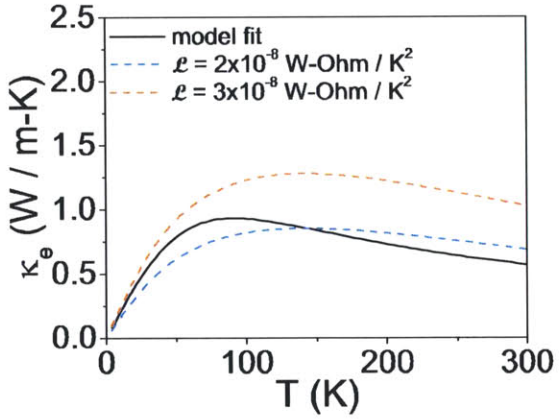

Figure F-6: Fitting results of sample GJ99 $\perp$ based on the electron model. The contribution to ρ from acoustic phonon scattering, point defect / ionized impurity atom scattering, and neutral impurity atom scattering are plotted as well. The fitting results confirm that the acoustic phonon scattering mechanism dominates for $T > 200$K and that the point defect scattering mechanism dominates for $T < 20$K. From κ_e, $\mathcal{L}$ is calculated to decrease as T increases.

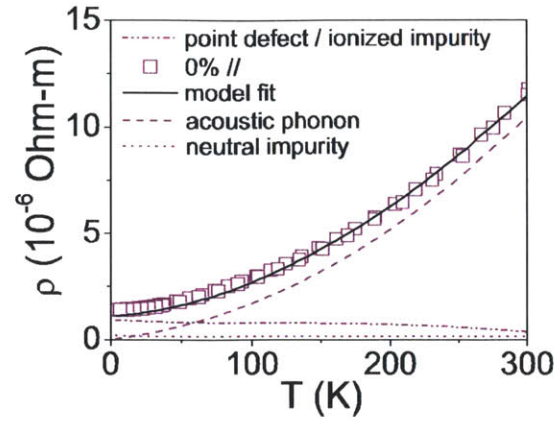

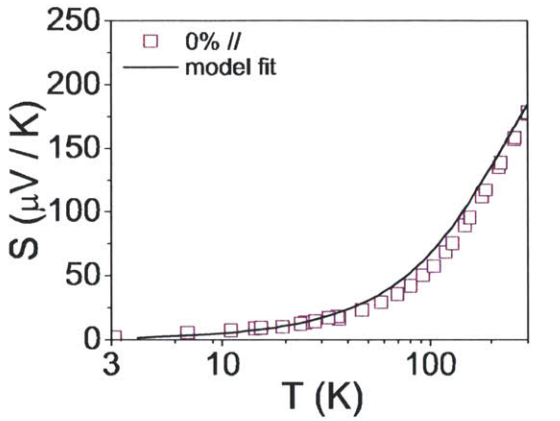

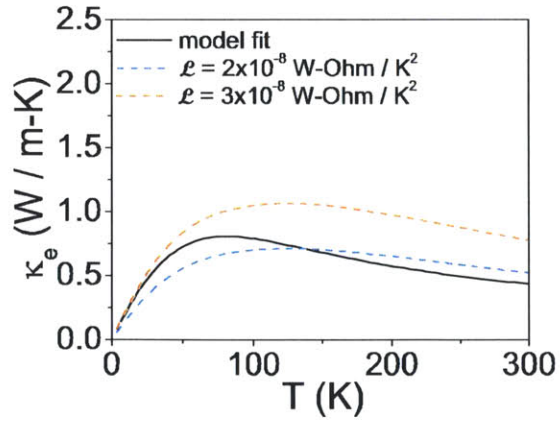

Figure F-7: Fitting results of sample 0% // based on the electron model. The contribution to ρ from acoustic phonon scattering, point defect / ionized impurity atom scattering, and neutral impurity atom scattering are plotted as well. The fitting results confirm that the acoustic phonon scattering mechanism dominates for $T > 200$K and that the point defect scattering mechanism dominates for $T < 20$K. From κ_e, $\mathcal{L}$ is calculated to decrease as T increases.

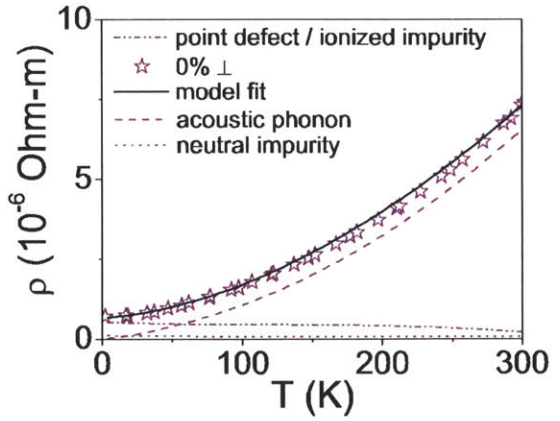

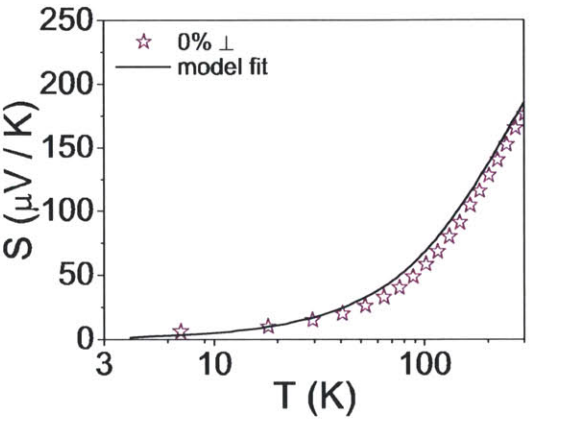

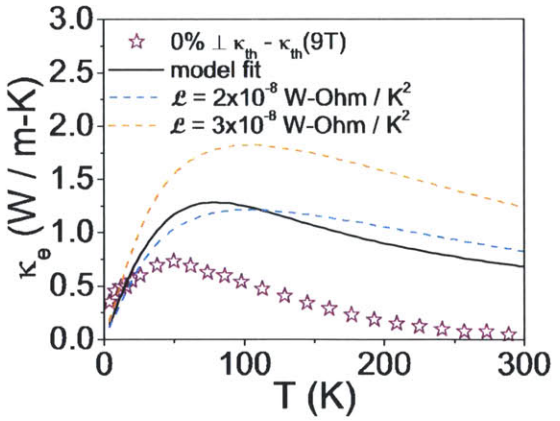

Figure F-8: Fitting results of sample 0% ⊥ based on the electron model. The contribution to ρ from acoustic phonon scattering, point defect / ionized impurity atom scattering, and neutral impurity atom scattering are plotted as well. The fitting results confirm that the acoustic phonon scattering mechanism dominates for $T > 200$K and that the point defect scattering mechanism dominates for $T < 20$K. From κ_e, $\mathcal{L}$ is calculated to decrease as T increases.

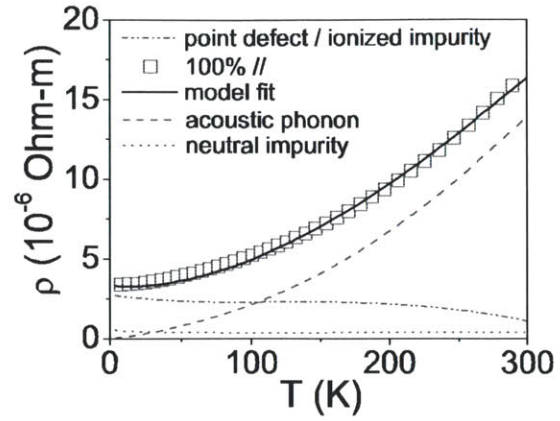

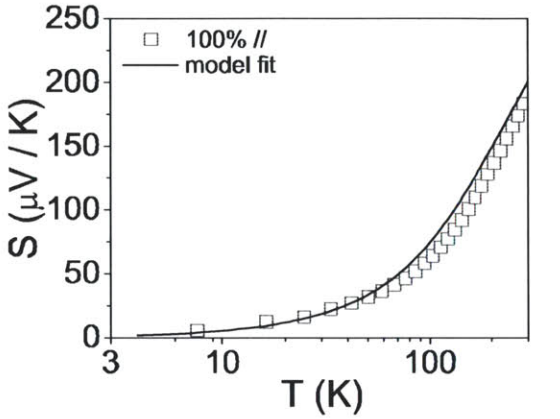

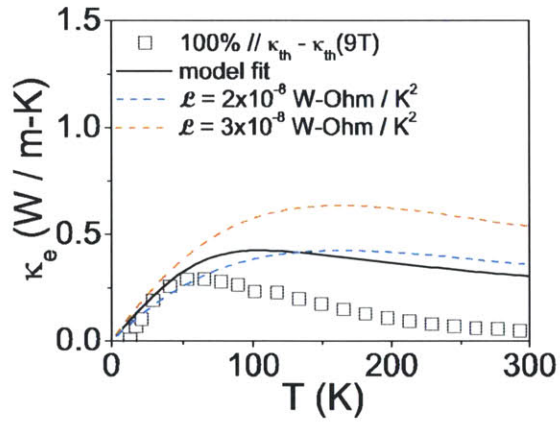

Figure F-9: Fitting results of sample 100% // based on the electron model. The contribution to ρ from acoustic phonon scattering, point defect / ionized impurity atom scattering, and neutral impurity atom scattering are plotted as well. The fitting results confirm that the acoustic phonon scattering mechanism dominates for $T > 200$K and that the point defect scattering mechanism dominates for $T < 20$K. From κ_e, $\mathcal{L}$ is calculated to decrease as T increases.

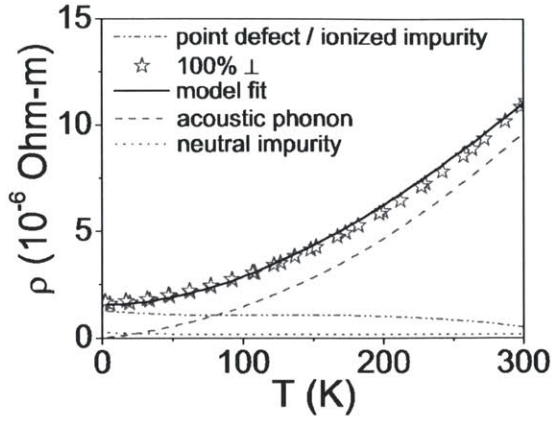

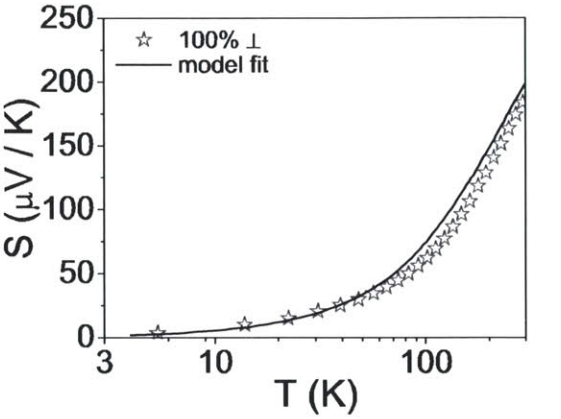

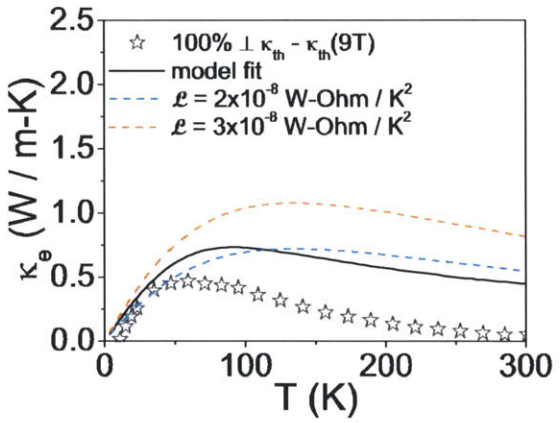

Figure F-10: Fitting results of sample 100% $\perp$ based on the electron model. The contribution to ρ from acoustic phonon scattering, point defect / ionized impurity atom scattering, and neutral impurity atom scattering are plotted as well. The fitting results confirm that the acoustic phonon scattering mechanism dominates for $T > 200$K and that the point defect scattering mechanism dominates for $T < 20$K. From κ_e, $\mathcal{L}$ is calculated to decrease as T increases.

Appendix G

Additional Phonon Model Fitting Results

Appendix G shows my phonon model fitting results for samples for which my results are not displayed in Section 4.5. Please refer back to Section 3.4 for the complete sample's description, Sections 4.1.2 and 4.2.2 for the description of my phonon model, and Section 4.5 for the detailed discussion of these results.

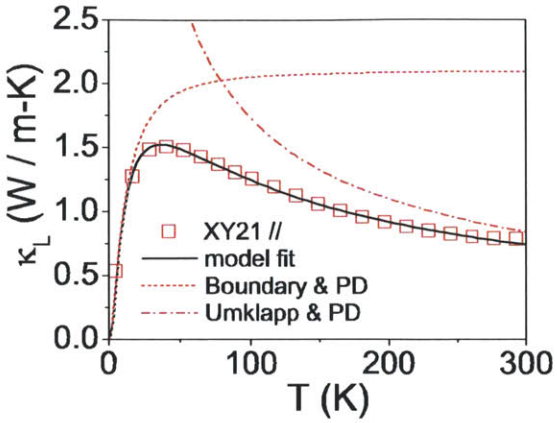

Figure G-1: Fitting results of sample XY21 // based on the phonon model. The boundary scattering together with the point defect scattering mechanisms (Boundary & PD), as well as the Umklapp scattering together with the point defect scattering mechanisms (Umklapp & PD), are plotted along with κ_L.

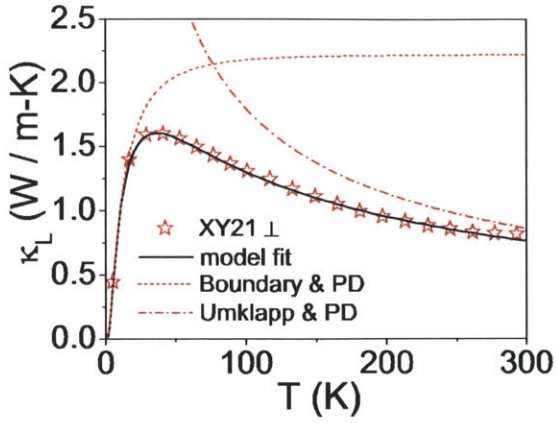

Figure G-2: Fitting results of sample XY21 $\perp$ based on the phonon model. The boundary scattering together with the point defect scattering mechanisms (Boundary & PD), as well as the Umklapp scattering together with the point defect scattering mechanisms (Umklapp & PD), are plotted along with κ_L.

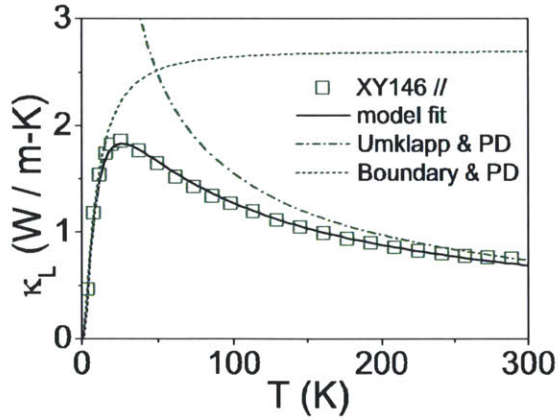

Figure G-3: Fitting results of sample XY146 // based on the phonon model. The boundary scattering together with the point defect scattering mechanisms (Boundary & PD), as well as the Umklapp scattering together with the point defect scattering mechanisms (Umklapp & PD), are plotted along with κ_L.

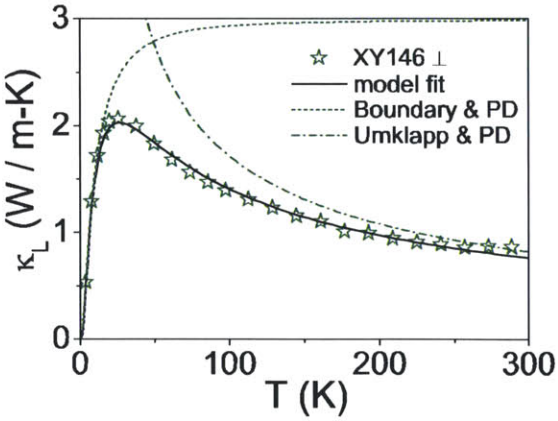

Figure G-4: Fitting results of sample XY146 $\perp$ based on the phonon model. The boundary scattering together with the point defect scattering mechanisms (Boundary & PD), as well as the Umklapp scattering together with the point defect scattering mechanisms (Umklapp & PD), are plotted along with κ_L.

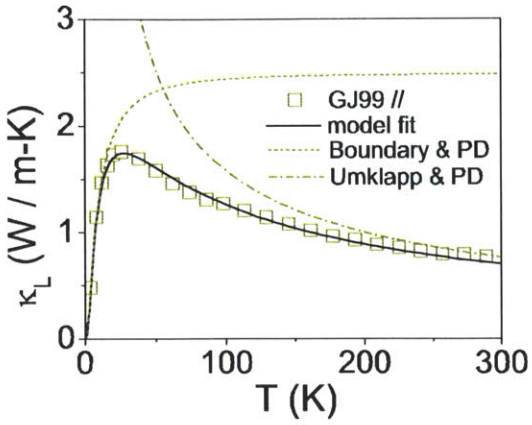

Figure G-5: Fitting results of sample GJ99 // based on the phonon model. The boundary scattering together with the point defect scattering mechanisms (Boundary & PD), as well as the Umklapp scattering together with the point defect scattering mechanisms (Umklapp & PD), are plotted along with κ_L.

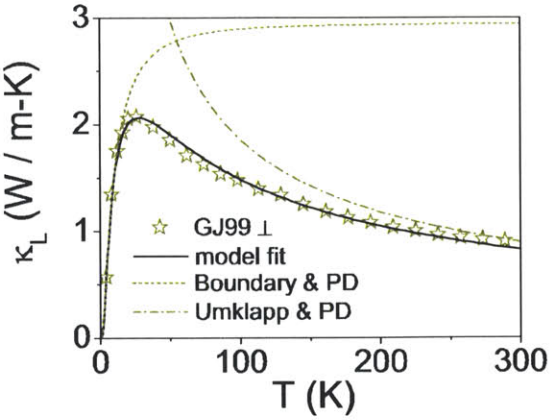

Figure G-6: Fitting results of sample GJ99 $\perp$ based on the phonon model. The boundary scattering together with the point defect scattering mechanisms (Boundary & PD), as well as the Umklapp scattering together with the point defect scattering mechanisms (Umklapp & PD), are plotted along with κ_L.

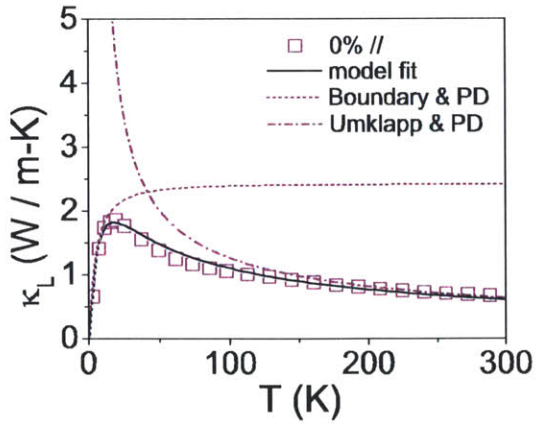

Figure G-7: Fitting results of sample 0% // based on the phonon model. The boundary scattering together with the point defect scattering mechanisms (Boundary & PD), as well as the Umklapp scattering together with the point defect scattering mechanisms (Umklapp & PD), are plotted along with κ_L.

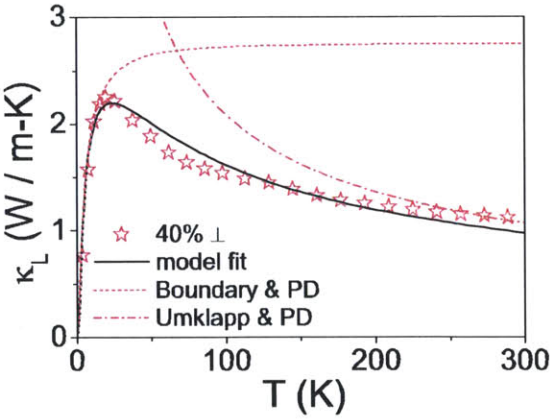

Figure G-8: Fitting results of sample 0% $\perp$ based on the phonon model. The boundary scattering together with the point defect scattering mechanisms (Boundary & PD), as well as the Umklapp scattering together with the point defect scattering mechanisms (Umklapp & PD), are plotted along with κ_L.

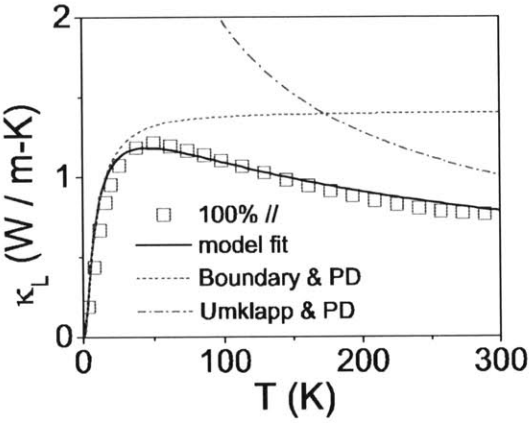

Figure G-9: Fitting results of sample 100% // based on the phonon model. The boundary scattering together with the point defect scattering mechanisms (Boundary & PD), as well as the Umklapp scattering together with the point defect scattering mechanisms (Umklapp & PD), are plotted along with κ_L.

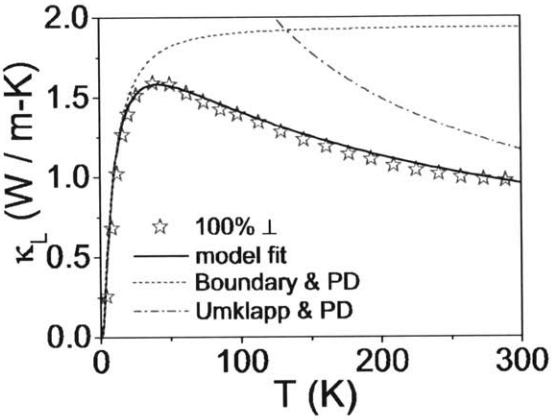

Figure G-10: Fitting results of sample 100% ⊥ based on the phonon model. The boundary scattering together with the point defect scattering mechanisms (Boundary & PD), as well as the Umklapp scattering together with the point defect scattering mechanisms (Umklapp & PD), are plotted along with κ_L.

Appendix H

Additional κ_{th}, κ_{th}(9T), calculated κ_L, and calculated κ_e Results

Appendix H shows the calculated κ_L, calculated κ_e, κ_{th}, and κ_{th}(9T) for samples for which my results are not displayed in Section 4.5. Please refer back to Section 3.4 for the complete sample's description and to Section 4.5 for the detailed discussion of these results.

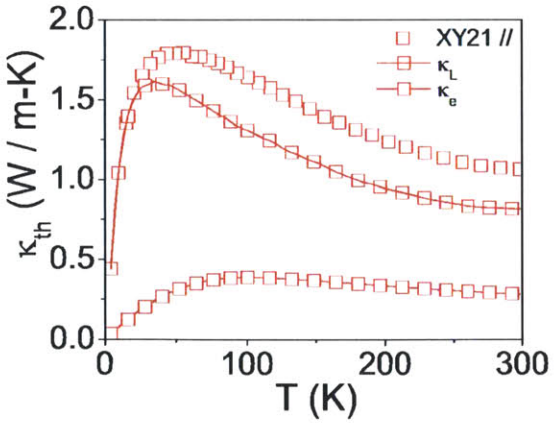

Figure H-1: Plot of the calculated κ_L, calculated κ_e, κ_{th}, and κ_{th}(9T) of sample XY21 // as a function of temperature.

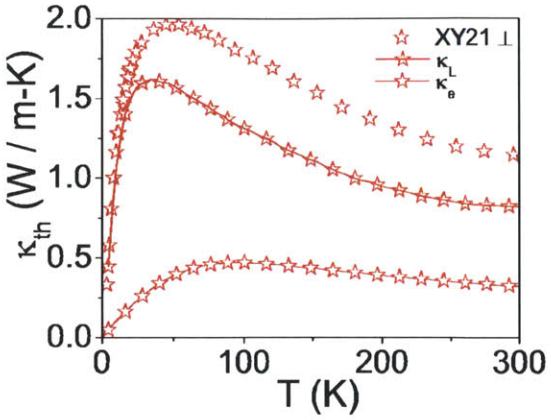

Figure H-2: Plot of the calculated κ_L, calculated κ_e, κ_{th}, and κ_{th}(9T) of sample XY21 $\perp$ as a function of temperature.

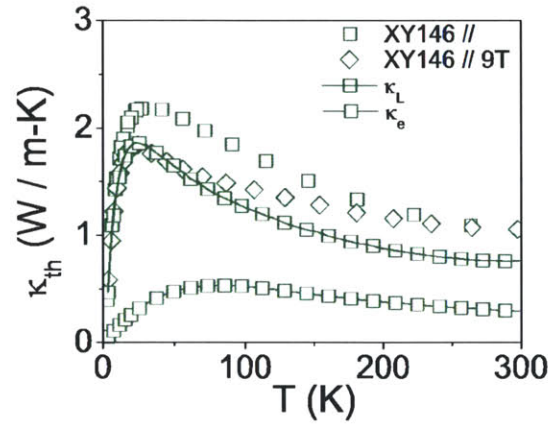

Figure H-3: Plot of the calculated κ_L, calculated κ_e, κ_{th}, and κ_{th}(9T) of sample XY146 // as a function of temperature.

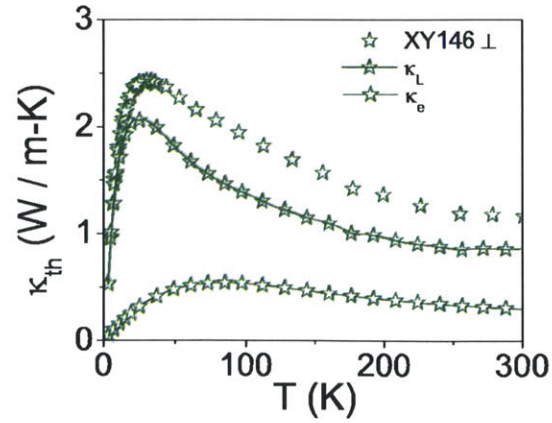

Figure H-4: Plot of the calculated κ_L, calculated κ_e, κ_{th}, and κ_{th}(9T) of sample XY146 $\perp$ as a function of temperature.

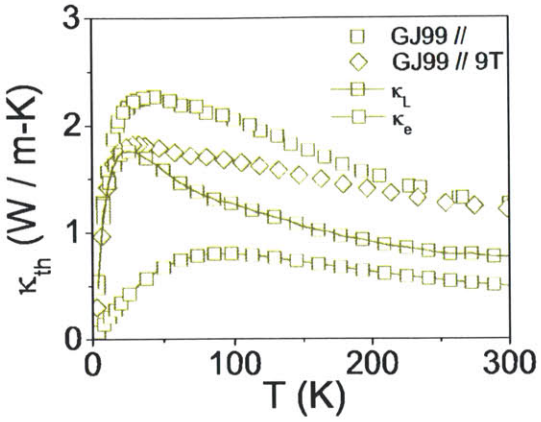

Figure H-5: Plot of the calculated κ_L, calculated κ_e, κ_{th}, and κ_{th}(9T) of sample GJ99 // as a function of temperature.

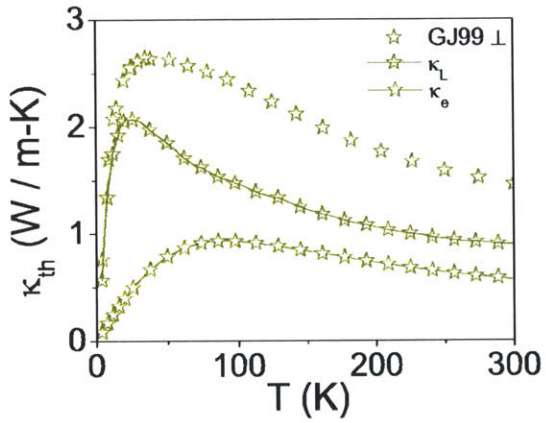

Figure H-6: Plot of the calculated κ_L, calculated κ_e, κ_{th}, and κ_{th}(9T) of sample GJ99 $\perp$ as a function of temperature.

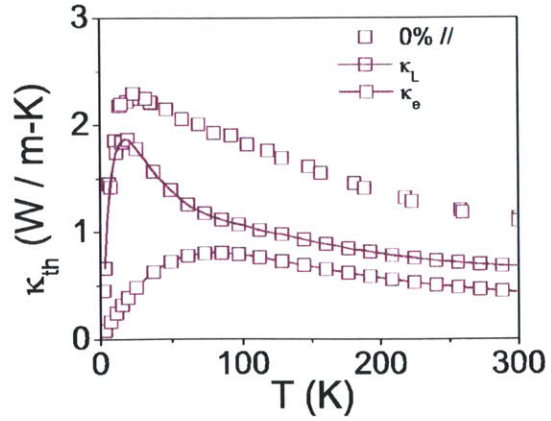

Figure H-7: Plot of the calculated κ_L, calculated κ_e, κ_{th}, and κ_{th}(9T) of sample 0% // as a function of temperature.

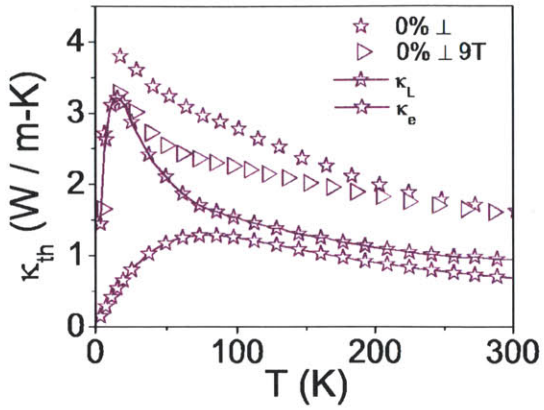

Figure H-8: Plot of the calculated κ_L, calculated κ_e, κ_{th}, and κ_{th}(9T) of sample 0% $\perp$ as a function of temperature.

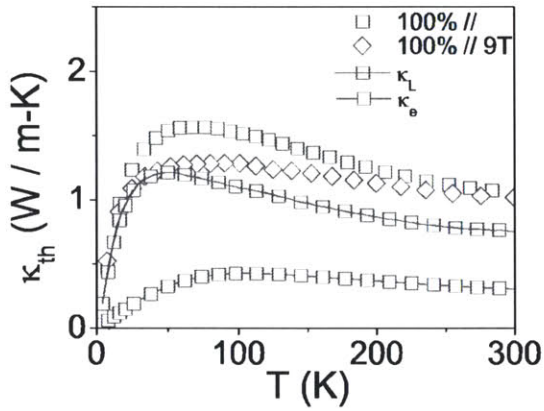

Figure H-9: Plot of the calculated κ_L, calculated κ_e, κ_{th}, and κ_{th}(9T) of sample 100% // as a function of temperature.

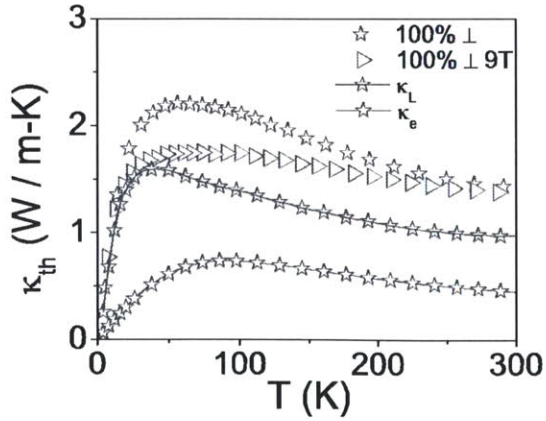

Figure H-10: Plot of the calculated κ_L, calculated κ_e, κ_{th}, and κ_{th}(9T) of sample 100% $\perp$ as a function of temperature.

Bibliography

[1] S. Fan et al., Applied Physics Letter **96**, 182104 (2010).

[2] B. Poudel et al., Science **320**, 634 (2008).

[3] H. J. Goldsmid, Journal of Applied Physics **32**, 2198 (1961).

[4] W. M. Yim and F. D. Rosi, Solid-State Ekcrronics **15**, 1121 (1972).

[5] J. E. A. Alderson, T. Farrell, and C. M. Hurd, Physical Review **174**, 729 (1968).

[6] B. L. Huang and M. Kaviany, Physical Review B **77**, 125209 (2008).

[7] E. V. Oleshko and V. N. Korolyshin, Soviet Physics, Solid state **27**, 1723 (1985).

[8] L. P. Caywood and G. R. Miller, Physical Review B **2**, 3209 (1970).

[9] H. J. Goldsmid, *Thermoelectric Refrigeration*, Plenum Press, New York, NY, 1964.

[10] L. D. Hicks and M. S. Dresselhaus, Phys. Rev. B **47**, 12727 (1993).

[11] L. D. Hicks and M. S. Dresselhaus, Phys. Rev. B **47**, 16631 (1993).

[12] R. Venkatasubramanian, E. Siivola, T. Colpitts, and B. O'Quinn, Nature **413**, 597 (2001).

[13] http://www.ulvac.com/thermal/zem%203.asp, accessed on 7/29/2011.

[14] http://www.qdusa.com/products/ppms.html, accessed on 8/18/2011.

[15] Quantum Design, San Diego, CA, *Physical Property Measurement System: Thermal Transport Option User's Manual*, Third edition, 2002, Part Number 1684-100B, and references therein.

[16] N. R. Dilley, R. C. Black, L. Montes, A. Wilson, and M. Simmonds, Commercial Apparatus for Measuring Thermal Transport Properties from 1.9 to 390 Kelvin, in *Thermoelectric Materials 2001– Research and Applications: MRS Symposium Proceedings, Boston, November 2001*, volume 691, pages 85–90, Warrendale, PA, 2002, Materials Research Society Press.

[17] O. Maldonado, Cryogenics **32**, 908 (1992).

[18] N. D. Lowhorn et al., Applied Physics A **94**, 231 (2009).

[19] W. M. Yim, E. V. Fitzke, and F. D. Rosi, Journal of Materials Science **1**, 52 (1966).

[20] H. W. Jeon, H. P. Ha, D. B. Hyun, and J. D. Shim, Journal of Physics and Chemistry of Solids **52**, 579 (1991).

[21] H. T. Langhammer, M. Stordeur, H. Sobotta, and V. Riede, Physica Status Solidi B **109**, 673 (1982).

[22] S. K. Mishrayz, S. Satpathyyz, and O. Jepsen, Journal of Physics: Condensed Matter **9**, 461 (1997).

[23] H. J. Goldsmid, Proceedings of The Physical Society of London **72**, 17 (1958).

[24] H. J. Goldsmid, Proceedings of The Physical Society of London **71**, 633 (1958).

[25] B. Yates, Journal of Electronics and Control **6**, 26 (1959).

[26] H. Scherrer and S. Scherrer, Thermoelectric Properties of Bismuth Antimony Telluride, in *Thermoelectrics Handbook: Macro to Nano*, edited by D. Rowe, chapter 327, pages 27–6, CRC Press, BGoca Raton, FL, 2006.

[27] R. Sehr and L. R. Testardi, Journal of Physics and Chemistry of Solids **23**, 1219 (1962).

[28] J. Black, E. M. Conwell, L. Seigle, and C. W. Spencer, Journal of Physics and Chemistry of Solids **2**, 240 (1957).

[29] R. Togei and G. R. Miller, Energy Bands in Bi_2Te_3: Pseudopotential Approach, in *The Physics of Semimetals and Narrow-Gap Semiconductors*, edited by D. L. Carter and R. T. Bate, pages 349–360, New York, NY, 1970, Pergamon Press.

[30] H. Kohler, Physica Status Solidi B **73**, 95 (1976).

[31] H. Kohler, Physica Status Solidi B **75**, 127 (1976).

[32] M. Stordeur, M. Stolzer, H. Sobotta, and V. Riede, Physica Status Solidi B **150**, 165 (1988).

[33] G. Wang and T. Cagin, Applied Physics Letters **89**, 152101 (2006).

[34] G. Wang and T. Cagin, Physical Review B **76** (2007).

[35] H. Scherrer and S. Scherrer, Bismuth Telluride, Antimony Telluride, and Their Solid Solutions, in *CRC Handbook of Thermoelectrics*, edited by D. M. Rowe, chapter 19, CRC Press, New York, NY, 1995.

[36] N. E. Ashcroft and N. D. Mermin, *Solid State Physics*, chapter 1, Saunders College Publishing, New York, 1976.

[37] C. Kittel, *Introduction to Solid State Physics*, chapter 5, John Wiley & Sons, Inc., New York, NY, Seventh edition, 1996.

[38] T. M. Tritt, *Thermal Conductivity: Theory, Properties, and Applications*, Kluwer Academic / Plenum Publishers, New York, NY, 2004.

[39] M. S. Dresselhaus et al., Advanced Materials **19**, 1043 (2007).

[40] N. E. Ashcroft and N. D. Mermin, *Solid State Physics*, chapter 16, Saunders College Publishing, New York, NY, 1976.

[41] N. E. Ashcroft and N. D. Mermin, *Solid State Physics*, chapter 13, Saunders College Publishing, New York, 1976.

[42] X. Sun, Z. Zhang, and M. S. Dresselhaus, Appl. Phys. Lett. **74**, 4005 (1999).

[43] N. E. Ashcroft and N. D. Mermin, *Solid State Physics*, chapter 25, Saunders College Publishing, New York, 1976.

[44] M. Lundstrom, *Fundamentals of Carrier Transport*, chapter 2, Cambridge University Press, New York, NY, Second edition, 2000.

[45] B. M. Askerov, *Electron Transport Phenomena in Semiconductors*, chapter 3, World Scientific, Singapore, 1994.

[46] C. Erginsoy, Physical Review **79**, 1013 (1950).

[47] J. W. Harrison and J. R. Hauser, Physical Review B **13**, 5347 (1976).

[48] D. K. Ferry, Physical Review B **17**, 912 (1978).

[49] C. R. Tellier, Thin Solid Films **51**, 311 (1978).

[50] J. W. Harrison and J. R. Hauser, Journal of Applied Physics **47**, 292 (1976).

[51] Collaboration: Authors and editors of the volumes III/17E-17F-41C, Group III Condensed Matter, Numerical Data and Functional Relationships in Science and Technology, in *Landolt-Bornstein*, edited by O. Madelung, U. Rossler, and M. Schulz, volume 41C: Non-Tetrahedrally Bonded Elements and Binary Compounds I, Springer-Verlag, New York, NY, 1996, and references therein.

[52] W. Richter, H. Kohler, and C. R. Becker, Physica Status Solidi B **84**, 619 (1977).

[53] D. P. White and P. G. Klemens, Journal of Applied Physics **71**, 4258 (1992).

[54] P. G. Klemens, Proceedings of The Physical Society of London Section A **68**, 1113 (1955).

[55] B. Abeles, Physical Review **131**, 1906 (1963).

[56] G. A. Slack, Physical Review **105**, 829 (1957).

[57] G. A. Slack, Physical Review **122**, 1451 (1961).

[58] G. A. Slack, Physical Review **122**, 1962 (1961).

[59] G. A. Slack, Physical Review **126**, 427 (1962).

[60] C. Dames, M. S. Dresselhaus, and G. Chen, Phonon Thermal Conductivity of Superlattice Nanowires for Thermoelectric Applications, in *Thermoelectric Materials 2003 - Research and Applications*, edited by Nolas, GS and Yang, J and Hogan, TP and Johnson, DC, volume 793 of *Materials Research Society Symposium Proceedings*, pages 15–20, Mat Res Soc, 2004, Symposium on Thermoelectric Materials held at the 2003 MRS Fall Meeting, Boston, MA, DEC 01-03, 2003.

[61] G. S. Nolas, G. Fowler, and J. Yang, Journal of Applied Physics **100**, 043705 (2006).

[62] Y. J. Han, Physical Review B **54**, 8977 (1996).

[63] J. O. Jenkins, J. A. Rayne, and R. W. Ure, Jr., Physical Review B **5**, 3171 (1972).

[64] P. Lost'ak et al., Journal of Physics and Chemistry of Solids **67**, 1457 (2006).

[65] J. S. Blakemore, Solid-State Ekcrronics **25**, 1067 (1982).

[66] T. Orlando, S. Senturia, and P. Hagelstein, Physics for Solid State Applications, Chapter 3 of MIT 6.730 Course Notes.

[67] P. R. Bevington and D. K. Robinson, *Data Reduction and Error Analysis for the Physical Sciences*, chapter 8, McGraw-Hill, New York, NY, Third edition, 2003.

[68] J. J. More, The Levenberg-Marquardt Algorithm: Implementation and Theory, in *Numerical Analysis: Proceedings of the Biennial Conference Held at Dundee, June 28-July 1, 1977*, edited by G. Watson, pages 105–116, New York, NY, 1978, Springer-Verlag.

[69] A. B. Pippard, *Magnetoresistance in Metals*, Cambridge University Press, New York, NY, 1989.